Fall 11-14-2022

Induced Seismicity in the Raton Basin and Global Variability of the 410-km Discontinuity

Margaret E. Glasgow
University of new mexico

Recommended Citation

Glasgow, Margaret E.. "Induced Seismicity in the Raton Basin and Global Variability of the 410-km Discontinuity." (2022). https://digitalrepository.unm.edu/eps_etds/329

Margaret E. Glasgow
Candidate

Earth and Planetary Sciences
Department

This dissertation is approved, and it is acceptable in quality and form for publication:

Approved by the Dissertation Committee:

Dr. Brandon Schmandt, Chairperson

Dr. Susan Bilek

Dr. Mousumi Roy

Dr. Susan Bilek

Induced Seismicity in the Raton Basin and Global Variability of the 410-km Discontinuity

by

Margaret E. Glasgow

B.S., Geology, University of North Carolina Wilmington, 2014

M.S., Earth and Planetary Sciences, University of New Mexico, 2017

DISSERTATION

Submitted in Partial Fulfillment of the Requirements for the Degree of

Doctor of Philosophy Earth and Planetary Sciences

The University of New Mexico Albuquerque, New Mexico

December 2022

Acknowledgements

I greatly appreciate the support, guidance, and creativity of my advisor, Brandon Schmandt. Thank you to my colleagues for creating an engaging work environment, especially Han, Justin, Collin, and Evans. Thank you to my parents for supporting my undergraduate education which helped set me on this path.

Induced Seismicity in the Raton Basin and Global Variability of the 410-km Discontinuity

by

Margaret E. Glasgow

B.S., Geology, University of North Carolina Wilmington, 2014

M.S., Earth and Planetary Sciences, University of New Mexico, 2017

Ph.D., Earth and Planetary Sciences, University of New Mexico, 2022

Abstract

Natural processes like mantle convection and plate tectonics dominate Earth's seismic structure. Recently human activities have increasingly influenced the deformation of the shallow crust. In this dissertation, passive source seismology was used to constrain seismic discontinuities in the mantle transition zone and seismogenic structures in induced earthquake settings. Using a novel sampling method and uniform processing approach, I found the 410-km discontinuity is thermally and compositionally variable. Using a machine-learning approach, I found the three main zones of seismicity in the Raton Basin consist of short faults or fault segments with variable orientations. The zone that hosted a Mw 5.3 earthquake in 2011 became seismically quiescent by 2016, whereas the two other zones remain active. Furthermore, the Mw 5.3 earthquake appears to have been a composite rupture which is rarely observed for moderate magnitude earthquakes. This dissertation places constraints on mantle seismic structure and seismogenic structures in the crust.

Table of Contents

1. Chapter One: Introduction

The Earth is dynamic on variable spatial and temporal scales. Large plates slowly move and collide along its surface and sink into the mantle. Earthquakes quickly release energy along the edges of and within plates. Our first-order approximation of how Earth works often breaks down at different spatial or temporal scales. For example, Earth's average structure is well approximated using 1-D models, but 3-D variations introduce vertical and lateral anomalies. Earthquake modeling using planar fault rupture is sufficient in many cases, but we know rupture can be more complex and faults can be curved. This thesis uses observations to reveal new findings regarding the seismic discontinuities in the mantle transition zone and seismogenic structures in induced earthquake settings.

In the past decade there has been a significant increase in the number of human-induced earthquakes for the central United States. Since its peak in 2015, seismicity has decreased but it remains elevated compared to its pre-2010 rate. Most of the central United States was poorly instrumented with seismometers during the onset of induced seismicity. Increased instrumentation with both long-term and temporary arrays has greatly improved the understanding of induced seismicity. Chapters 2 and 3 utilized periods with increased instrumentation in the Raton Basin, an induced seismicity region on the Colorado-New Mexico border where wastewater disposal by injection began in 1994. The basin has experienced injection-induced seismicity since 2001. Previous results suggested the basin includes three zones of seismicity. Each zone was suggested to have a through-going normal fault that is ~10-15 km long. In Chapter 2, I utilized two new datasets, a seven-station broadband network and a one-month geophone array, to build an earthquake catalog from 2016-2020 using a machine-learning approach. From 2016-2020, I found two of the three zones are seismically active. Each zone is composed of short, < 3km long, reactivated basement faults with variable strikes and faulting styles. Additionally, I found the spatiotemporal-magnitude statistics for the Raton Basin seismicity was similar to those for tectonic settings which suggests the majority of earthquakes release stored tectonic stress.

The zone that hosted very little seismicity during the 2016-2020 study (chapter 2), known as the Trinidad zone, was investigated in Chapter 3. I utilized a rapid aftershock network deployed following the largest recorded earthquake in the basin, a Mw 5.3 in 2011, to build an earthquake catalog for the 2011 earthquake sequence using the same machine learning approach from Chapter 3. Earthquakes clustered into six main groups that have a NE-SW composite trend. A single-station template matching method was used to extend the temporal resolution of Trinidad zone seismicity from 2008-2022. This fourteen-year catalog provides the most in-depth investigation of the spatiotemporal evolution of Trinidad zone seismicity, including the 2011 earthquake sequence. The catalog reveals a multi-segment rupture for the Mw 5.3 earthquake rather than previous suggestions of a single planar fault rupture. Multi-segment rupture has been observed for large magnitude (M>6) earthquakes, but it is rarely observed for moderate magnitude earthquakes. The ability of an earthquake to grow by connecting multiple segments presents a challenge for hazard assessment, especially in fluid-injection settings where faults are often unmapped or buried until reactivated.

Seismic observations of the mantle transition zone are often collected using one of two approaches: regional sampling with dense arrays of seismometers or global sampling with broadly distributed single stations. The fourth chapter of this thesis bridges the two traditional sampling approaches by using dense regional arrays from around the globe. Data mining of an open-source database for densely spaced arrays of seismometers from 1990-2022 were used to calculate teleseismic P-to-S receiver functions for the 410-, 520-, and 660-km seismic discontinuities. This unprecedented dataset contains greater than 240,000 observations. The uniform processing and inversion of the receiver function datasets permitted their first global comparison. The mineral composition of the mantle is often estimated as pyrolytic, meaning ~55-60 vol. % olivine and ~40-45 vol. % garnet-pyroxene. However, I found the composition of the seismic discontinuity at ~410 km depth can vary greatly, from ~20-80 vol. % olivine with a mean composition of ~45-50 vol. % olivine. This suggests the 410-km discontinuity is compositionally variable despite being in a portion of the mantle that is considered well mixed.

Chapter 2 is published. Chapters 3 and 4 will be submitted for publication shortly after the thesis defense.

2. Chapter Two: Raton Basin induced seismicity is hosted by networks of short basement faults and mimics tectonic earthquake statistics

Abstract

The Raton Basin has been an area of injection induced seismicity for the past two decades. Previously, the reactivated fault zone structures and spatiotemporal response of seismicity to evolving injection have been poorly constrained due to sparse publicly available seismic monitoring. The application of a machine-learning phase picker to four years of continuous seismic data from a local array enables the detection and location of ~38,000 earthquakes. The events from 2016 to 2020 are ~2.5-6 km below sea level and range from M_L<-1 to 4.2. Most earthquakes occur within previously identified ~N-S zones of seismicity, however our new catalog illuminates that these zones are composed of many short faults with variable orientations. The two most active zones, the Vermejo Park and Tercio zones, are potentially linked by small intermediate faults. In total, we find ~60 short (<3 km long) basement faults with strikes from WNW to NNE. Faulting mechanisms are predominantly normal but some variability, including reverse dip-slip and oblique-slip, is observed. The Trinidad fault zone, which previously hosted a M_w 5.3 earthquake in 2011, is quiescent during 2016-2020, likely in response to both slow accumulation of tectonic strain after the 2011 sequence, and the significant decrease (80% reduction) in nearby wastewater injection from 2012 to 2016. Unlike some other regions, where induced seismicity was triggered in response to higher injection rates, the Raton Basin's frequency-magnitude and spatiotemporal statistics are not distinguishable from tectonic seismicity. The similarity suggests that seismicity in the Raton Basin is predominantly releasing tectonic stress.

2.1. Introduction

Human-induced earthquakes present societally relevant hazards and opportunities to study earthquake sequences and seismogenic structures in the central United States at accelerated time scales. The abrupt rise of human-induced earthquakes in the central U.S. began in 2009 and peaked in 2015 (Figure 2.1a; Keranen & Weingarten, 2018; Weingarten et al., 2015; Langenbruch et al., 2018). Wastewater injection from oil and gas operations is the main driver behind the observed seismicity (e.g., Ellsworth, 2013; Keranen et al., 2014; Weingarten et al., 2015). Since 2015, seismicity decreased on average for the central U.S. and decreased or plateaued for the strongest contributing regions, e.g., central Oklahoma and Arkansas (Langenbruch et al., 2018; Scanlon et al., 2019). However, a few regions have expanded oil and gas operations in recent years and are experiencing a rise in seismicity, e.g., west Texas and southeastern New Mexico (Skoumal & Trugman, 2021; Skoumal et al., 2020; Frohlich et al., 2020). Studying how seismicity evolves following the peak of wastewater injection may be informative for other regions that experience similar situations in the future. The Raton Basin located on the Colorado-New Mexico border is one of the regions in the central United States where seismicity ramped up in concert with wastewater injection (Figure 2.1b; Rubinstein et al., 2014). Coal-bed methane production and wastewater injection began in 1994 and its increase from ~2000-2002 was accompanied by a rapid increase in seismicity (Figure 2.1b; Advanced National Seismic System Comprehensive Earthquake Catalog (ANSS ComCat)). Thus, the Raton Basin's rise of induced seismicity was ~8 years ahead of the central U.S. average (Figure 2.1), and it is a valuable example of how induced seismicity can persist as injection decreases or potentially cease on local scales (e.g., Healy et al., 1968; Hsieh & Bredehoeft, 1981; Bollinger, et al., 1983). Historically, seismicity in the basin was rare but not absent. Rubinstein et al. (2014) estimated a magnitude of completeness of 3.8 for the Raton Basin from 1970 to 2011. One M≥4 earthquake occurred from 1970 to 2000 and 15 M≥4 earthquakes occurred from 2001-2020 (Rubinstein et al., 2014; ANSS ComCat, 2021). The rate of M≥3 earthquakes in the basin began increasing in 2001 and peaked at 20 M≥3 earthquakes in 2011. The largest earthquake of the region was the 2011 M_w 5.3 event (Barnhart et al., 2014; Rubinstein et al., 2014). Since 2011, seismicity has decreased to an average of ~6 M≥3 earthquakes/year but remains much higher than prior to 2001 (Figure 2.1). Most recently, the region has experienced some of the lowest rates of seismicity since 2001, with an average of 1.7 M≥3 earthquakes/year from Jan 2020- Sept 2021 (ANSS ComCat, 2021).

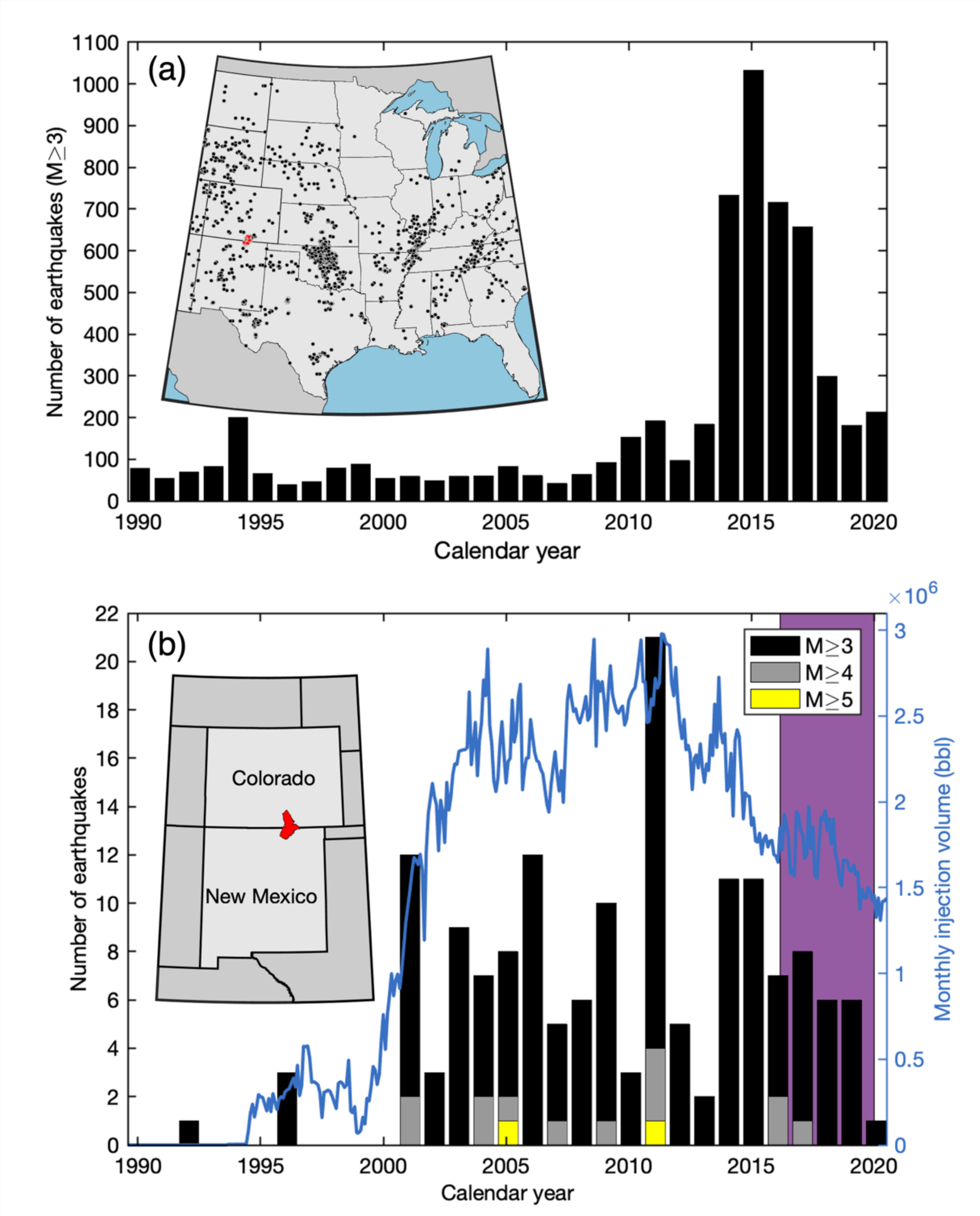

Figure 2.1 Central U.S. and Raton Basin seismicity. (a) Yearly number of M≥3 earthquakes in the central United States (ANSS ComCat, 2021). Inset displays map of the central United States with M≥3 earthquakes (circles). Red circles indicate earthquakes in the Raton Basin. (b) Yearly number of M≥3 earthquakes in the Raton Basin. See legend for magnitude details. Monthly injection volume (blue line) is on the right y-axis (COGCC, 2021; NMOCD, 2021). Injection is summed across the 24-29 wells typically operating in the

basin. Our study period from July 2016 to July 2020 is highlighted in purple. Inset displays state borders and the Raton Basin in red.

The disposal of fluids, generally byproducts of oil and gas production, by injection is the main driver of increased seismicity in the central United States (e.g., Ellsworth 2013; Keranen et al., 2014; Weingarten et al., 2015). Pore pressure changes are often considered the dominant mechanism for inducing earthquakes but poroelastic coupling can also play an important role (Segall & Lu, 2015). Wastewater injection near faults can increase the pore pressure and reduce the effective normal stress on a fault thereby promoting fault slip (Raleigh et al., 1976; Hsieh & Bredehoeft, 1981). Poroelasticity can amplify the stress changes potentially leading to an increase in both the seismic rate (Zhai et al., 2019) and seismic footprint (Goebel & Brodsky, 2018). In cases where hydraulic communication between faults and seismicity is weak or uncertain, poroelastic stress may be more effective than pore pressure diffusion at earthquake triggering, e.g., earthquakes on low permeability faults (Chang & Segall, 2016) or for far-field earthquakes (Goebel et al., 2017). Studies of induced seismicity in the central United States demonstrate that small pressure changes, e.g., <0.1 MPa, can induce earthquakes (Keranen et al., 2014; Nakai et al., 2017b; Verdecchia et al., 2021). In Oklahoma, and southern Kansas, the majority of induced earthquakes occur in the basement beneath the injection reservoir (Walsh & Zoback, 2015; Schoenball et al., 2017b). Precambrian basement faults extend upward into the primary wastewater disposal unit providing likely hydraulic pathways for downward migration of pore fluid pressure (Schwab et al., 2017). Earthquakes also occur in the basement in the Raton Basin (Nakai et al., 2017b). It is less certain how pore pressure is transmitted from the injection reservoir to the basement, but permeable faults have been hypothesized (Rubinstein et al., 2014; Nakai et al., 2017b).

Injection rate and cumulative injected volume are proposed as key parameters that influence induced seismicity in the United States (Weingarten et al., 2015; Scanlon et al., 2019; McGarr, 2014). High-rate injection wells (≥300,000 barrels/month) are associated with earthquakes twice as often as low-rate injection wells (<100,000 barrels/month) in the central and eastern United States (Weingarten et al., 2015). Scanlon et al. (2019) found the association of earthquakes to cumulative wastewater injection volume remained random below 1 million barrels (Mbbl) per well and increased from 60% at 1 Mbbl/well to ~90-100% at ≥30 Mbbl/well. Wastewater injection wells in the Raton Basin inject at a range of rates from high to low (≥300,000 to <100,000 bbl/month). The average injection rate in the basin since 2001 is low (~80,000-90,000 bbl/month per well) but the long injection history yields high cumulative injection volumes, ~22 Mbbl/well since 1994. Most recently, the basin has experienced a decline in the wastewater injection rate and volume (Figure 2.1b). The average rate for the ~10-year plateau of injection from 2004–2014 was ~2.45 Mbbl/month, whereas the rate from 2016-2021 is ~1.67 Mbbl/month.

Publicly available seismic data near the Raton Basin have been sparse, apart from the temporary aftershock deployments in 2001 and 2011 (Meremonte et al. 2002; Rubinstein et al. 2014) and the EarthScope Transportable Array during which two stations bounded the basin from 2008-2010 (Nakai et al., 2017a; 2017b). Previous seismic studies identified three prominent zones of seismicity (Figure 2.2), referred to as the Trinidad (Rubinstein et al., 2014; Barnhart et al., 2014), Vermejo Park, and Tercio zones (Nakai et al., 2017b). The Trinidad zone strikes NE-SW, extends ~15 km, and hosted the largest recorded earthquake within the basin, a M_w 5.3 in 2011 (Rubinstein et al., 2014). The Vermejo Park and Tercio zones strike N-S and extend ~20 and ~10 km, respectively (Nakai et al., 2017b). It is unclear if these zones are spanned by continuous faults. Recent research utilizing a dense one-month array deployed in a subset of the Raton Basin suggests that more complex fault networks exist within the previously identified zones of seismicity (Wang et al., 2020a).

Deployment and continuous operation of a local broadband array since 2016 (Figure 2.2) creates the opportunity to advance knowledge of the structural setting and the spatiotemporal characteristics of Raton Basin seismicity in the context of post-peak wastewater injection. A new high-resolution earthquake catalog was built by taking advantage of a machine-learning phase picker (Zhu & Beroza, 2019) and a waveform correlation-based hypocenter estimation method (Trugman & Shearer, 2017) to investigate four years of continuous seismic data. The new catalog of ~38,000 events is quantitatively analyzed to constrain the geometry of reactivated faults, whose diverse orientations are supported by complementary focal mechanism analysis. Spatiotemporal-magnitude statistics are calculated for multiple sections of the basin and compared to results from tectonic and other induced settings to evaluate potential drivers of Raton Basin seismicity.

2.2. Geologic background

The Raton Basin is asymmetric with the synclinal axis west of center (Johnson & Finn, 2001). The western margin dips steeply east toward the Sangre de Cristo Mountains, whereas the eastern margin tilts gently west (Woodward, 1997; Johnson & Finn, 2001; Flores & Bader, 1999; Baltz, 1965). The Devonian through Plio-Pleistocene basin stratigraphy is underlain by Precambrian basement (Johnson & Finn, 2001). The basin is defined by the area contained within the Trinidad sandstone and Vermejo formation contact (Figure 2.2; Hemborg, 1998). East-west compression during the Laramide orogeny (late Cretaceous to early Tertiary) resulted in predominantly ~N-S oriented faults and fold axes (Woodward, 1997). Igneous activity during the mid to late Tertiary emplaced dikes, sills, and laccoliths along the weak zones created during the Laramide orogeny (Johnson, 1969; Johnson & Wood 1956; Woodward, 1997). The widespread intrusive activity includes over 80 mapped dikes and sills (Johnson, 1969; Dane & Bachman, 1965, Woodward, 1997) and the Spanish Peaks (Figure 2.2) towering over the basin with ~1.5 km of topographic relief (Johnson & Finn, 2001). Igneous intrusions and faults can impact fluid flow by acting as either permeable paths or impermeable barriers. Hemborg (1998) suggests faulting and intrusions in the northern Raton Basin may have enhanced the permeability of coal reservoirs and notes that higher performing wells are closer to faults.

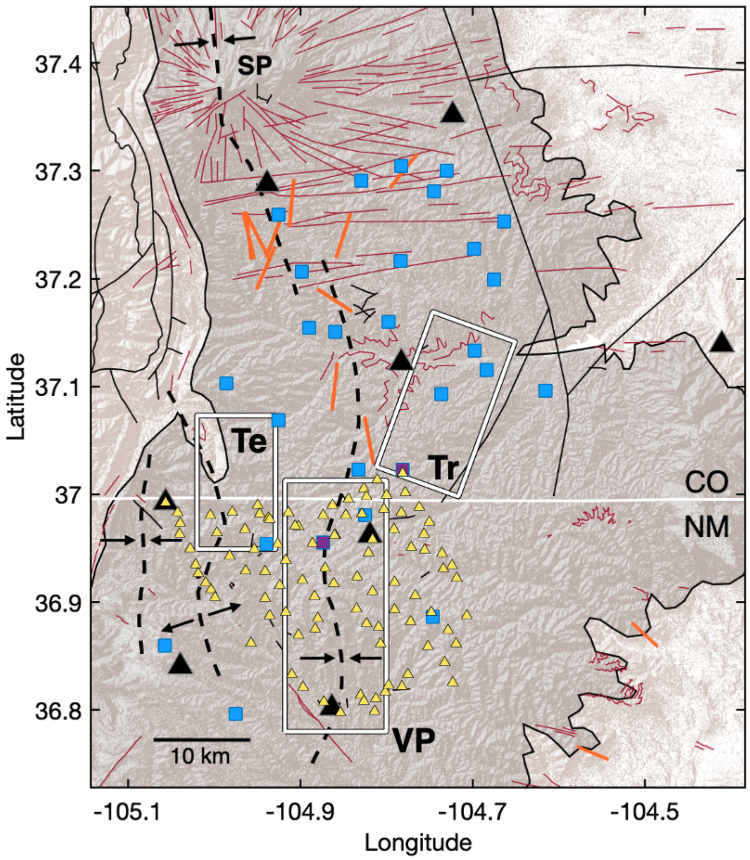

Figure 2.2 Map of study region. The Raton Basin is outlined in black and shaded gray. The map displays the eight broadband seismometers (black triangles), 96 geophone nodes (yellow triangles), and 29 wastewater injection wells (blue squares) used in this study. Purple squares indicate co-located wastewater injection wells. The three white boxes approximate previously identified zones of seismicity from Rubinstein et al., (2014) and Nakai et al., (2017). They are abbreviated Te – Tercio, Tr – Trinidad, and VP – Vermejo Park. Geologic features include mapped surface faults (black lines), mapped dikes and sills (red lines), and anticlines and synclines (dashed black lines; Stoeser et al., 2007; Johnson, 1969; Pillmore 1964, 1965a, 1965b, 1969, 2003; Papadopulous & Associates, Inc., 2008). The Spanish Peaks are labeled SP. Orange lines are maximum horizontal stress orientations from Lund Snee and Zoback, (2020).

The Raton Basin is located at the intersection of two major stress fields, the N-S normal faulting extensional stress field of the Rio Grande Rift and the E-W strike-slip compressive stress field of the broader central United States (Lund Snee & Zoback, 2020). This convergence produces a range of stress orientations, from NE-SW to NW-SE maximum horizontal stress, in and along the margins of the basin (Figure 2.2). Earthquake focal mechanisms support predominantly normal dip-slip and occasional strike-slip motion near the central basin (Barnhart et al., 2014; Wang et al., 2020a; U.S. Geological Survey, 2021; Saint Louis University, 2021). Similar to the neighboring Rio Grande Rift and southern Rocky Mountains, the Raton Basin has high heat flow, ~90-165 mW/m^2 on average compared to ~65 mW/m^2 for the global continental average (Blackwell et al., 2011; Morgan, 2009). Heat flow can shape the geometry of the seismogenic zone, wherein high heat flow correlates to thinner seismogenic crust (Bonner et al., 2003). Heat flow can also control the style of earthquake clustering, e.g., swarm-like earthquakes correlate to regions of high heat flow and burst-like earthquakes to low heat flow regions (Zaliapin & Ben-Zion, 2016a).

2.3. Data

2.3.1. Seismic

Data from two seismic arrays (Figure 2.2) are used to investigate earthquakes in the Raton Basin from July 2016–July 2020 (Table 2.S1). The first is an eight-station broadband array with ~30 km inter-station spacing and continuous 100 Hz sampling. Seven of the stations were deployed in 2016 (Table 2.S1, UNM1-7). The eighth station, T25A, is a legacy EarthScope Transportable Array station located near the eastern edge of the basin. The second array is composed of 96 Fairfield-Magseis 3-C nodes deployed in the southern portion of the basin from May–June 2018 (Figure 2.2, Table 2.S1). The nodes contain 5-Hz geophones. They were spaced ~2-5 km apart and recorded continuously with a sample rate of 250 Hz.

2.3.2. Wastewater injection

Publicly available wastewater injection volume data are used to investigate spatial and temporal changes in injection volume for the Raton Basin. Public injection records are accessible through online databases by state, i.e., the Colorado Oil and Gas Conservation

Commission (COGCC, 2021) and the New Mexico Oil Conservation Division (NMOCD, 2021). The monthly injection volume is reported for each well in Colorado (CO) since 1998 (COGCC, 2021) and in New Mexico (NM) since 2006 (NMOCD, 2021). We refer to Rubinstein et al. (2014), who used the produced water volume as a proxy for the injection volume, for estimates of the yearly injection volume in NM prior to June 2006. The number of active wells in the basin varies from 24-29 (Figure 2.2). The current metadata indicates that one well (VPR 007) in NM is located ~30 km west of the basin (NMOCD, 2021) but we conclude from the permitting documents that the accurate location of this well is ~200 m northeast of VPR 042. We consider wells located within 250 m of each other to be co-located (Figure 2.2, two purple squares). When considering injection, data from co-located wells are summed.

2.4. Methods

2.4.1. Event detection and location

2.4.1.1. Phase picking and association

A deep neural network package called PhaseNet was used to estimate the probabilities of earthquake P and S arrivals within continuous unfiltered seismic data (Zhu & Beroza, 2019). PhaseNet was trained on >600,000 recordings from the Northern California Earthquake Data Center Catalog and has been successfully applied in many regions (e.g., Liu et al., 2020; Park et al., 2020) including the southern portion of the Raton Basin (Wang et al., 2020a). Phase detections with a probability ≥0.3 for the broadband array (Figure 2.3, e-f) and ≥0.5 for the 1-month node array were passed to the event association step. The 0.3 probability threshold was determined after an analyst visually inspected picks at each station (e.g., Figure 2.3, e-f). The average pick probability for the broadband array was 0.86. For the node array, the 0.5 probability follows the threshold set by Wang et al. (2020a). Events were associated using the Rapid Earthquake Association and Location algorithm (REAL, Zhang et al., 2019) with the 1-D velocity model from Wang et al. (2020a). A minimum of five total phases were required for event association, including at least three P and two S arrivals. Higher thresholds were required during the month of the 96-node array, with ≥50 phases including at least 25 P and 10 S arrivals. A higher probability threshold and a higher requirement for the number of phase picks were set for the nodal seismic data because the primary goal of including this data was to better constrain hypocenters for clusters active during that month rather than to increase the number of earthquake detections. For a focused study on detecting earthquakes during the month of the nodal array see Wang et al. (2020a).

We compared the catalog from the automated approach discussed above to a catalog created by the authors using a manual approach. The manual catalog was built using short-term average to long-term average detections (Allen, 1978; Earle & Shearer, 1994) followed by analyst adjustment of P and S picks. There are ~5,500 earthquakes in the manually refined earthquake catalog from July 2016–May 2019 and ~25,000 earthquakes in the automated catalog for the same time period. Comparing >50,000 picks between the automated and manually refined results reveals that 98% of P and 94% of S phase picks are within one tenth of a second of each other. Manual picks are slightly (0.018 s on average) later relative to the automated machine-learning picks (Figure 2.3a & d). The automated approach results in an ~4.5-fold increase in the number of events detected. Only the catalog built using the automated workflow (PhaseNet, REAL) is considered hereafter.

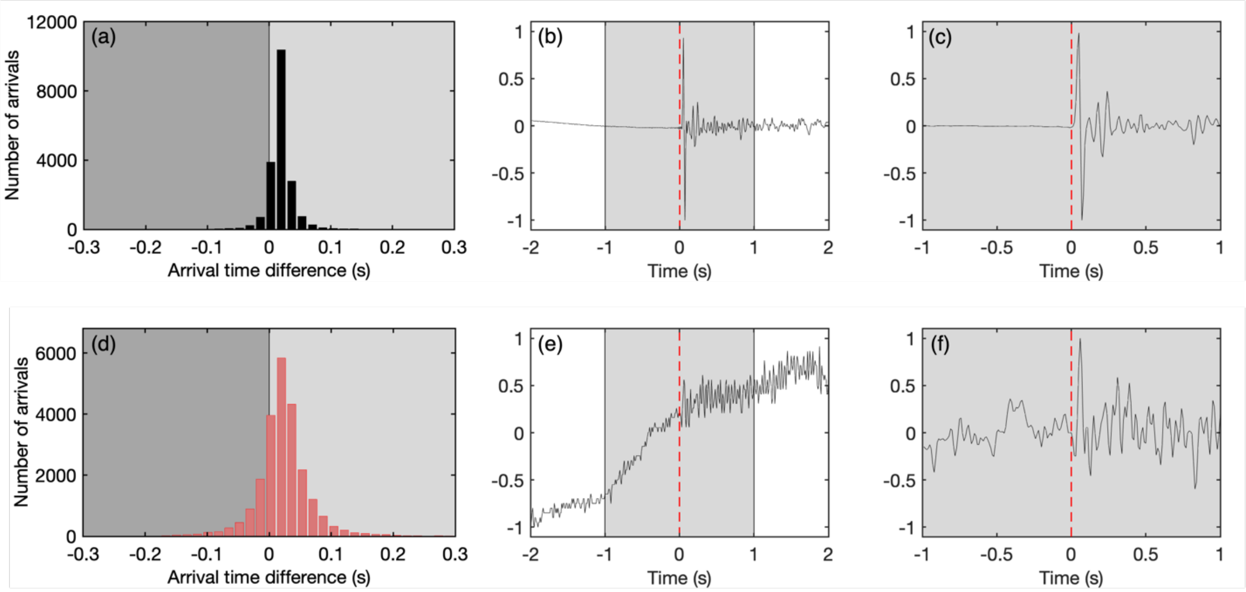

Figure 2.3 PhaseNet earthquake arrival time results and examples. (a) P and (d) S phase distributions of arrival time differences between manual and automated machine-learning approaches. The dark gray and light gray backgrounds indicate when manual picks are relatively early and late compared to automated machine-learning picks, respectively. (b-c, e-f) Normalized waveforms for events with different probability P arrival (red dashed line)

from PhaseNet (Zhu & Beroza, 2019). (b, e) show unfiltered waveforms. (c, f) show zoomed and corresponding waveforms filtered between 1-20 Hz. b-c) high (0.99) and (e-f) low (0.3) probability.

2.4.1.2. Hypocenter estimation

Initial locations from REAL were refined using VELEST, a least-squares absolute hypocenter estimation method (Kissling et al., 1994), with the 1-D velocity model from Wang et al. (2020a). The earthquake catalog with absolute locations from VELEST includes 37,866 earthquakes from July 2016–July 2020 (Figure 2.4a, d).

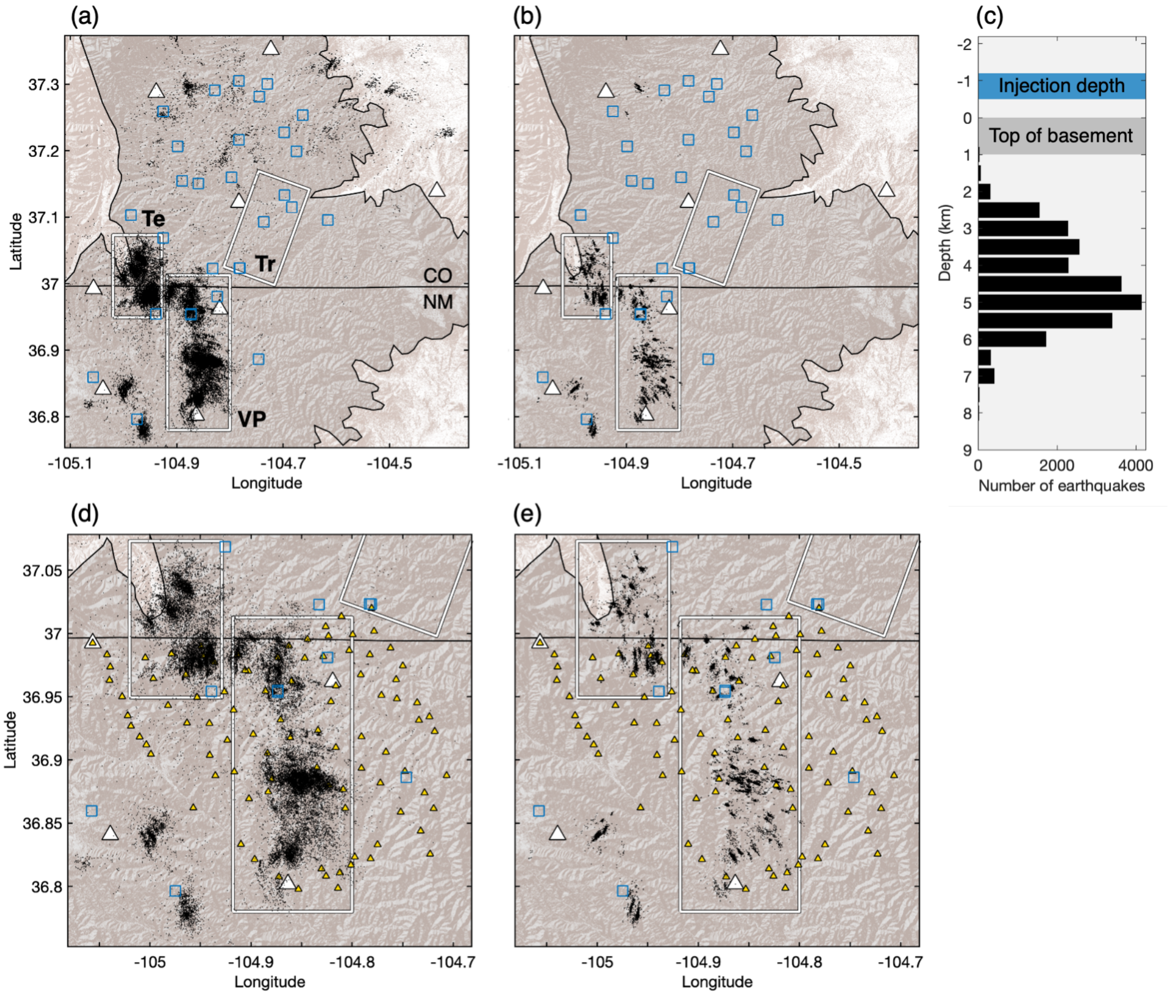

Figure 2.4 Earthquake locations. The basin is outlined in black. The state border is a black line. The white boxes outline regions of seismicity identified by past studies (Nakai et al., 2017; Rubinstein et al., 2014). They are abbreviated Te – Tercio, Tr – Trinidad, and VP –

Vermejo Park in (a). (a) The absolute locations of the ~38,000 earthquake catalog after VELEST (black dots) and (b) the relative relocations of ~23,000 earthquakes after GrowClust (black dots). (c) The depth distribution of relative relocation earthquakes from (b). Sea level is zero km depth. The depth range of the wastewater injection is shaded in blue. The depth range of the top of the basement is shaded in dark gray. (d) and (e) zoom in on the most seismically active regions from (a) and (b) respectively. White triangles are broadband seismometers. Blue squares are wastewater injection wells. Yellow triangles are geophone nodes.

The catalog was relocated using GrowClust (Trugman & Shearer, 2017), which relies on waveform similarity to cluster earthquakes and estimate relative locations with correlation-based differential times. The 1-D velocity from Wang et al. (2020a) was used with GrowClust. Prior to cross-correlation, bandpass filtered (1-20 Hz) waveforms were cut from -1 to 1.5 s for P arrivals and -1 to 2.5 s for S arrivals similar to Trugman and Shearer (2017). Each earthquake was correlated with its 300 nearest neighbors in distance. The East or North horizontal channel with the higher correlation was used for S. A range of cluster connectivity ratios and correlation threshold parameters were tested because they affect the spatial compactness and splitting of hypocenter clusters (see Figure 2.S1 for examples and details). The orientation of earthquake clusters remained fairly consistent between parameter tests (Figure 2.S1). Only event pairs with cross-correlation coefficients ≥0.5 are considered. For final results, the connectivity ratio was set to 0.01 and a minimum of 5 phases with cross-correlation coefficients ≥0.6 were required (Figure 2.4, b & e). Sixty percent (22,684 of 37,866) of the earthquakes were relocated (Figure 2.4b) and GrowClust identified 91 clusters with >50 earthquakes and 46 clusters with >100 earthquakes. Growclust's nonparametric error estimate was used to estimate the relative location error. Under the presumption that the velocity model is correct, the median horizontal and vertical earthquake location errors are 180 m and 240 m, respectively, following 100 bootstrap resamples.

2.4.2. Local magnitude calculation

Three-component waveforms were filtered from 0.01 – 40 Hz, corrected for instrument response, and converted to Wood-Anderson displacement (Uhrhammer & Collins, 1990). Waveforms were cut 0.5 s prior to the P arrival to 3 s after the S arrival for local magnitude (M_L) calculations (Gutenberg & Richter, 1956). To maintain consistency throughout the four-year catalog, only broadband waveforms were considered for magnitude calculation. The maximum three-component vector amplitude (A) in micrometers and the earthquake-station distance (D) in kilometers were used to calculate the local magnitude for each station. The magnitude formula (Gutenberg & Richter, 1956) was calibrated with the 10 largest earthquakes from full waveform moment tensor inversions:

$$M_L = log_{10}(A) + 2.56log_{10}(D) - 4.69$$

The final estimate is the median of all stations M_L for the event.

2.4.3. Fault determination

A two-dimensional principal component analysis (PCA) was used to estimate the strikes of clusters containing 40 earthquakes or more identified by GrowClust. The earthquake-station distance and the small range of earthquake depths (Figure 2.4c) deter us from using three-dimensional PCA to estimate fault dip. Bootstrap resampling with 100 iterations was used to reduce the effect of potential outliers on the PCA results and estimate strike uncertainties. Only mean strikes with one standard deviation <10° were accepted. In addition, clusters where the first principal component was less than two times greater than the second principal component were rejected. In total, 57 clusters passed the criteria for strike estimation (Figure 2.5).

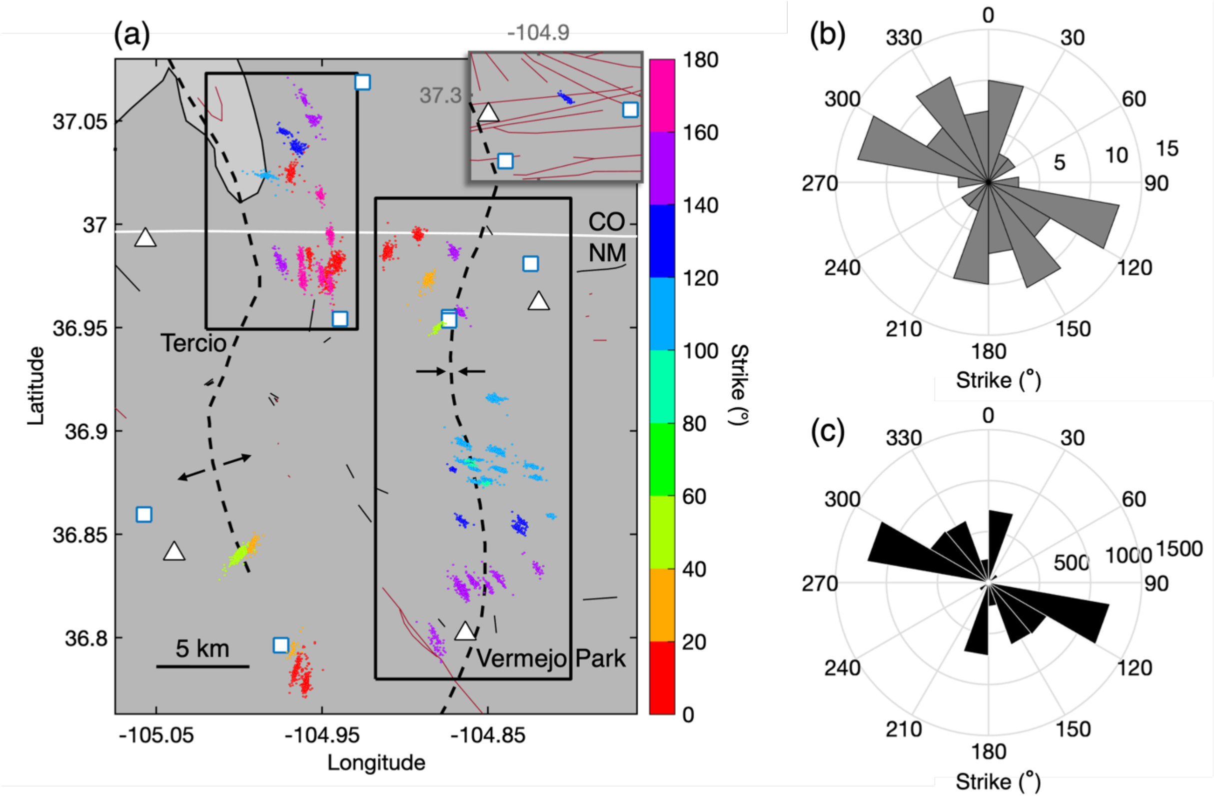

Figure 2.5 Estimated fault orientations. (a) Dots mark earthquake epicenters and the colors correspond to the estimated strike of the epicenter cluster based on the principal component analysis (PCA). The inset shows the single cluster located outside of the main figure region. Surface geology includes faults (thin black lines), dikes (red lines), synclines and anticlines (black dashed lines). The Tercio and Vermejo Park zones (black boxes) are labeled. Triangles are seismometers and squares are wastewater injection wells active during 2016 to 2020. The basin has a dark gray background and a black outline. (b) A summary of the strike distribution of the estimated faults from PCA in (a). (c) The distribution of M_L>0.5 earthquakes from (a) by fault strike. The minimum magnitudes of completeness for the Tercio zone and Vermejo Park zones are 0.1 and -0.2, respectively. (b-c) are symmetric, e.g., the 0-20° bin is equal to the 180-200° bin.

2.4.4. Source mechanism constraints

Deviatoric moment tensors were estimated for 27 M≥2.8 earthquakes, which produced low-frequency waveforms suitable for inversion with the Time Domain Seismic Moment Tensor (TDMT) package (Dreger, 2003). The same 1-D velocity model used for hypocenter estimation (Wang et al., 2020a) was used to calculate a Green's function library for TDMT inversions. A frequency band of 0.08-0.4 Hz was used, and the window length varied between 10 to 15 s, depending on the source-receiver distance. The parameter choices were adopted from previous studies in a similar setting (e.g., Wang et al., 2016, 2018). Although only 8 stations are available, they are all within ~50 km and approximately evenly distributed so azimuthal gaps are limited for events within the Raton Basin. Even the 2 out of 27 events inverted with 4 stations showed mechanisms comparable to those estimated from larger events nearby. During the fitting of deviatoric moment tensors (i.e., no volumetric component), the average variance reduction for TDMT inversion results is 66% and the highest is 90%. Event epicenters were taken from the newly developed catalog and depths were independently optimized based on a grid-search with 1-km increments. The depths estimated with moment tensor inversions are consistent with the catalog, with a mean difference of 0.26 km (± 1.58 km).

Some highly active clusters did not host any M≥2.8 events during the study period and therefore, do not have moment tensor solutions. These clusters were investigated with focal mechanism estimates using first-motion polarities (i.e., FOCMEC; Snoke, 2003). One area targeted for first-motion focal mechanism analysis was the concentration of hypocenter clusters with strikes of ~100° located in the center of the previously identified ~N-S Vermejo Park zone (Figure 2.5). Additionally, two prominent clusters within the Tercio zone (Figure 2.5) were investigated. As a result, four additional focal mechanisms are included in Figure 2.6 (purple beach balls). These events with M_L from 1.26-2.33 provided between 70-92 clear first-motion polarity picks (Figure 2.S2).

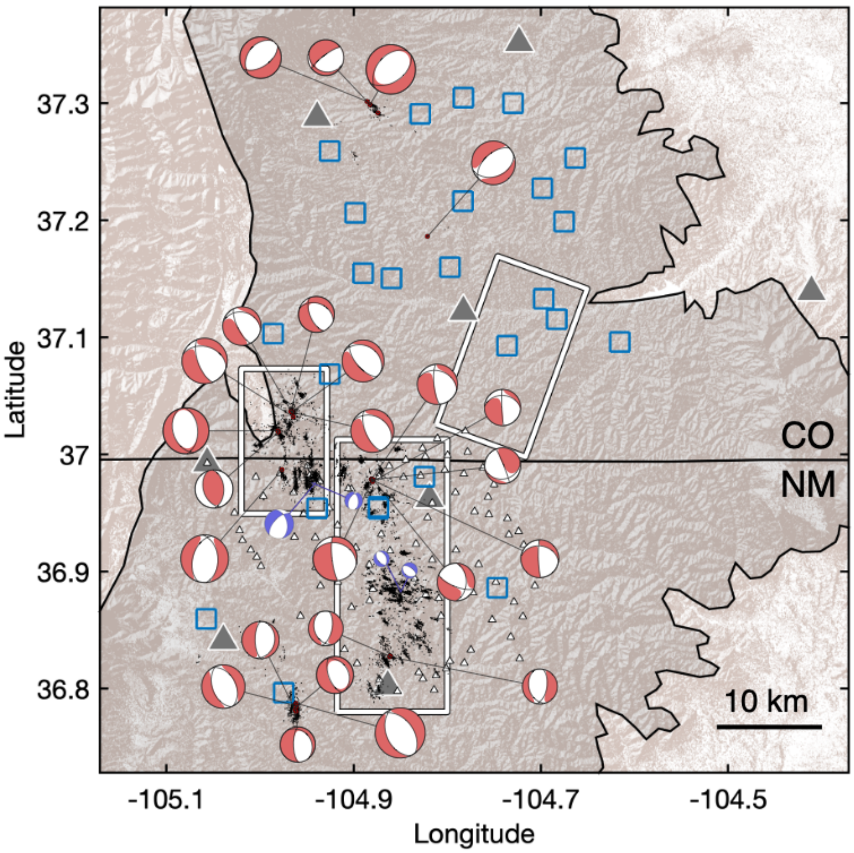

Figure 2.6 Source mechanism constraints. Deviatoric moment tensor inversion (red and white) resolved from broadband station (gray triangles) recordings. First-motion polarity based focal mechanism inversion results for four smaller magnitude events (purple and white) were resolved using nodal station (small white triangles) recordings. The size of the beachball symbols scales with M_L from 1.26-3.99. From east to west, white boxes mark the Trinidad, Vermejo Park, and Tercio zones. Blue squares are the active wastewater injection wells between 2016-2020. The apparent inconsistency between the moment tensors and hypocenter cluster near 37.3° N is discussed in section 2.5.2.

2.4.5. Statistical analysis

The statistical behavior of earthquakes in a region have been used to discriminate between induced and tectonic sequences (e.g., Zaliapin & Ben Zion, 2013, 2016b; Schoenball et al., 2015; Mousavi et al., 2017). A variety of statistical analyses were used to investigate how Raton Basin seismicity is distributed in magnitude, time, and space. Each approach was applied to the full basin and three subregions: the northern basin, the Tercio zone, and the Vermejo Park zone (Figure 2.7). The additional earthquake detections from using the nodal array were not considered to maintain spatiotemporal and magnitude consistency throughout the catalog. The frequency-magnitude distribution is considered first to estimate magnitude of completeness (M_c) and the slope of the decay in earthquake frequency with increasing magnitude (b-value). M_c and b-value were estimated using the maximum curvature method (Wiemer & Wyss, 2000). We note the maximum curvature method may underestimate M_c by 0.1 (Woessner & Wiemer, 2005). The 95% confidence intervals of b-values were calculated using ZMAP (Wiemer, 2001; Reyes & Wiemer, 2020). A b-value of ~1 is expected given the Gutenberg-Richter law but has been suggested to deviate in regions of high heat flow and/or where fluids are present, including subduction zones, volcanic settings, geothermal fields, and oil and gas fields (Bachman et al., 2012; van Stiphout et al., 2009; Mousavi et al., 2017; Goebel et al., 2016; Roberts et al., 2015; Farrell et al., 2009). Only earthquakes with magnitudes greater than each region's M_c (Figure 2.8a) are included in the subsequent statistical assessments (e.g., Figure 2.8c-d).

Spatiotemporal and magnitude clustering of earthquakes were investigated using three approaches: interevent time distributions (Kagan & Jackson, 1991), optimized Epidemic Type Aftershock-Sequence models (ETAS; Ogata, 1988; Harte, 2010), and nearest neighbor space-time distributions (Baiesi & Paczuski, 2004; Zaliapin & Ben-Zion, 2013, 2016b; Schoenball et al., 2015). First, interevent times and the coefficient of variation (C_V) indicate the degree of temporal clustering of earthquakes. The interevent time is the time (in seconds) between events and the C_V is the standard deviation divided by the mean of interevent times. A C_V of 1 indicates a Poissonian process (e.g., independent or background seismicity), $C_V>1$ indicates temporal clustering of seismicity (e.g., earthquake-earthquake interactions), and $C_V>4$ indicates highly clustered earthquakes (Kagan & Jackson, 1991; Schoenball & Ellsworth, 2017b; Cochran et al., 2018). A range in the degree of temporal clustering has been observed for regions of induced seismicity, including near-Poissonian to highly clustered (Cochran et al., 2018; Skoumal et al., 2020) and these temporal behaviors could reflect different processes driving the seismicity. For example, Cochran et al. (2018) observed lower C_Vs from earthquake families close to high-volume injection and suggested these sequences are driven directly by pore fluid pressure increases; in contrast, high-C_V

clusters further from wells are highly clustered and imply strong earthquake-earthquake interactions.

The second approach, ETAS modeling, considers event magnitude and time as it predicts the earthquake rate of a stationary Poisson process plus time-decaying aftershocks. We use the ETAS model proposed by Ogata (1988) and updated by Harte (2010) wherein the rate of occurrence of the entire earthquake sequence at time t based on the history of occurrence ($Ht = \{(t_i, M_i); t_i < t\}$) is:

$$\lambda(t|Ht) = \mu + K \sum_{i:t_i<t} e^{\alpha(M_i-M_c)} \left(1 + \frac{t-t_i}{c}\right)^{-p}.$$

Here, t_i is the time of the i^{th} event with magnitude M_i and M_c is the magnitude of completeness for each considered region in our study. The parameters, K, c, and p describe the frequency of aftershocks, wherein, K is the aftershock productivity and c and p are the Omori-Utsu parameters for the temporal decay of seismicity following the mainshock (Omori, 1894; Utsu, 1961). The K for this study follows Harte (2010) and is equal to K_0c^{-p} from the Ogata (1988) study. The parameter α measures the efficiency of an earthquake of a given magnitude to trigger aftershocks (i.e., large α for earthquake swarms which lack typical aftershock behavior). Lastly, μ is the background seismicity rate (i.e., the forcing rate), which is assumed to be stationary for short time scales but has been found to correlate temporally with injection operations in some induced seismicity settings (e.g., Brodsky & Lajoie, 2013). The ETAS parameters are determined when a minimum tolerance of 0.001 is reached during optimization. Many studies focus on the time-dependent changes of ETAS parameters (Hainzl & Ogata, 2005; Lei et al., 2008) but Llenos & Michael (2013) suggest the absolute values of ETAS parameters could be a way to differentiate between natural earthquakes and anthropogenically induced earthquakes. Induced seismicity may have higher values of K and μ and natural seismicity may have lower values of α (Llenos and Michael, 2013).

Finally, nearest neighbor distance (NND) distributions in the space-time-magnitude domain are indicative of the independent and/or clustered nature of an earthquake sequence or a region's seismicity. We calculate NND in the space-time-magnitude domain (Baiesi & Paczuski, 2004) for each pair of events i and j using the following equation:

$$\eta_{ij} = \begin{cases} t_{ij}\left(r_{ij}\right)^{d} 10^{-bm_i} & , t_{ij} > 0; \\ \infty & , t_{ij} \leq 0, \end{cases}$$

where t_{ij} is the interevent time (year), r_{ij} is the interevent distance (km), d is the dimension of the earthquake hypocenter distribution, b is the b-value, and m_i is the i^{th} event's magnitude (Zaliapin & Ben-Zion, 2013; Schoenball et al., 2015). We set $b = 1$ based on our b-value results discussed in section 5.3 and we set $d = 1.6$ (Zaliapin & Ben-Zion, 2013; Vasylkivska & Huerta, 2017; Cochran et al., 2020). Both Schoenball et al., (2015) and Zaliapin & Ben-Zion (2013) find the variation of d within 0.5 units of its true value does not significantly affect their results. Following Zaliapin et al., (2008), we can separate the η_{ij} equation into rescaled distance (R_{ij}) and rescaled time (T_{ij}) components where:

$$R_{ij} = \left(r_{ij}\right)^{d} 10^{-bm_i/2},$$

$$T_{ij} = \left(t_{ij}\right)^{d} 10^{-bm_i/2},$$

and

$$\eta_{ij} = R_{ij}T_{ij}.$$

For an ETAS-like earthquake sequence the NND distribution is bimodal with a signal at shorter rescaled distances indicating clustered behavior and a signal at larger rescaled distances indicating independent background behavior (Zaliapin et al., 2008). For NND results in Figures 2.7-2.8, the relocated earthquake catalog was used except for in the case of the northern basin, where only a small number of events (~280) were accepted for relative relocation (Figure 2.S3d). A comparison between NND results using absolute locations and relative relocations for each region can be found in Figure 2.S6. A higher ratio of background to clustered seismicity has been found in some induced settings (Zaliapin & Ben Zion, 2016b; Schoenball et al., 2015; Cochran et al., 2020) compared to tectonic settings. Also, the presence of repeaters, earthquakes that occur at short rescaled distances and long rescaled times, are suggested as an induced seismicity signal (Kraft & Deichmann, 2014; Zaliapin & Ben Zion, 2016b). In addition to the type of seismicity (e.g., induced, tectonic), geologic setting is suggested to affect the spatiotemporal-magnitude statistics (Martinez-Garzon et al., 2018; Vasylkivska & Huerta, 2017). We use NND distributions to compare the Raton Basin to regions of tectonic seismicity and other regions of induced seismicity.

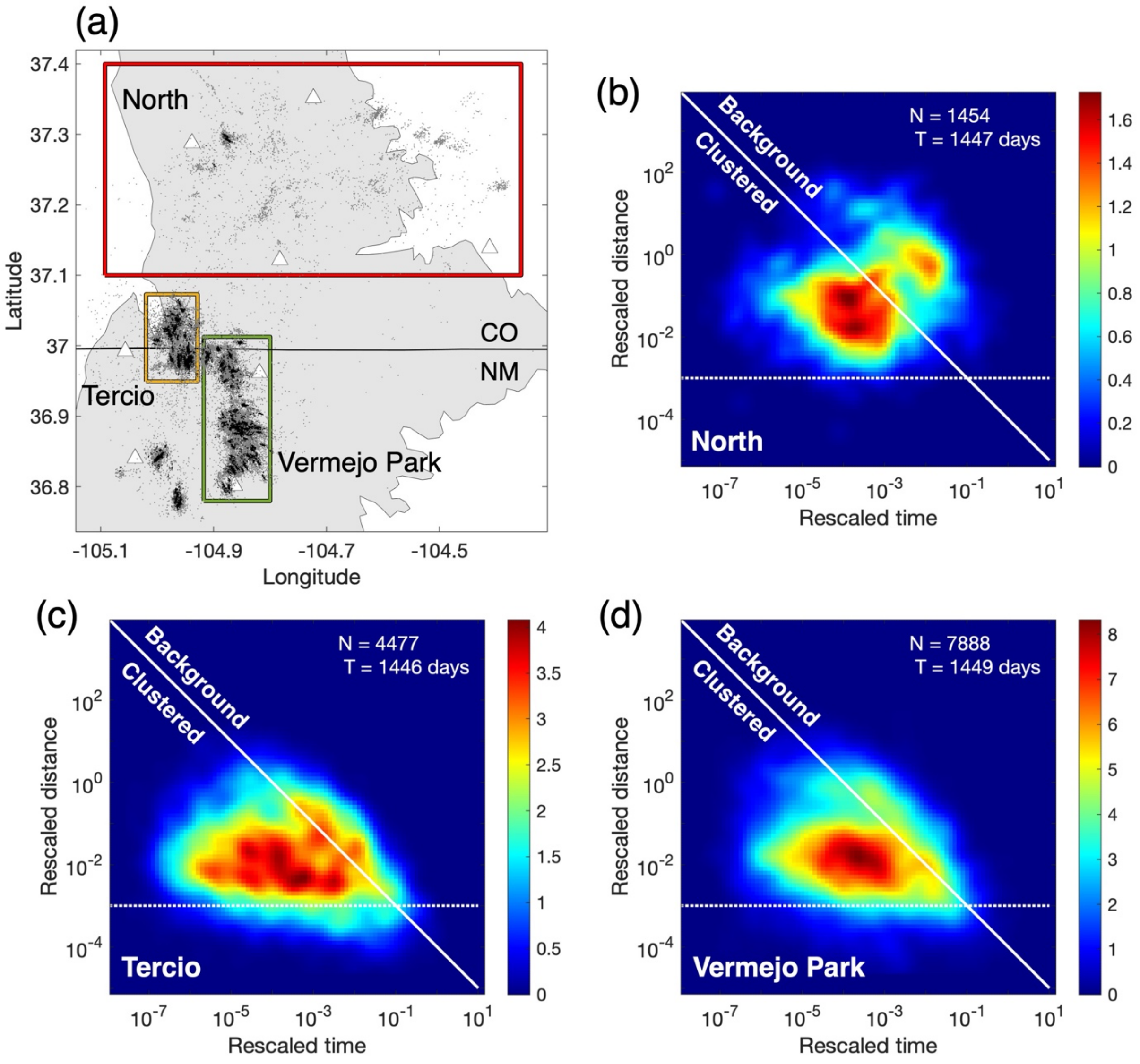

Figure 2.7 Nearest neighbor time-distance distributions for seismicity in subregions of the Raton Basin. (a) Map of earthquakes and subregions: North subregion outlined in red, Tercio zone outlined in yellow, and Vermejo Park zone outlined in yellow. Absolute epicenters are gray dots and relative epicenters are black dots. Seismometers are white triangles. (b-d) The nearest neighbor distribution results for each subregion. The subregion is labeled in bottom right of each plot. Absolute locations were used for the results shown in b and relative relocations for the results in c-d. The color bar indicates the number of event

pairs at a given rescaled distance-time. The number of earthquakes, N, and the time period, T, is printed on each figure. The diagonal white line represents a stationary behavior, wherein rescaled distance ($\boldsymbol{R_{ij}}$) by rescaled time ($\boldsymbol{T_{ij}}$) equals a constant. The horizontal white dotted line represents a constant rescaled distance. Consistent lines are used for all NND figures for direct comparisons.

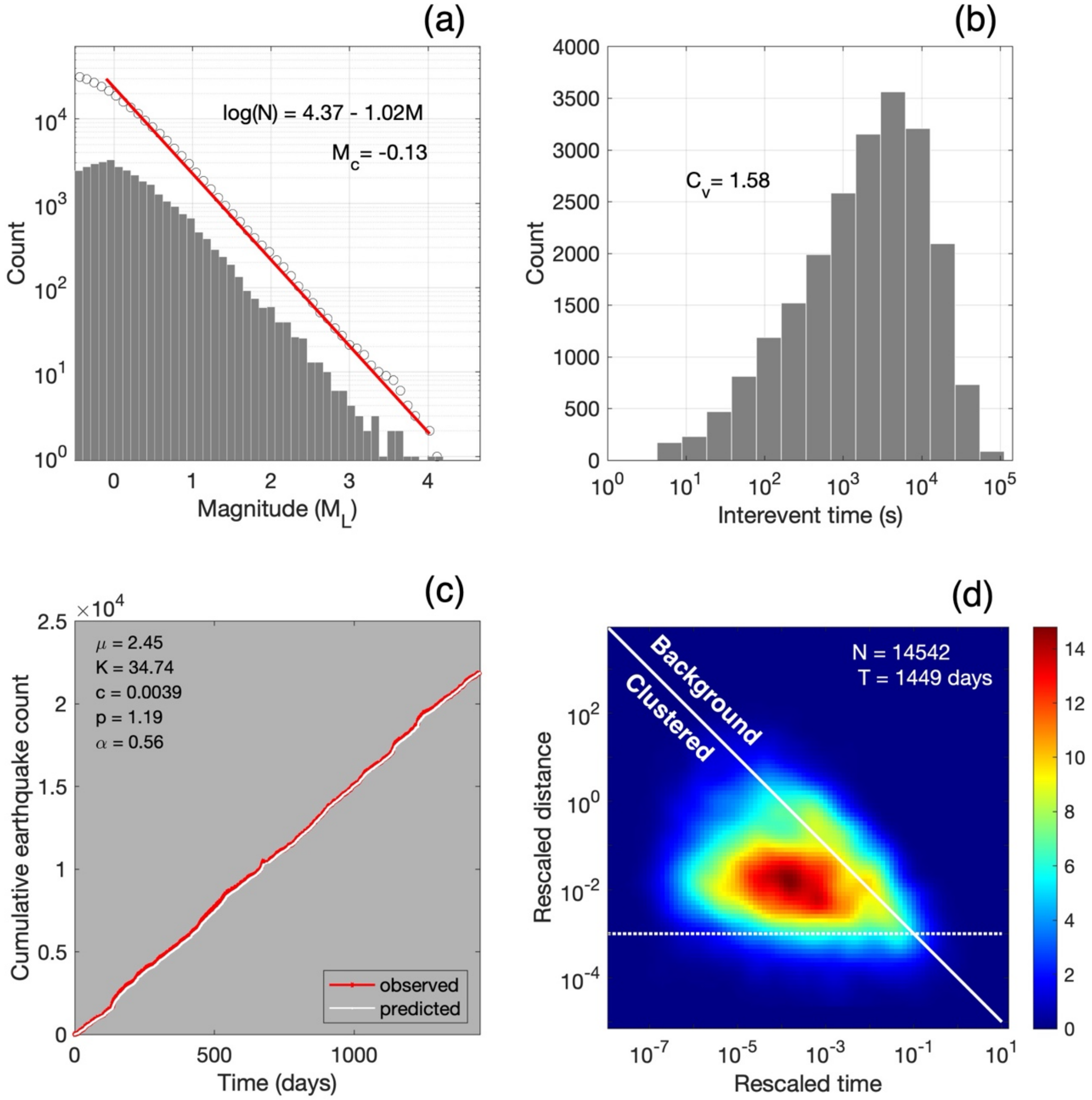

Figure 2.8 Raton Basin frequency-magnitude and spatiotemporal statistical results. (a) Earthquake frequency-magnitude histogram (gray bars; noncumulative) and cumulative earthquake distribution (gray circles). The red line approximates the best least squares fit to

the Gutenberg-Richter relation above the minimum magnitude of completeness (M_c). (b) Interevent time histograms. The average coefficient of interevent time variation (C_v) is printed. (c) Cumulative number of earthquakes versus the number of days from observed seismicity (gray) and Epidemic Type Aftershock-Sequence (ETAS) modeling (black line). ETAS maximum likelihood parameter estimates are printed (Ogata, 1988). (d) Nearest-neighbor rescaled time-distance distribution. The color bar indicates the number of event pairs at a given rescaled distance-time. The diagonal white line represents a stationary behavior, wherein rescaled distance ($\boldsymbol{R_{ij}}$) by rescaled time equals a constant ($\boldsymbol{T_{ij}}$). The horizontal white dotted line represents a constant rescaled distance. Consistent lines are used for all NND figures for direct comparisons.

2.5. Results

2.5.1. Spatial clustering of hypocenters

The majority of hypocenters are tightly clustered in geometries consistent with earthquake activity on unmapped basement faults ~2.5–6 km below sea level (Figure 2.4c). Absolute earthquake locations are heavily concentrated in the central to southern basin with 90% of earthquakes (~34,000) south of 37.05 latitude (Figure 2.4a). The absolute earthquake locations (Figure 2.4a, d) collapse into dense elongated clusters after relative relocation (Figure 2.4b, e). Two of the three previously identified fault zones, the Tercio and Vermejo Park zones (Figure 2.2, Figure 2.4), are active during our study period, similar to the 2008-2010 study by Nakai et al. (2017a). Very few earthquakes were detected in the Trinidad zone. Small seismically active zones were identified in the southwest and northwest of the basin by absolute and relocated epicenters (Figure 2.4a-b). One of the southwestern clusters was previously identified by Wang et al. (2020a) using only one month of nodal data. Absolute hypocenters are sparsely distributed in the remainder of the northern basin, however all but the northwestern group were culled by the relocation criteria.

Application of a PCA to the relocated earthquake epicenters indicates 57 short (<3 km long) faults (Figure 2.5a). The majority of the faults (48 out of 57) strike from approximately WNW to slightly east of north (Figure 2.5b). WNW-ESE striking faults are the most seismogenic, hosting ~33% of the total $M_L \geq 0.5$ earthquakes in Figure 2.5c.

2.5.2. Source mechanism constraints

Most focal mechanisms from full moment tensor inversion and first motion polarities are consistent with the regional scale normal faulting regime (Lund Snee & Zoback, 2020), with a few exceptions showing oblique or reverse regimes (Figure 2.6). The strike orientations vary from NE to WNW from north to south. More heterogeneous strikes are observed near the boundary of New Mexico and Colorado (Figure 2.5-6). In general, the strikes estimated from the PCA (Figure 2.5) and potential fault planes from focal mechanisms (Figure 2.6) are comparable in the central to southern basin where most seismicity occurs, and the seismograph distribution minimizes azimuthal gaps. Several oblique mechanisms and one reverse faulting mechanism are in the central to southern basin (Figure 2.6). The reverse event is located in the middle of the Tercio zone. Most other events in the Tercio zone indicate ~NW striking normal faults. Oblique mechanisms are more prevalent near the transition between the Tercio and Vermejo Park zones. Most mechanisms farther south within the middle to southern portion of the Vermejo Park zone indicate WNW to N normal faults (Figure 2.5-2.6).

A notable example of inconsistency between the moment tensor and the PCA results is found for one fault near the northern edge of the array, ~37.3° N (Figure 2.6). Its PCA strike estimate is NW, and its moment tensor strike estimate is NE (Figure 2.5a inset & Figure 2.6). The different strikes of the PCA and moment tensor analysis could be explained by the activation of non-optimally oriented faults through large pressure perturbations, tens of MPa, as has been suggested for the 2014 M_W 4.9 Milan, Kansas earthquake (Joubert et al., 2020). However, given the location near the edge of the array the epicenters may be biased by limited azimuthal coverage in which case the PCA strikes could be incorrect. The three-component waveform-based moment tensor estimate of strike is preferred in this location. Additionally, maximum compressive stress indicators near 37.3° N show orientations of ~NNE-NE (Figure 2.2; Lund Snee & Zoback, 2020), which would be consistent with a ~NE striking normal fault.

2.5.3. Frequency, magnitude, and temporal clustering statistics

Space-time-magnitude statistics are calculated for the full basin and three subregions: the northern basin, the Tercio zone, and the Vermejo Park zone (Figure 2.7-2.8; 2S.3-2S.6). The M_c varies spatially due to station coverage (Figure 2.S3-2S.5). Although $M_c = -0.13$ for the entire catalog (Figure 2.8a), we conservatively suggest that the catalog is complete to ~M_L 0.6 since this was the maximum M_c of the subregions (Figure 2.S3-2S.5). However, the following statistical results were all derived using earthquakes with M_c unique to each considered region. The maximum magnitude during our study is M_L 4.2. The b-value for the entire study region is 1.03 (Figure 2.8a) and its 95% confidence interval (CI) is 0.95-1.09. The b-values of the three subregions are 1.07 (0.57-1.58 95% CI) for the north, 0.98 (0.90-1.07 95% CI) for the Tercio zone, and 1.05 (1.047-1.054 95% CI) for the Vermejo Park zone (Figure 2.S3a-S5a).

Interevent times range from ~$10^1 – 10^5$ s and the full basin C_v is ~1.6 (Figure 2.8b) indicating low to moderate temporal clustering of the seismicity. The C_v of each subregion is slightly higher than the full basin, ~1.8 for Vermejo Park, ~1.9 for Tercio, and ~2 for the north (Figure 2.S3b-2.S5b). The C_v values for induced earthquakes in Oklahoma and southern Kansas range from ~1-10 (Schoenball et al., 2017b; Cochran et al., 2018) implying a variety of temporal clustering from little or none to highly clustered. We find a narrower range of results with C_v values from ~1.6-2 indicating low to moderate temporal clustering and no significant variation between regions at the temporal and spatial scale considered.

ETAS modeling visually fits the observed seismic rate for the full basin (Figure 2.8c), as well as the Tercio and Vermejo Park regions (Figure 2.S4c, 2.S5c). This demonstrates that most of the observed seismicity in the Raton Basin can be modeled by time-independent events and subsequent aftershocks. A minor exception is that for the northern subregion, ETAS often underpredicts the seismic rate (Figure 2.S3c) indicating the observed rate has even higher productivity of earthquake-earthquake interactions than predicted by ETAS. The decay parameters (c and p) are comparable between the subregions and consistent α were observed across the multiple subregions, indicating similar magnitude productivity (Figure 2.S3c-2.5c). The productivity values (K as defined by Harte, 2010) for the southern sections, ~32-40, are orders higher than that of the northern section (4), echoing differences in the number of events observed during the same four-year period. The full-basin statistics, as a result, are dominated by the southern sections (i.e., Tercio and Vermejo Park), characterized by steady seismicity rate over the four years studied. Although there are variations in the injection volume and rate in each considered subregion (Figure 2.S7), we did not observe significant differences in the μ parameters, which often reflect the forcing rate from external contribution (e.g., Llenos & Michael, 2013; 2016; Kothari et al., 2020). The invariance of μ with injection strategies (and the other four parameters), however, does not imply the natural origin of the seismicity, but rather implies a complex (i.e., non-linear) and delayed response between the injection activities and earthquake rates and/or that the tectonic forcing is more dominant than the forcing from fluid injection.

NND distributions for the full basin (Figure 2.8d) are slightly bimodal with the largest concentration of event pairs at short space-time distances corresponding to clustered seismicity and a smaller distribution along a constant slope corresponding to independent background seismicity. NND distributions for the three subregions (Figure 2.7c-d) also exhibit a strong clustered behavior and comparatively weak independent behavior. The dominance of the clustered mode at 10^{-2} rescaled distance and 10^{-4} rescaled time in Figure 2.8d is similar to the results for the induced setting of southern Kansas and Oklahoma (Schoenball & Ellsworth, 2017b; Verdecchia et al., 2021) and the mixed (induced and tectonic) setting of the Salton Sea geothermal area (Zaliapin & Ben Zion, 2016b). But our results are dissimilar from some induced seismicity settings where strong ratios of background to clustered signals have been identified (Cochran et al., 2020; Schoenball et al., 2015; Zaliapin & Ben Zion, 2016b). The northern region (Figure 2.7b) exhibits the clearest separation between the clustered and background mode. However, poorly constrained absolute locations can lead to artifacts at large rescaled space-time distances (Zaliapin & Ben-Zion, 2015). The Vermejo Park zone exhibits the highest ratio of clustered to background signal and its NND pattern dominates the full basin NND distribution (Figure 2.7d, Figure 2.8d). A repeater signal may be present for the Vermejo Park zone appearing as a lobe in the bottom right of Figure 2.7d, but it is not apparent for the other considered regions (Figure 2.8d, Figure 2.7b-c).

2.6. Discussion

2.6.1. Basement fault systems beneath the Raton Basin

The spatial distribution of seismicity in the new catalog provides evidence for local variability of fault orientations that is not apparent in prior work using the EarthScope Transportable Array (Nakai et al., 2017b) or short-term aftershock deployments (Rubinstein et al., 2014; Barnhart et al., 2014). Prior work indicated primarily N to NNE striking normal faulting earthquakes (Rubinstein et al., 2014; Barnhart et al., 2014; Nakai et al., 2017b), which were grouped into three zones of seismicity ~10-20 km in length: the Trinidad, Vermejo Park, and Tercio zones (Figure 2.2). During 2016-2020, the Vermejo Park and Tercio zones were much more active than the Trinidad zone, whose activity has greatly diminished since hosting a M_W 5.3 event in 2011 and continued to diminish from 2016 to 2020 (Figure 2.9e). Primarily using EarthScope Transportable Array data with ~70-km station spacing, Nakai et al. (2017b) suggested that the Vermejo Park and Tercio zones were long (~10-20 km) N-S normal faults. With the local array catalog from 2016 to 2020, we find 57 shorter faults across the Raton Basin with variable strikes (Figure 2.5) and faulting regimes (Figure 2.6). Most of these short faults are concentrated in the Vermejo Park and Tercio zones, where discrete faults with lengths of ~1-3 km combine to form the previously identified broader zones of seismicity. The nearly contiguous seismicity between the Tercio and Vermejo Park zones suggests their activity may be linked. These multi-scale fault zone structures are similar to but more extensive than earlier suggestions of en echelon faults within the Trinidad zone near the time of the 2011 M_W 5.3 earthquake sequence (Rubinstein et al., 2014).

A potential implication of the multi-scale fault zone structure is that the maximum potential earthquake magnitude may be smaller if there are no continuous faults that span the ~20 km long Vermejo Park zone or ~10 km long Tercio zone. However, ruptures may span multiple nearby fault segments (e.g., Landers earthquake, Li et al., 1994; and Hector Mine earthquake, Treiman et al., 2002) such that the maximum fault length is not a reliable predictor of the maximum earthquake magnitude. Such co-slipping of en-echelon fault systems has been observed for induced seismicity in Alberta, Canada (M_W 4.1, Wang et al., 2018) and east Texas (M 4.8, Wang et al., 2020b). Within the Raton Basin, the largest earthquake since the beginning of injection was the M_W 5.3 Trinidad event with a geodetically estimated rupture length of ~8-10 km (Barnhart et al., 2014), which is shorter than the ~14 km total length of the Trinidad zone of seismicity (Rubinstein et al., 2014; Meremonte et al., 2002). A local seismic network was not in place prior to the M_W 5.3 event therefore it is unclear whether it ruptured one fault or multiple shorter faults, but the aftershock locations suggest the presence of multiple segments with strikes rotated closer to North, instead of the orientation of the composite Trinidad zone of seismicity (Figure 2.9a; Rubinstein et al., 2014).

The changes in fault orientation (Figure 2.5) and evidence of different slip regimes (Figure 2.6), specifically along the CO-NM border, indicate either stress conditions that change over short-length scales (~5-10 km) or stress perturbations that are sufficient to reactivate non-optimally oriented faults. A stress rotation from N-S maximum horizontal stress in the mid to northern basin to E-W at the southeastern edge (Figure 2.2) may help explain the variable strikes (Lund Snee & Zoback, 2020; Wang et al., 2020a) but there are no stress measurements for comparison in the most seismically active parts of the central to southern basin. Alternatively, the regional stress field may be modified by local stresses or earthquakes may occur on non-optimally oriented faults, as observed in some areas of fluid injection. Such stress perturbations are often observed from high-rate injections like hydraulic fracturing (e.g., Shen et al., 2021) or geothermal exploitations (e.g., Martinez-Garzon et al., 2016). At maximum injection pressures for the Geysers geothermal field, a range of fault orientations are activated including non-optimally oriented faults at maximum injection pressure (Martinez-Garzon et al., 2016). We generally observe more variable fault orientations closer to wastewater injection wells (e.g., the CO-NM border, Figure 2.5a). Non-optimally oriented faults in Oklahoma and Kansas are suggested to reactivate from either high pore pressure increase or potentially static stress changes from nearby seismogenic faults (Joubert et al., 2020; Sumy et al., 2014). A systematic investigation of fault orientations, injection rates, and static stress changes would provide further insights into the driving mechanism(s) of the induced seismicity.

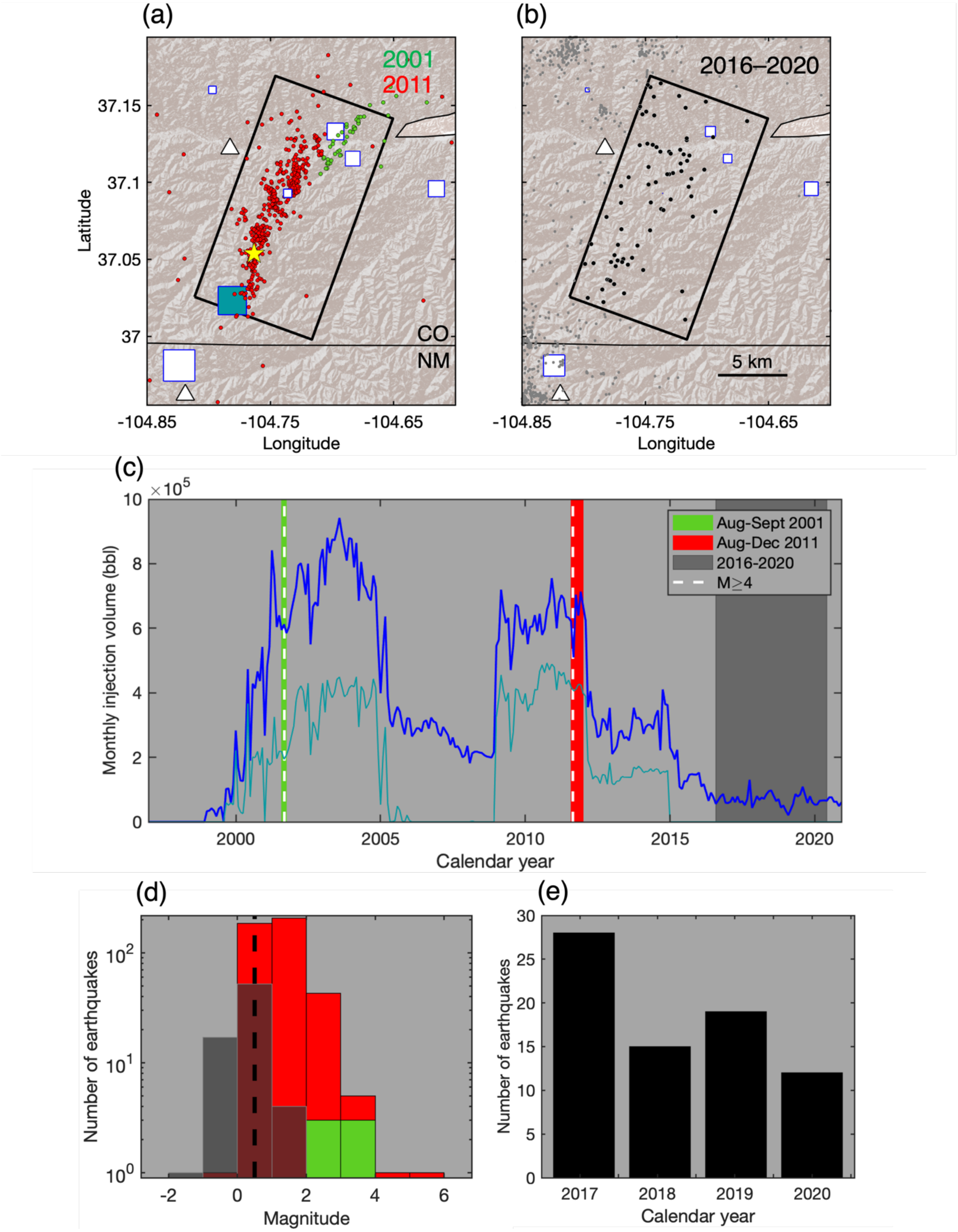

Figure 2.9 Evolution of Trinidad zone seismicity. (**a-b**) Maps of earthquakes in the Trinidad zone (black box) from (**a**) Aug–Dec 2001 (green, Meremonte et al., 2002), Aug–Dec 2011

(red; Rubinstein et al., 2014) and (**b**) our July 2016–July 2020 catalog (black and gray). Seismometers are white triangles. Wastewater injection wells are squares and are scaled by average injection volume from 2008-2012 for (a) and from 2016 to 2020 for (b). The yellow star is the 2011 M_w 5.3 earthquake epicenter. (**c**) The total monthly wastewater injection volume within the Trinidad zone is shown in dark blue. The turquoise monthly wastewater injection volume is for two co-located wells shown as a turquoise well in (a). Shaded regions indicate times of earthquake studies, see legend. White dashed lines are M≥4 earthquakes from the USGS catalog within 10 km of the Trinidad zone. (**d**) Earthquake magnitudes for each catalog within the Trinidad zone. Legend colors from (c) apply to (d). Black dashed line marks the minimum magnitude of completeness for our 2016-2020 catalog. (**e**) Number of earthquakes per year within the Trinidad zone for our catalog shown in (b).

2.6.2. Evolution of wastewater injection and seismicity

2.6.2.1. Full basin summary

The seismogenic faults from this study are located in the basement similar to previous studies of Raton Basin seismicity (Nakai et al., 2017b; Rubinstein et al., 2014) as well as Oklahoma and Kansas (Schoenball & Ellsworth 2017a). Permeable pathways, such as faults, provide a potential link between shallow wastewater injection and reactivated basement faults under the Raton Basin (Nakai et al., 2017b). In the Raton Basin mapped faults and intrusions are observed at the surface and basement faults are inferred from earthquake locations but there are no direct observations of permeable pathways that connect the injection reservoir to the basement. However, mantle-derived helium often found in geothermal springs along faults at locations near the Raton Basin, e.g., Sheep Mountain and Bravo Dome, suggests that permeable connections between mantle depths and Earth's surface are common in this region of the southern Rocky Mountains (Karlstrom et al., 2013). Additionally, Hemborg (1998) alludes to higher productivity of coal bed methane beds closer to faults in the Spanish Peak field wells suggesting the potential for enhanced permeability within the basin sediments.

To understand the evolution of wastewater injection, we examine the average monthly injection for three four-year time periods in the Raton Basin (Figure 2.10). The wastewater injection record by well is complete from 2006-2020. Similar to Weingarten et al., (2015), we consider injection ≥300,000 bbl/month as high-rate, <100,000 bbl/month as low-rate, and rates between as moderate. The total injection volume in the Raton Basin for the considered time periods decreases chronologically from 2008 to 2020 (Figure 2.10a-c). The number of high-rate injection wells decreased from two during 2008-2012 to zero from 2012-2020 (Figure 2.10). Injection rate declined in the south and central basin from 2008-2020 and is more evenly distributed across the basin by 2016-2020 (Figure 2.10). The northernmost well and two wells just south of the state border remain moderate- to high-rate injectors during all considered time periods. During our earthquake catalog from 2016 to 2020, these three wells operate at >170,000 bbl/month and in total 6 wells are moderate-rate injectors. Similar injection rates, >150,000 bbl/month, were reported for all wells associated with induced seismicity for the Barnett Shale in Texas but some wells operated at this rate with no associated seismicity (Frohlich, 2012).

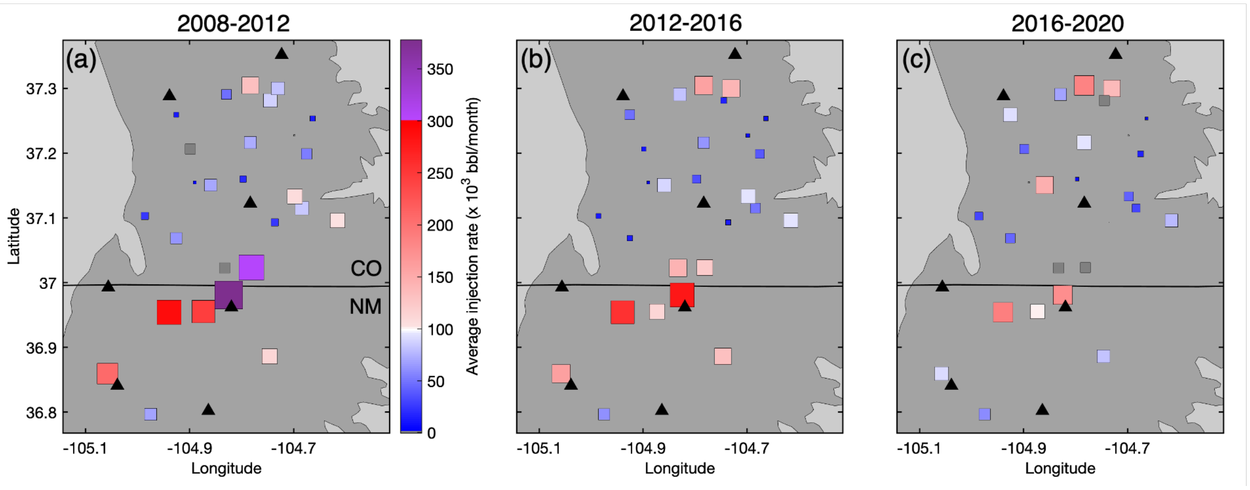

Figure 2.10 The average monthly wastewater injection volume during three time periods indicated by the titles for a-c. The color bar from (**a**) can be used for (**b-c**). Purple indicates high-rate (>300,000 bbl/month), red indicates moderate-rate (100,000-300,0000 bbl/month), and blue indicates low-rate injection wells (<100,000 bbl/month). Squares scale with the average injection volume and are consistent between figures. Gray squares indicate wells with no reported injection volume. Black triangles are seismometers. The Raton Basin is outlined in black.

Greater than 90% of earthquakes occur less than 10 km from the nearest wastewater disposal well from 2016 to 2020 (Figure 2.11) with an average earthquake to well distance of 5.8 km. Given the proximity of seismicity to injection wells, pore fluid pressure increases are a likely driver of fault reactivation, but it is not certain how pore fluid pressures are transmitted to basement depths. Although our earthquake depths taper off near the top of the basement (Figure 2.4c), it is likely permeable conduits, such as faults, extend upward from the basement into the basin sediments. Previous pore fluid pressure modeling along a permeable fault in the Vermejo Park zone indicated increases of 0.08 MPa would be sufficient for triggering earthquakes (Nakai et al., 2017b). Poroelasticity has been found to favor slip for high-angle normal faults beneath the injection reservoir (Chang & Segall, 2015) and may amplify stresses inducing earthquakes in the Raton Basin.

The timing of pore fluid pressure changes is strongly dependent on hydraulic diffusivity (Barbour et al., 2017), which may explain the lack of a short-term (< years) temporal correlation between wastewater injection and seismicity (Figure 2.1a; Figure 2.S7). The summed injection rate was steady to slightly decreasing from 2016 to 2020 and no apparent correlation exists between the injection rate and earthquake rate (Figure 2.S7). The temporal evolution in the Raton Basin is similar to other areas where induced seismicity can lag several years behind the initiation of wastewater disposal (Schoenball et al., 2018). The rate of wastewater injection in the basin plateaued from ~2004 to 2014 with an average total of ~2.45 Mbbl/month (Figure 2.1b). Comparatively, the injection rate has declined 32% in the last five years (2016-2021) with an average total of ~1.67 Mbbl/month. The earthquake rate for the same time periods has decreased ~40% (from ~8.5 to 5 $M\geq3$ earthquakes/year when comparing 2004-2014 to 2016-2021, respectively) which suggests the wastewater injection and seismic record may be correlated when longer timescales (~5 to 10 years) are considered. Following a rate reduction in wastewater injection, Dempsey & Riffault, (2019) suggest induced seismicity will initially decline, experience occasional quiescence, and eventually reach a new equilibrium. The most recent decrease in the earthquake rate (~1.7 $M\geq3$ earthquakes/year from Jan 2020–Sept 2021, ANSS ComCat, 2021) may reflect an adjustment of the seismicity in response to the reduced wastewater injection rate.

2.6.2.2. Tercio and Vermejo Park zones

From 2008–2020, the wells with the highest injection rates and largest cumulative injection volume lie within the Tercio and Vermejo Park zones just south of the CO-NM border (Figure 2.10). These zones are the most seismically active during this study (Figure 2.11). Two additional wells (VPR 007 and VPR 042) are co-located between the large injectors. All four wells are within ~10 km horizontal distance and <250 m vertical distance of each other. They collectively inject >450,000 bbl/month on average from 2016 to 2020. Weingarten et al. (2015) found the likelihood that a wastewater injection well is associated with earthquakes increases as the maximum injection rate increases, e.g., high-rate wells (>300,000 bbl/month) are twice as likely to be associated with earthquakes as low-rate wells (<100,000 bbl/month). High-rate wells perturb pressure at larger magnitude and further extent than low-rate wells (Weingarten et al., 2015). The larger spatial effect of high-rate wells also increases the probability of encountering faults. Absolute earthquake locations extend from the area of large cumulative injection along the border to 15 km north in the Tercio zone and 20 km south in the Vermejo Park zone (Figure 2.11c). At the furthest extents in these zones, earthquakes are closer to other injection wells but are not spatially contiguous with these low-rate wells.

2.6.2.3. Northeastern basin

Seismicity is observed at the greatest distance from wells beyond the northeastern margin of the basin. Earthquakes occur up to ~27 km from the nearest injection well and ~35 km from the nearest moderate-rate well (Figure 2.11). Above basement injection, as is the case in the Raton Basin, has been linked to larger spatial footprints of seismicity in a global compilation (Goebel & Brodsky, 2018). Induced earthquakes have occurred 20-40 km from injection wells in Oklahoma (Keranen et al., 2014; Goebel et al., 2017) and ~25-90 km from high volume wells in Kansas (Peterie et al., 2018; Ansari et al., 2019). Assessing the origin of the more distant events in the Raton Basin is difficult because catalog sensitivity to M<3 earthquakes is sporadic over the past two decades. The earthquake catalog by Nakai et al. (2017) from 2008-2010, has 70 earthquakes per year in the north and 23 in the northeast above their M_c of 1.3 (see Figure 2.11a for definition of north and northeast). Using the same M_c, we find a comparable number of earthquakes in the north, 63 earthquakes/year, and sixty percent more earthquakes in the northeast, 37 earthquakes/year. Injection rates in the northern basin have not changed dramatically over time (Figure 2.10). After two decades of wastewater injection, it is plausible pore-pressure has diffused to the region of northeast seismicity, however, poroelastic effects could be more influential in triggering earthquakes at large distances from wells (Goebel et al., 2017) or on hydraulically isolated faults (Chang & Segall, 2015). Reanalysis of earlier seismic data and further hydrogeologic modeling (e.g., Nakai et al., 2017b) are needed to test potential linkages between the northeastern extent of earthquake activity and wastewater injection at distances >25 km.

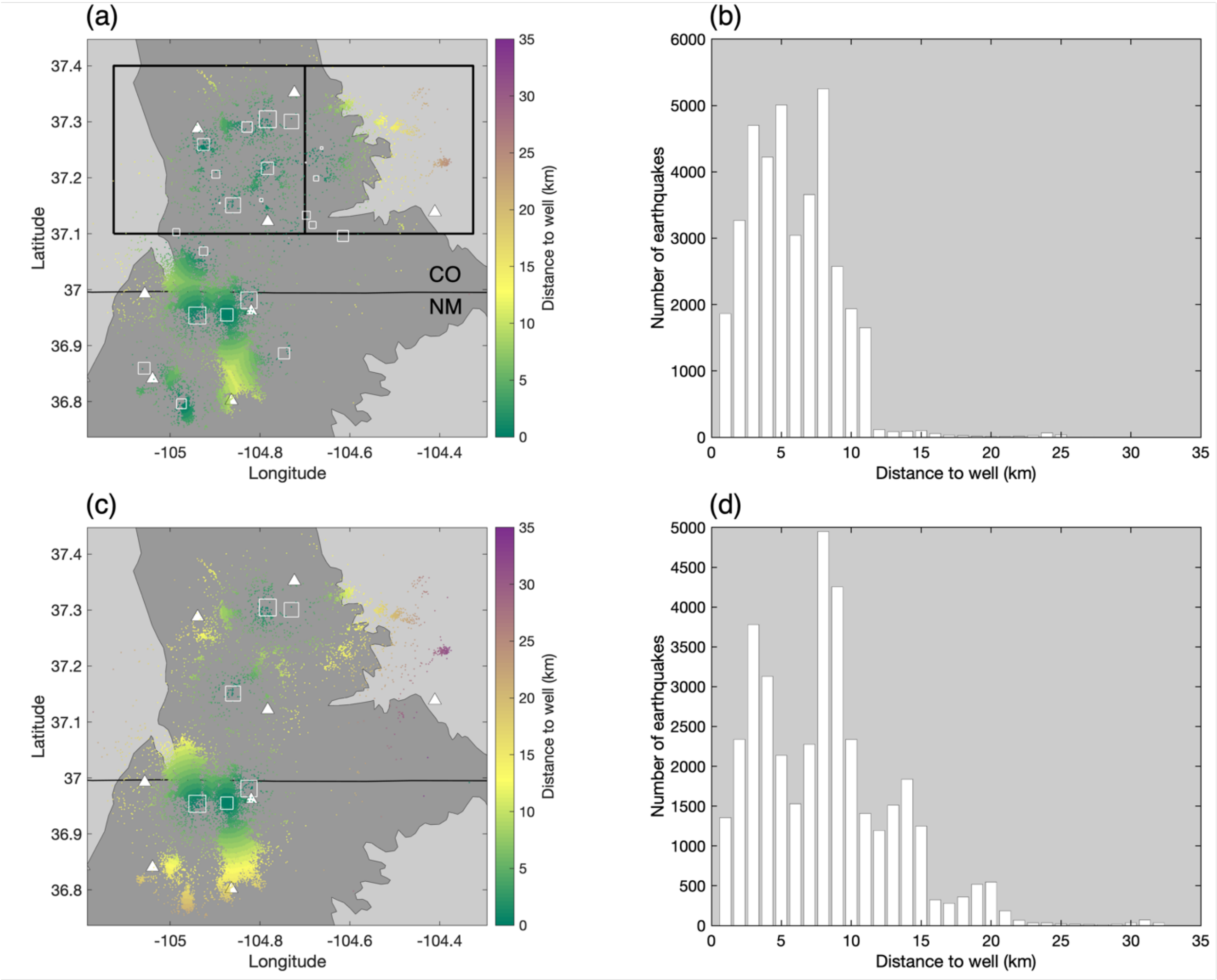

Figure 2.11 Earthquake distance to nearest wastewater injection well. Map of earthquake distance to (a) the nearest wastewater injection well and (c) the nearest moderate-rate (100,000-300,0000 bbl/month) injection well. Color corresponds to distance. The size of white squares scale with the average monthly injection volume from 2016 to 2020. White

triangles are seismometers. The perimeter of the black box in (a) distinguishes the north mentioned in 6.2.3 and the line dividing the box separates the northeast and the northwest. (b) Distribution of distances from (a). (d) Distribution of distances from (c).

2.6.2.4. Trinidad zone

Few earthquakes are observed in the Trinidad zone which hosted the largest recorded earthquake in the basin (M_W 5.3) in the second of two short-lived earthquake sequences in 2001 and 2011 (Figure 2.9, Meremonte et al. 2002; Rubinstein et al., 2014; Barnhart et al., 2014). Approximately seventy earthquakes with $M_L<2$ are located in the Trinidad zone during our study (Figure 2.9b) with none surviving the relocation step (Figure 42.b). Only one earthquake was located in the Trinidad zone for the 2008–2010 earthquake catalog with $M_c=1.3$ by Nakai et al. (2017b). The combination of results demonstrates seismicity in the Trinidad zone has included quick bursts of activity and quiescent periods on the order of years.

The monthly injection rate in the Trinidad zone for the years preceding the 2011 sequence was ~600,000 bbl/month (Figure 2.9c), ~70-80% of which was contributed by the two co-located high-rate wells nearest the M_W 5.3 earthquake (Figure 2.9a & c). In 2012 the injection rate dropped to ~300,000 bbl/month and by 2016 to ~100,000 bbl/month. The two co-located wells were completely shut-in by January 2015, ~20 months prior to our study (Figure 2.9c). Goebel et al. (2019) found fluid pressures can decrease within the injection reservoir at kilometer-length scales within days of well shut-in. We suggest that the 2011 earthquake sequence depleted the stored tectonic strain in the crust. Furthermore, the Trinidad zone experienced a significant decrease in wastewater injection after 2011, contributing to our observation of a low and declining seismicity rate from 2016 to 2020 (Figure 2.9). The Trinidad zone may be a useful example for further studying the evolution of seismicity following cessation of about a decade of injection during which moderate magnitude events occurred.

2.6.3. Statistical similarity to tectonic sequences

Induced and tectonic settings are expected to have different spatiotemporal-magnitude and frequency-magnitude statistics if the physical mechanisms driving the processes are different. For example, hydraulic fracturing and enhanced geothermal system regions (Mousavi et al., 2017), may have higher b-values than tectonic settings, whereas lower b-values are observed for water-injection-related sequences in the Sichuan Basin (Lei et al., 2019). However, the b-value for the Raton Basin is ~1, comparable to tectonic settings as well as some other wastewater injection induced seismicity cases in the United States (e.g., Cochran et al., 2020; Mousavi et al., 2017). The b-value of ~1 suggests that the stress condition that drives seismicity in the Raton Basin is similar to tectonic settings and dissimilar to other induced regions with abnormal b-values.

In cases of clear anthropogenic forcing, such as geothermal stimulation, independent background earthquakes dominate the spatiotemporal-magnitude behavior (Schoenball et al., 2015; Martinez-Garzon et al., 2018). In regions of tectonic earthquakes, fewer independent and more clustered earthquakes are observed compared to some induced settings (Zaliapin & Ben Zion, 2016b). The range of C_v (~1.6-2) for the full basin and subregions suggests low to moderate temporal clustering. Predictions from ETAS modeling demonstrate the earthquake rate for the full basin, Tercio zone, and Vermejo Park zone can be modeled by time-independent events and subsequent aftershocks. Lastly, the NND distributions (Figure 2.7, 2.8d) reveal a higher ratio of clustered to background seismicity in the space-time-magnitude domain for all considered regions.

The strong clustered behavior of the Raton Basin suggests earthquake-earthquake interactions are more significant than direct forcing by fluid injection, which produces more background events. A study by Schoenball et al. (2017b) with similar clustering results to ours led to the conclusion that earthquake sequences in Oklahoma and southern Kansas are initiated by anthropogenic stressing but stored tectonic energy drives sequences. Alternatively, a one-month study by Cochran et al. (2020) found independent sequences dominate Oklahoma seismicity and suggests they are directly driven by the high stressing rates of wastewater disposal wells. Wastewater injection rates in their study region were 7-8 Mbbl/month, ~4-5 times the wastewater injection rate during our study (Figure 2.1b). For the Raton Basin we suggest, similar to Schoenball et al., (2017b), that small changes in pore fluid pressure from moderate- to low-rate wastewater injection decreases the frictional resistance on faults, permitting the stored tectonic stress to initiate slip and continue through interevent triggering (earthquake-earthquake interactions).

2.7. Conclusions

A four-year earthquake catalog of ~38,000 earthquakes improves the resolution of the seismogenic structures in the Raton Basin and provides us the opportunity to characterize the earthquake behavior through spatiotemporal-magnitude statistical analyses. Sixty short, 1-3 km long, faults with a range of strikes from WNW to NNE are active in the basement beneath the Raton Basin. The majority of fault motion agrees with the regional scale normal faulting regime although some oblique and reverse slip exists. High permeable conduits, such as fault zones, likely extend upward from the basement into the basin sediments providing hydraulic connectivity between the injection reservoir and the seismically active faults.

The Tercio and Vermejo Park zones host over 80% of the basin's seismicity. The Trinidad zone that hosted the 2011 M_w 5.3 earthquake experienced low rates of seismicity from 2016 to 2020, likely due to the combined effects of near-complete release of tectonic strain and the large decrease in the wastewater injection rate from 2011 to 2016.

Unlike some regions of induced seismicity with distinct independent background events resulting from direct forcing by fluid injection, the spatiotemporal-magnitude behavior of the seismicity in the Raton Basin is more strongly clustered, similar to tectonic regions. We suggest that the low- to moderate-rate wastewater injection of the Raton Basin may only initiate earthquake sequences by decreasing the frictional resistance on faults whereas stored tectonic stress is responsible for subsequent earthquake-earthquake interactions.

2.8. Supplementary Information

Network	Station	Start	End	Sample Rate (Hz)	DOI
TA	T25A	2016-07-20	2019-03-07	100	https://doi.org/10.7914/SN/TA
C0	T25A	2019-03-07	2020-07-09	100	https://doi.org/10.7914/SN/C0
YX	UNM1, UNM2, UNM3, UNM4, UNM5, UNM6, UNM7	2016-07-20	2020-07-09	100	https://doi.org/10.7914/SN/YX_2016
4E	1-96	2018-05-12	2018-06-15	250	https://doi.org/10.7914/SN/4E_2018

TABLE 2.S1 Networks and stations used in this publication are listed, along with the dates of the data used, sampling rates, and digital object identifiers (DOI).

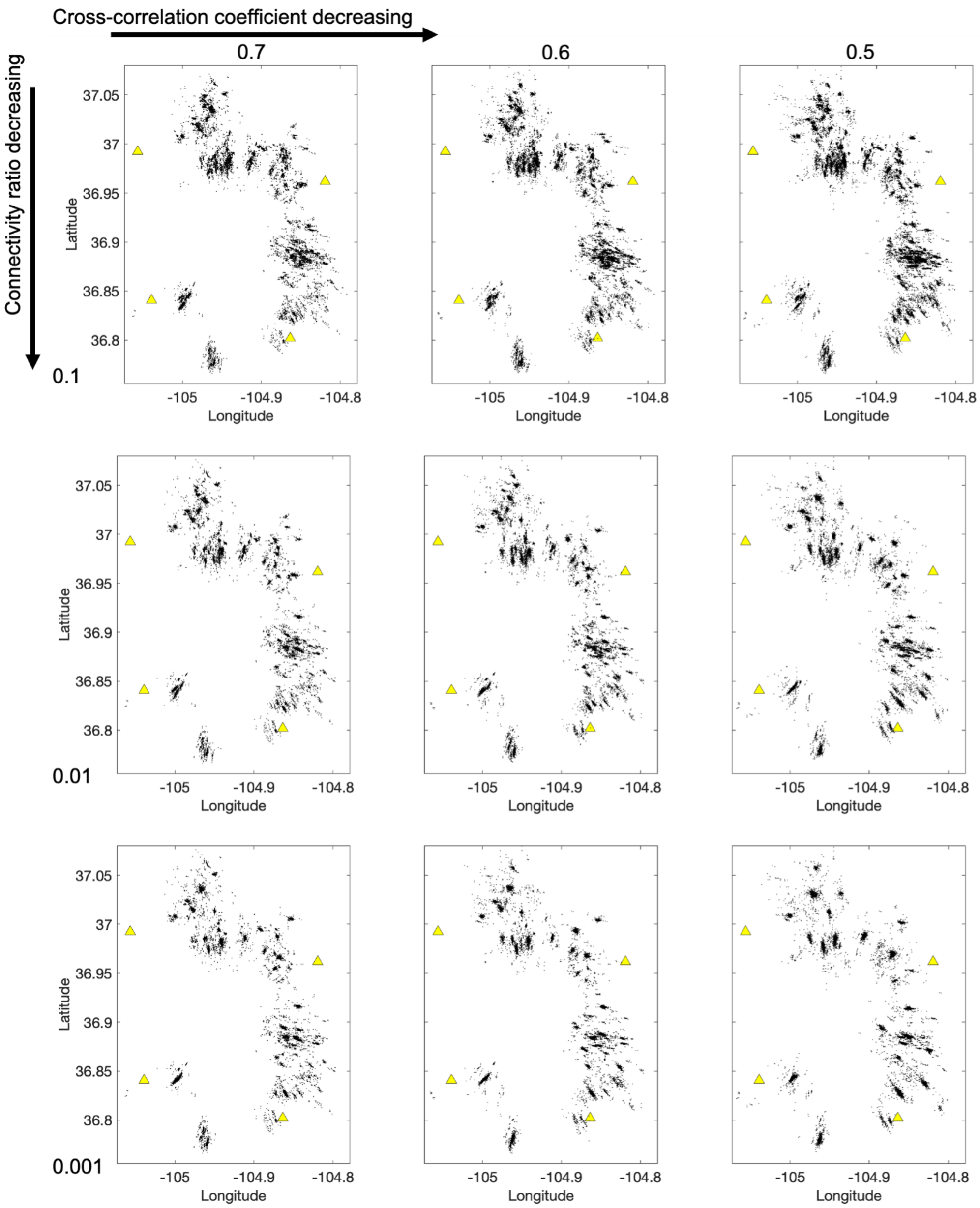

Figure 2.S1 Testing connectivity ratios and correlation parameters in GrowClust. Maps of the southern portion of the Raton Basin, black dots are earthquake hypocenters. Yellow triangles are seismometers. The columns correspond from left to right to the minimum cross-correlation coefficient considered for the computation of the GrowClust event-pair similarity coefficient. At least 5 differential time observations had to be above the minimum cross-correlation coefficient, which was set to 0.7 for the left column, 0.6 for the center column, and 0.5 for the right column. The rows are organized by decreasing connectivity ratio from top to bottom, with 0.1 for the top row, 0.01 for the middle row, and 0.001 for the bottom row. The high connectivity ratio (top row) resulted in more clusters with less events in each

cluster. In contrast, the low connectivity ratio (bottom row) resulted in fewer clusters with more events in each cluster. For more information on parameters please see Trugman & Shearer, (2017). The middle result (middle row, middle column) is shown in the publication.

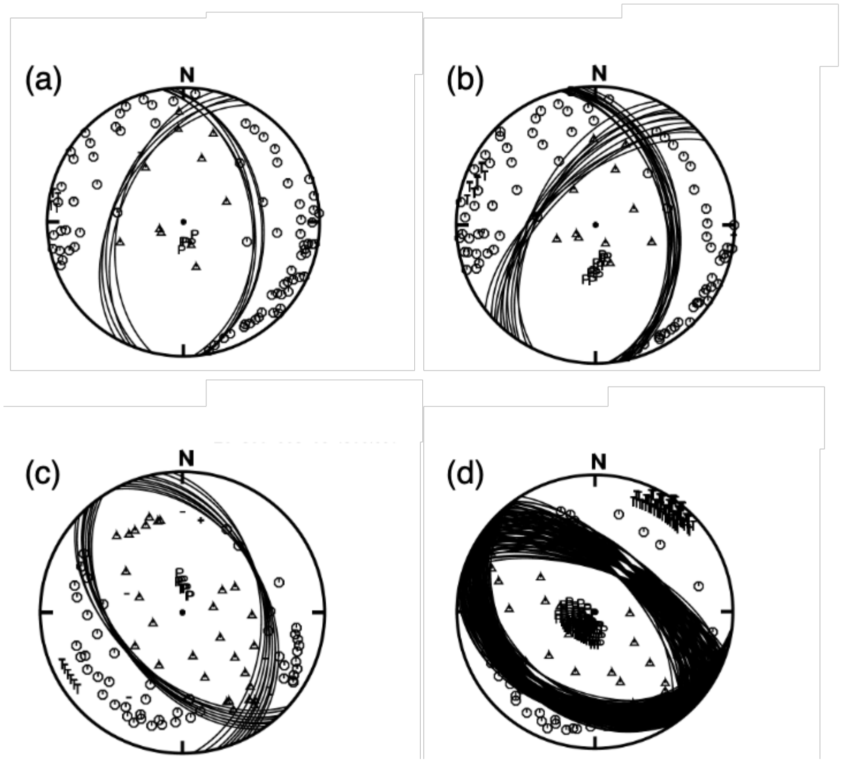

Figure 2.S2 First-motion focal mechanisms. Focal mechanism solutions for (A) M_L 2.33 earthquake with 92 picks, (B) M_L 1.44 earthquake with 92 picks, (C) M_L 1.28 earthquake with 88 picks, and (D) M_L 1.26 earthquake with 70 picks. These focal mechanisms are plotted in Figure 2.6 in order from west to east corresponding to A-D.

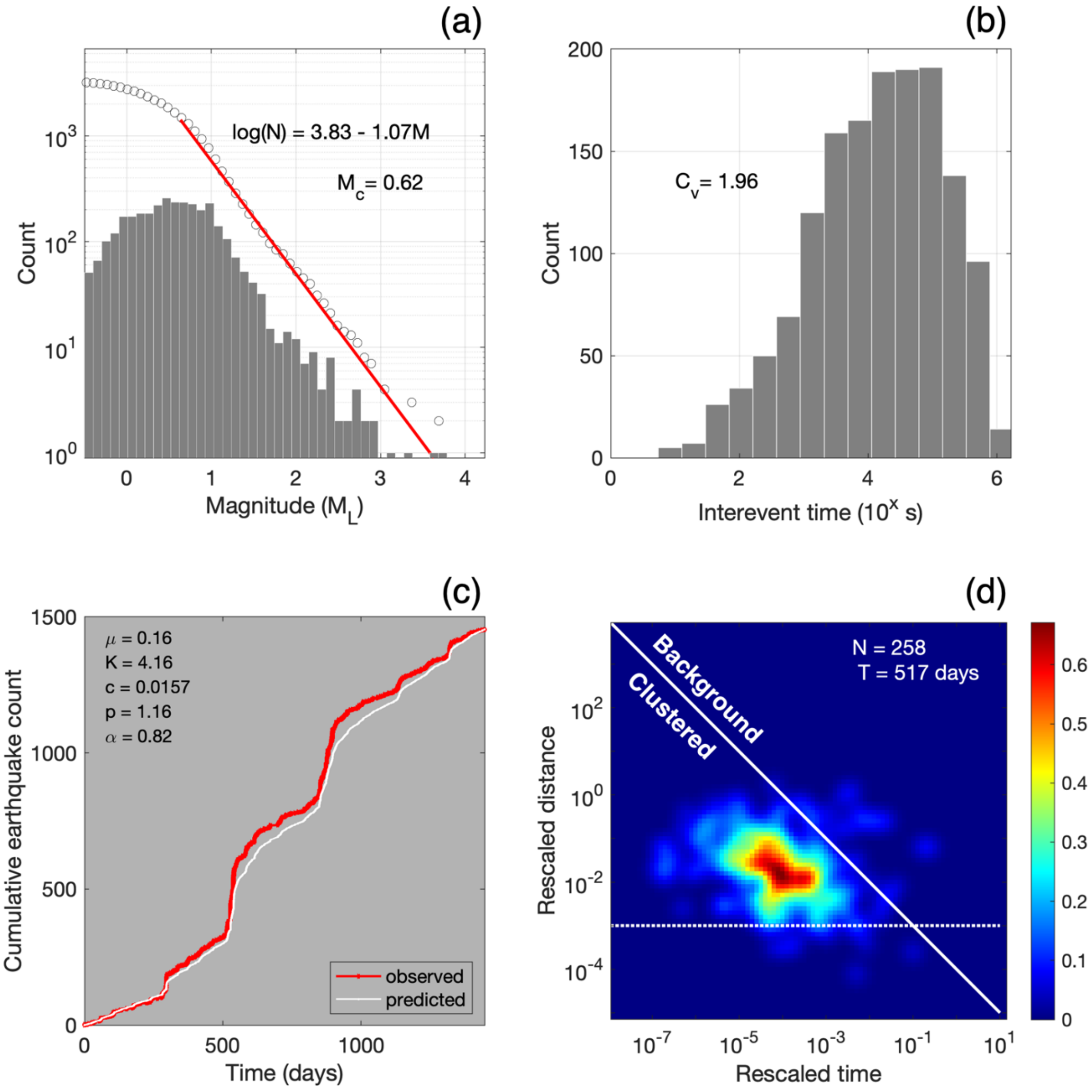

Figure 2.S3 Raton Basin frequency-magnitude and spatiotemporal statistical results for the northern basin (see S6 for map reference). (**a**) Earthquake frequency- magnitude histogram. The Gutenberg-Richter equation and the minimum magnitude of completeness (M_c) are printed. (**b**) Inter-event time histograms. The average coefficient of interevent time variation (C_v) is printed. (**c**) Cumulative number of earthquakes versus the number of days from observed seismicity (red) and Epidemic Type Aftershock-Sequence (ETAS) modeling (white line). ETAS maximum likelihood parameter estimates are printed (Ogata, 1988). (**d**) Nearest-neighbor rescaled time-distance distribution using relocated earthquake catalog. The color bar indicates the number of event pairs at a given rescaled distance-time. The diagonal

white line represents a stationary behavior. The horizontal white dotted line represents a clustered behavior. Lines can be used for comparison between Figures 2.S4-2.S6.

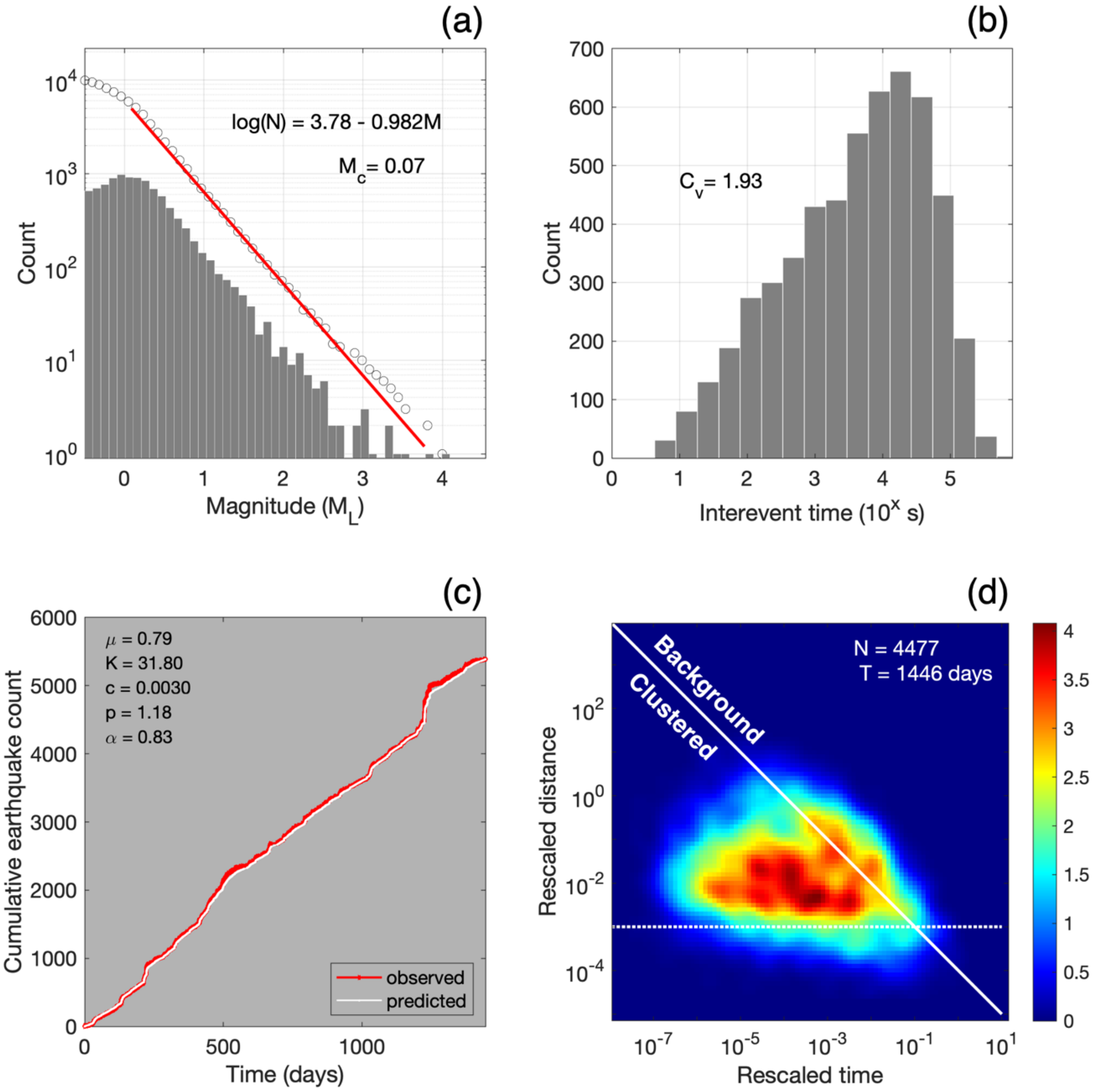

Figure 2.S4 Raton Basin frequency-magnitude and spatiotemporal statistical results for the Tercio zone (see 2.S6 for map reference). Description of (a-d) can be found in Figure 2.S3 caption.

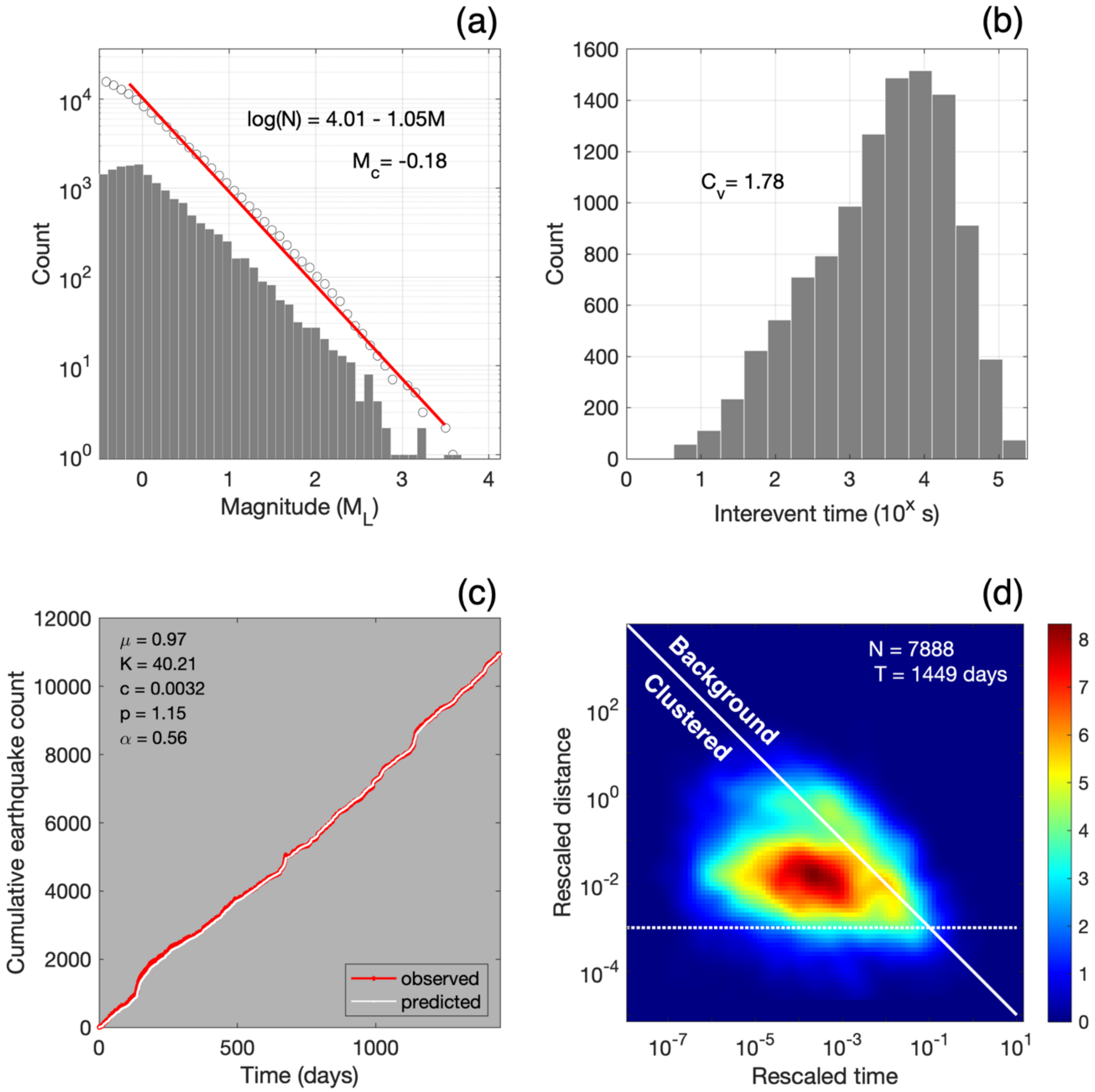

Figure 2.S5 Raton Basin frequency-magnitude and spatiotemporal statistical results for the Vermejo Park zone (see 2.S6 for map reference). Description of (a-d) can be found in Figure 2.S3 caption.

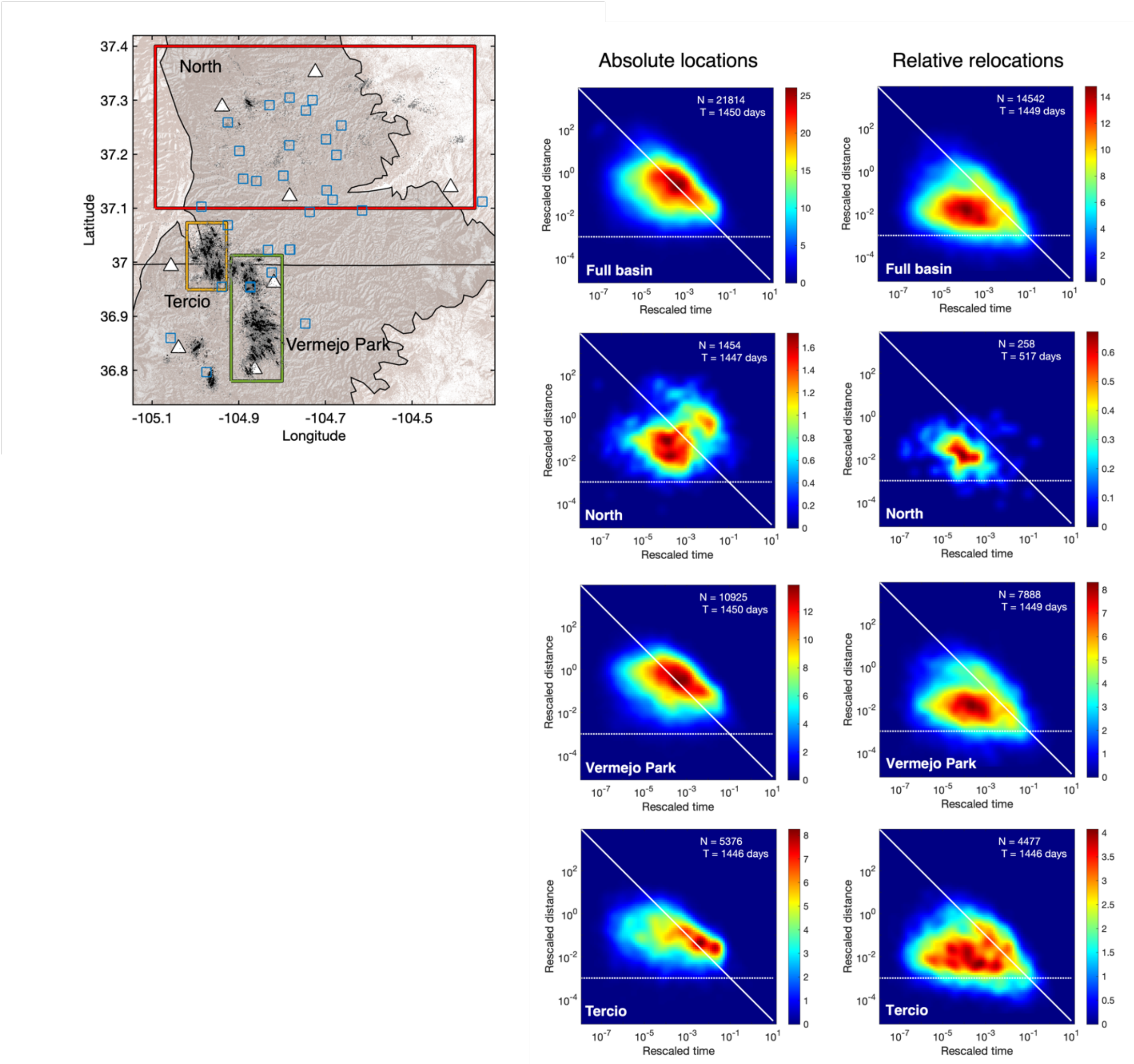

Figure 2.S6 Nearest-neighbor distributions (NND) for absolute locations and relative relocations. A map of the absolute (gray) and relocated (black) earthquakes. Boxes indicate the subregions considered for NND analysis and each region is labeled. White triangles are seismometers and blue squares are wastewater injection wells. NND results using absolute earthquake locations are on the left. Results using relative relocations of earthquakes are on the right. The considered region is written in white text in the bottom left corner of the NND plots. For “Full basin”, we consider the full study period shown in the map. The color bar indicates the number of event pairs. The diagonal white line represents a stationary behavior. The horizontal white dotted line represents a clustered behavior.

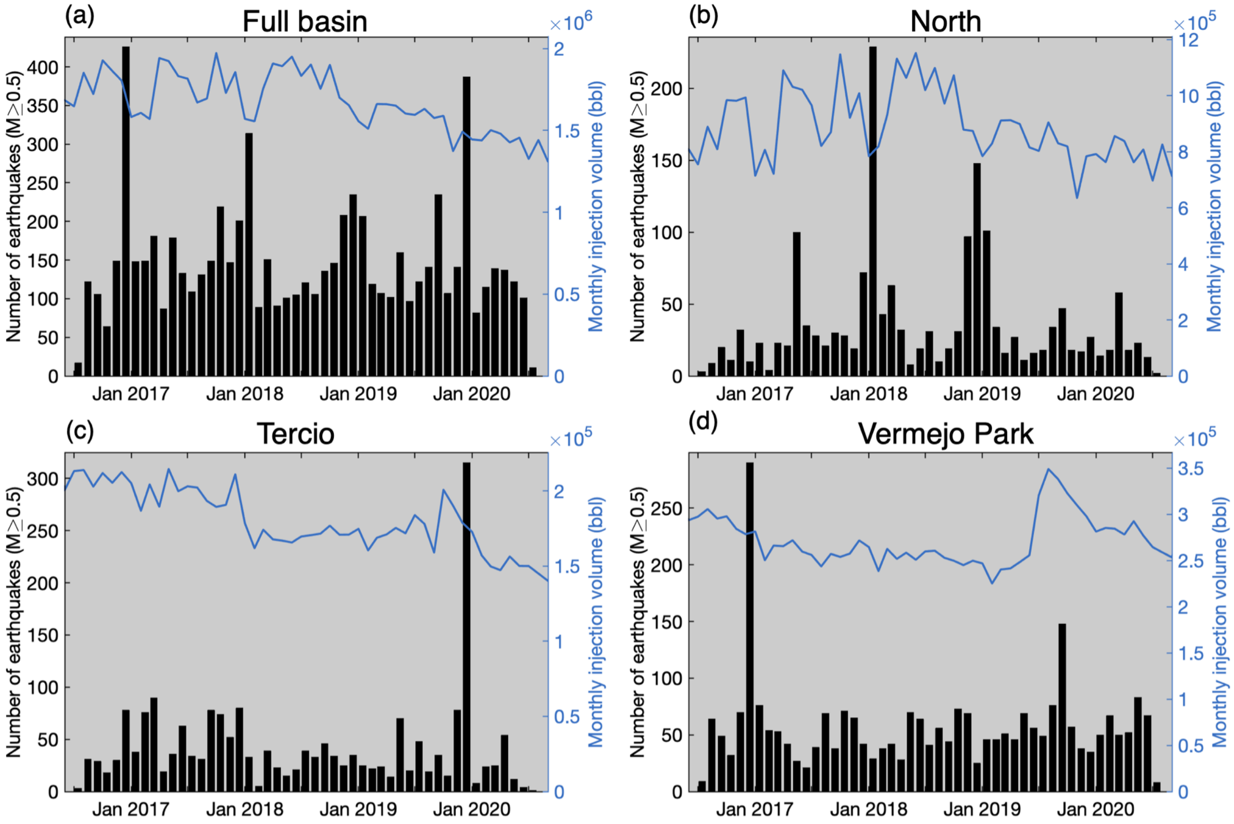

Figure 2.S7 Monthly number of $M_L \geq 0.5$ earthquakes (bars) and total monthly injection volume (blue line) within the (a) full basin, (b) Northern subregion, (c) Tercio zone, and (d) Vermejo Park zone. See S6 for a map of subregions.

3. Chapter Three: Cascading multi-segment rupture of a Mw 5.3 induced earthquake

Abstract

Complex rupture has been observed for large magnitude earthquakes but the scalability to moderate or small magnitude earthquakes is unknown. We investigated a moderate magnitude earthquake (Mw 5.3) in the Trinidad zone, located in the Raton Basin coalbed methane field on the Colorado-New Mexico border. The rupture scenario of the earthquake sequence and broader evolution of seismicity from 2008-2022 was captured using machine-learning for earthquake detection with an aftershock array followed by automated template detection. We found that the previously reported single-fault rupture of the 2011 Mw 5.3 mainshock was likely a cascading rupture with slip across multiple well-separated segments that we interpret as faults, asperities, or a combination of both. The mainshock rupture appears to have involved 3-6 distinct patches of slip based on aftershock clustering. The three southern clusters were active in the months to minutes prior to the mainshock, whereas the three northern clusters were inactive over the same period. Rupture initiated in the south and moved northward across the three southern clusters. The largest slip patch from a previous geodetic study aligns with the northernmost southern cluster. It is unclear if, or how many of, the three previously quiescent clusters in the northern Trinidad zone were involved in the mainshock rupture. However, all six segments hosted seismicity directly after (<60 minutes) the mainshock rupture. The 2011 earthquake sequence arrested near the 2001 MbLg 4.5 mainshock earthquake sequence. Seismicity in the Trinidad zone became increasingly quiescent from 2012-2016, and the earthquake rate from 2016-2020 is two orders of magnitude lower than that of the neighboring Tercio and Vermejo Park zones. A factor that may have contributed to this case of complex rupture was the 10 years of nearby wastewater injection weakening the fault zone. Multi-segment rupture presents a challenge for accurately assessing how large an earthquake can grow. Understanding cascading ruptures is especially important in fluid-injection settings where fault geometry is unresolved until reactivated and the strength of the crust can be locally modified by fluid-injection.

3.1. Introduction

3.1.1. Implications of complex fault structures on earthquake hazard

Accurate seismic hazard assessment relies on the ability to estimate the maximum magnitude of earthquakes. Calculating a maximum magnitude in complex tectonic settings is difficult because earthquake rupture can grow by stepping-over or physically linking multiple faults (Fossen & Rotevatn, 2015). Multi-asperity and multi-fault ruptures are observed for some large earthquakes with M>6.5 (e.g., Philibosian & Meltzner, 2020; Hamling et al., 2017; Ross et al., 2019; Wei et al., 2011; Chen et al., 2020; Yang et al., 2021) but are less commonly observed for moderate to small magnitude (M<6) earthquakes. This may be due to the techniques that are used to observe them, such as finite rupture inversions and back-projection rupture imaging, which are typically only feasible for M≥6 earthquakes. The use of these techniques produces increasing examples of cascading rupture, the temporal clustering of earthquakes on neighboring faults or asperities (e.g., Yang et al., 2021; Zhang et al., 2020; Yue et al., 2012; Ross et al., 2019; Yamanaka & Kikuchi, 2004; Ye et al., 2018). It is uncertain if smaller ruptures are similarly capable of linking multiple segments. High-frequency rupture inversions utilizing dense arrays and high-resolution spatiotemporal evolution of microseismicity will improve the potential discovery of cascading rupture during smaller magnitude events.

In a cascading process, the final size of an earthquake is controlled by the distribution of slipable patches and the surrounding stress conditions (Ide, 2019). Therefore, cascading rupture poses a serious seismic hazard in regions where faults are unmapped, buried, or potentially being reactivated by fluid injection. Thus far, the maximum magnitude estimates of earthquakes in fluid-injection settings have focused on probabilistic approaches and parameters related to the injection volume (Eaton & Igonin, 2018). However, these methods may be inadequate at predicting the size of cascading ruptures. For example, injection volume-based magnitude estimates were three orders of magnitude lower than the moment magnitude (Mw) 5.5 Pohang earthquake (Li et al., 2021) which ruptured two faults (Palgunadi et al., 2020). Understanding the frequency and physics of multi-segment earthquake rupture is important for hazard assessment, especially in fluid-injection settings where mitigation is possible.

3.1.2. The Trinidad zone

There are three major zones of seismicity in the Raton Basin, a coal-bed methane production field on the Colorado-New Mexico border (Figure 3.1). In the Trinidad zone, two earthquake sequences have occurred within 2 km of high-rate, high-volume wastewater injection wells: one in 2001 with a MbLg 4.5 mainshock and one in 2011 with a Mw 5.3 mainshock (Figure 3.1b; Rubinstein et al., 2014; Meremonte et al., 2002). Each sequence was preceded by foreshocks in the day(s) prior to the mainshock. A geodetic study (Barnhart et al., 2014) concluded the Mw 5.3 earthquake ruptured an 8-10 km-long, blind normal fault striking NE-SW. However, the rupture length is anomalously long for its magnitude and style. A typical rupture length for a Mw 5.3 is 5 km (Wells & Coppersmith, 1994). Unlike the Tercio and Vermejo Park zones, which have been persistently active, seismicity in the Trinidad zone is variable through time (Figure 3.1), experiencing very low rates despite the denser instrumentation from 2008-2010 (Nakai et al., 2017b) and 2016-2020 (Glasgow et al., 2021). We revisited the 2011 earthquake sequence to investigate the spatiotemporal evolution of fourteen years of seismicity in the Trinidad zone, with emphasis on the evolution of seismicity before and after the 2011 Mw 5.3 mainshock.

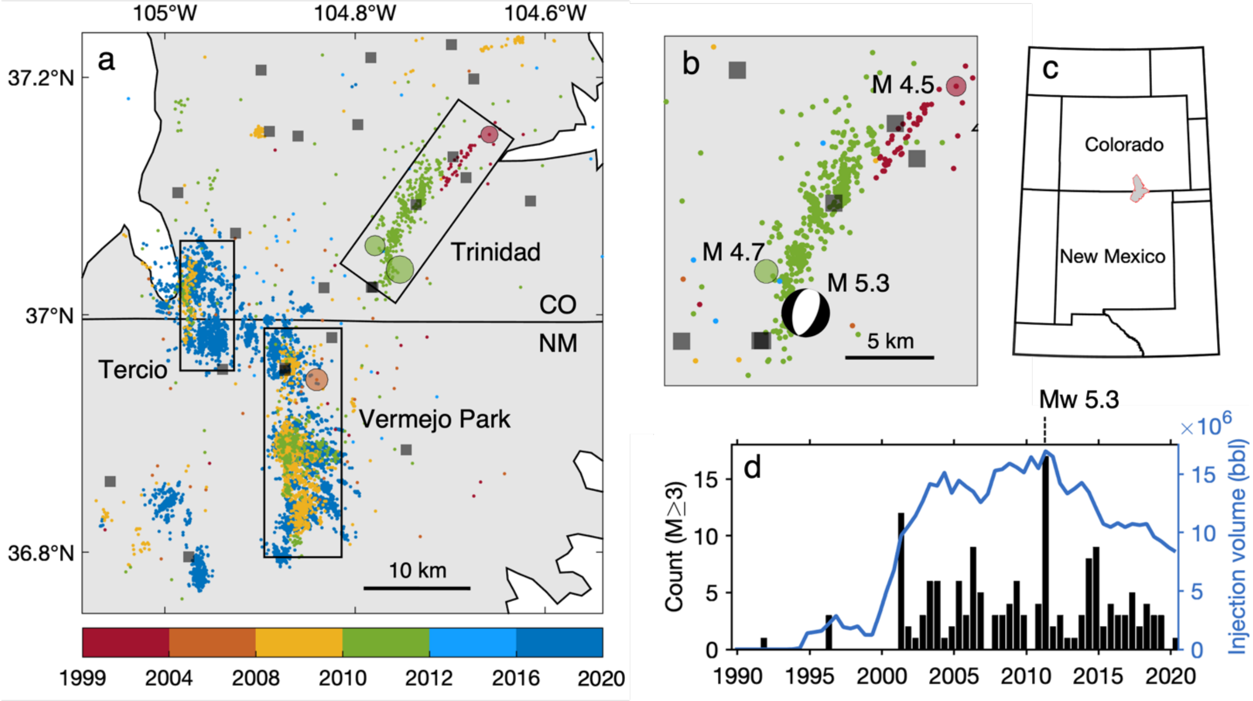

Figure 3.1. An overview of Raton Basin seismicity. a) Seismicity from multiple studies (Rubinstein et al., 2014; Barnhart et al., 2014; Nakai et al., 2017b; Glasgow et al., 2021) is

shown by dots and colored by the time ranges shown in the color bar. Note, only the relocated earthquakes from Glasgow et al., (2021) are shown. The five earthquakes with Mw or MbLg ≥ 4.5 are shown as larger circles scaled by their magnitude and colored by the time ranges. The three main zones of seismicity are marked by black rectangles and labeled. Wastewater injection wells are shown as gray squares. The Raton Basin is outlined in black and shaded gray. b) An overview of seismicity in the Trinidad zone. Figure descriptions from (a) apply to (b). The magnitude of earthquakes with Mw or MbLg ≥ 4.5 are labeled. The 2011 Mw 5.3 mainshock focal mechanism from Rubinstein et al., (2014) is plotted. c) Colorado and New Mexico state map. The Raton Basin is outlined in red and shaded gray. d) The number of earthquakes (M≥3) from the United States Geological Survey earthquake catalog (ANSS ComCat, 2022) in six-month bins are shown as black bars and correspond to the left vertical axis. The wastewater injection volume from Glasgow et al., (2021) for six-month intervals is shown as a blue line and corresponds to the right vertical axis. The six-month period containing the 2011 Mw 5.3 mainshock is denoted by a dashed line with a magnitude label.

3.2. Methods

3.2.1. Aftershock earthquake catalog

Automated workflows that combine multiple packages to build earthquake catalogs (e.g., Zhou et al., 2021; Zhang et al., 2022; Woollam et al., 2022) have been popularized by recent studies (e.g., Park et al., 2022). We applied an automated workflow, similar to Wang et al., (2020a) and Glasgow et al., (2021), to build an earthquake catalog using nine months of continuous data (August 2011-May 2012) from the six broadband seismometers nearest to the Trinidad zone (Figure 3.2a; Figure 3.S1). Four seismometers were part of a rapid aftershock experiment deployed within one day and 15 km of the 23 August 2011 Mw 5.3 mainshock. One seismometer is located ~20 km northwest of the Ration Basin and ~110 km from the study area (Figure 3.S1). The sixth seismometer, T25A, is a legacy U.S. transportable array station that has recorded continuously since 2008. It is located ~30 km from the Trinidad zone along the eastern edge of the Raton Basin (Figure 3.2a inset, Figure 3.S1). The unfiltered continuous seismic data from the six stations was passed to an automated phase-picker (PhaseNet; Zhu & Beroza, 2019) that outputted P and S phase probabilities. Phases with >0.3 probability were considered for association and location. At least three P- and two S-phases were required for association and initial location estimates using Rapid Earthquake Association and Location (Zhang et al., 2019). Locations were updated using VELEST (Kissling et al., 1995). The earthquakes were relocated using hierarchical clustering of waveform similarity (GrowClust; Trugman & Shearer, 2017). To be considered for relocation, an event needed an average cross correlation coefficient (CCC) ≥ 0.45 and a minimum of three phases with CCC ≥ 0.6. Local magnitudes (ML) were estimated for earthquakes using the Mw-calibrated equation from Glasgow et al., (2021).

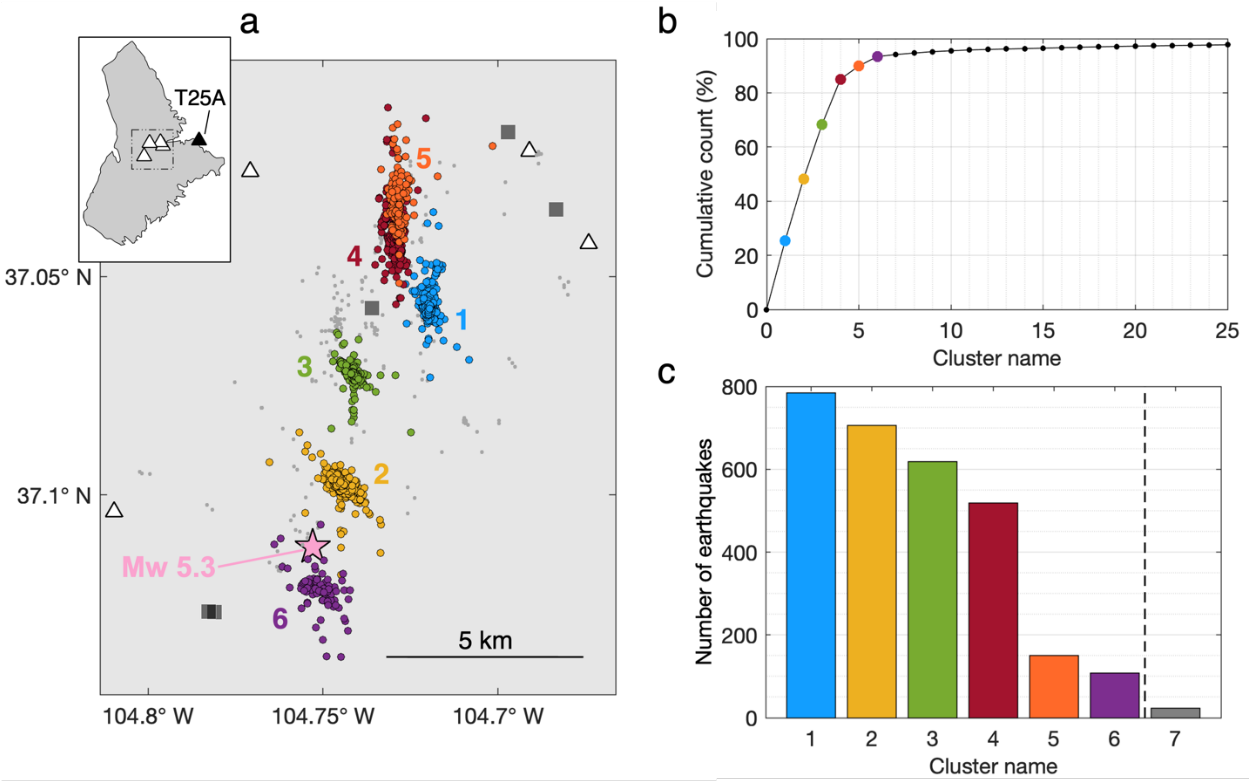

Figure 3.2. The aftershock catalog. a) Map of aftershock earthquakes. Earthquakes are shown as circles. The six main earthquake clusters are labeled 1 through 6 sequentially by the decreasing number of events per cluster (as shown in c). The earthquakes from small clusters (n<25) are shown as gray dots. The pink star marks the epicenter of the 2011 Mw 5.3 mainshock from Barnhart et al., (2014). Seismometers are displayed as triangles and wastewater injection wells as squares. Note, two wastewater injection wells are co-located in the southwest of the plot. The inset shows the Raton Basin outline and seismometer distribution with station T25A labeled. The black dashed box denotes the area shown in the

main figure. b) The percentage of earthquakes per cluster. The six main clusters compose 93% of earthquakes in the aftershock catalog. c) The number of relocated earthquakes per cluster. After cluster 6, the number of earthquakes per cluster drops to <25 earthquakes per cluster (e.g., cluster 7). This study focuses on the clusters left of the dashed line with >100 earthquakes. Cluster names and colors 1-6 correspond between plots a-c.

3.2.2. Template detection

Template detection at station T25A was used to characterize the spatiotemporal evolution of seismicity in the Trinidad zone during its 14 years of continuous recording (2008-2022) including seismicity surrounding the 2011 Mw 5.3 mainshock. T25A was the only station within 100 km that recorded the 2011 mainshock. Templates were created from the three significant sources with documented seismicity in the Trinidad zone since 2008 (Figure 3.1): the aftershock catalog from this study, the USGS catalog, and the 2016-2020 catalog by Glasgow et al., (2021). The Nakai et al., (2017b) catalog was not used because it documented one earthquake within the Trinidad zone. Earthquakes in the USGS catalog from May 2008 - August 2011 were used to build templates within ~15 km of the Trinidad zone. When available, origin times and locations were updated to those from Barnhart et al., (2014). In total, seven templates were from the USGS catalog, and we manually picked their P- and S-wave arrivals at T25A.

The remaining templates were built from earthquakes within the Trinidad zone that occurred after the 2011 mainshock. All earthquakes from the aftershock catalog built in this study and from the catalog in Glasgow et al., (2021) with ML≥1 were used as templates. Templates were made for earthquakes with ML<1 if they had a signal to noise ratio ≥3. Following this step, an additional constraint is added for the aftershock catalog to minimize the number of redundant detections that would result from the inclusion of similar template waveforms and to save computational expense. For the aftershock catalog, a candidate template was rejected if it had a CCC ≥ 0.6 with the already accepted templates. In total, 117 templates were selected from the aftershock catalog and 57 from the Glasgow et al., (2021) catalog. Ninety-one templates were from the six largest clusters identified in the aftershock catalog which compose 93% of the total relocated seismicity.

To increase the stability of single-station template detection, we used six time-windows for each template: a P-window and an S-window for each of the station's three-components. The inclusion of P- and S-windows, rather than a single window for the event, ensured the relative P- and S-times were consistent with the template. Whenever necessary, P- and S-arrival times at T25A were estimated using P- and S-wave travel time curves. A 3-second P-window and a 7-second S-window were used for each template. Windows began 1 s prior to the phase arrival. The minimum S minus P time was 3.25 s, therefore, the P and S windows never overlapped. We did not vary the window length based on the template location because the source-receiver distances are similar (30-35 km). The data was down sampled to the lowest sampling rate of the recording period, 40 Hz, and filtered from 1-10 Hz (Gao & Kao, 2020). Template detection using the Fast Matched Filter Method (Beauce et al., 2018) was performed from 2008-2022, the full recording period of T25A. For each template, we obtained a fourteen-year long time series of the mean CCC.

To determine the threshold at which a given template would trigger on noise, we ran template detection with time-reversed templates similar to the method of Slinkard et al., (2014). The maximum CCCs for the time-reversed templates ranged from 0.28-0.34. This test suggested that (time-forward) templates began to trigger on noise when CCC were ≤ 0.34 (Figure 3.S2). If our goal was to detect every event, including lower quality earthquakes buried in noise, then the detection threshold could be set at CCC >0.34. However, our goal was to detect moderate to high quality events that were similar (e.g., location and mechanism) to the template, therefore we set the detection threshold slightly higher at CCC ≥ 0.45. Visual inspection of new detections confirmed the higher quality of the 0.45 threshold compared to 0.34 (Figure 3.S3). New earthquakes were assigned the location of the template. When multiple detections existed within a 10-second window, only the origin time and the location of the template event corresponding to the highest CCC was kept.

3.3. Results

3.3.1. Aftershock earthquake locations

The aftershock earthquake catalog includes 4,417 earthquakes over nine months and the minimum magnitude of completeness is -0.6 (Figure 3.S4). Absolute earthquake locations are comparable to previous estimates that suggest a slightly NNE-SSW strike of aftershocks following the 2011 Mw 5.3 mainshock (Figure 3.1 & 3.2; Figure 3.S5; Rubinstein et al., 2014; Barnhart et al., 2014). Seventy percent of earthquakes were relocated (3,088 of 4,417). After relocation, earthquakes clustered into six main groups (n>100) that compose ~93% of the seismicity (Figure 3.2). The remaining earthquakes clustered into smaller groups (n<25). Earthquake clusters are labeled 1-6 in descending order of the total number of events in each cluster. The three southern clusters (clusters 2, 3, and 6) are located ~1-3 km apart, whereas the three northern clusters (clusters 1, 4, and 5) are <1 km apart. Clusters 4 and 5 overlap in map view but can be differentiated by their depths with averages of ~6.4 ± 0.5 km and 4.2 ± 0.7 km respectively. Depth is relative to the surface elevation, ~2.1 km in the Trinidad zone. We recognize the southern cluster orientations may partially be attributed to unreliable location estimates at the fringe of the seismic array. Nevertheless, the distinct clustering of events based on waveform similarity remains valid and their locations reveal the fault zone structure (e.g., Savage et al., 2017). The new earthquake locations suggest the Trinidad zone is defined by multiple seismogenic segments rather than previous suggestions of a single through-going fault for the 2011 earthquake sequence (Barnhart et al., 2014; Rubinstein et al., 2014).

3.3.2. Spatiotemporal evolution of seismicity from template detection

The template detection catalog contains 4,865 new earthquakes with 88% (4,277) detected using the aftershock catalog templates, 8.5% (412) detected using the USGS catalog templates, and 3.5% (176) detected using the Glasgow et al., (2021) catalog templates. The template detection catalog reveals the spatiotemporal evolution of seismicity in the 32 months prior to the 2011 M 5.3 earthquake. Seismicity in the southern Trinidad zone was intermittently active in the 32 months prior to the 2011 Mw 5.3 mainshock, whereas northern cluster 4 was moderately active and northern clusters 1 and 5 were inactive (≤ 5 earthquakes; Figure 3.S6). Two of the three foreshocks in the days prior to the mainshock can be associated with the two southernmost clusters based on their waveform similarity (CCC≥ 0.6) with templates from those clusters (Figure 3.3). In the weeks prior to the Mw 5.3 mainshock, earthquakes only occurred in the southern section with the majority of activity bounding either side of the mainshock epicenter (Figure 3.3). Within an hour of the mainshock rupture, all six clusters hosted earthquakes. Seismic activity significantly decreased for the Trinidad zone by ~2016, ~4.5 years after the Mw 5.3 mainshock whereas seismicity continued in the two other seismically active zones of the Raton Basin (Figure 3.4, Glasgow et al., 2021).

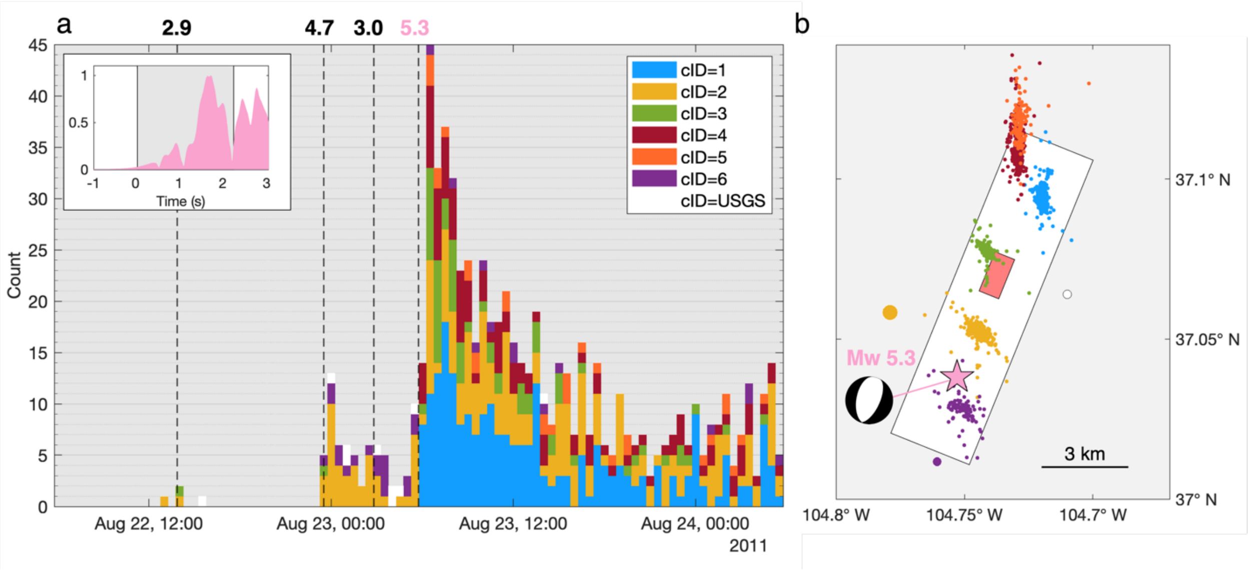

Figure 3.3. Mw 5.3 mainshock timeline. a) The earthquake record from template detection results in 30-minute bins for two days before and after the 2011 Mw 5.3 mainshock. Colors correspond to earthquake cluster IDs (see legend). The time of the foreshocks and mainshocks are marked by black dashed lines and their corresponding magnitudes are printed (ANSS ComCat, 2022). The inset displays the envelope function of the 0.5-3 Hz filtered vertical component waveform at station T25A for the mainshock. The 2.2 s mainshock duration (ANSS ComCat, 2022) is shaded gray. b) A map of seismicity in the Trinidad zone to accompany (a). The aftershock earthquake locations from Figure 3.2a are dots. The three foreshocks from (a) are scaled by magnitude. The pink star marks the location of the 2011 Mw 5.3 mainshock from Barnhart et al., (2014) and a pink line connects it to its focal mechanism from Rubinstein et al., (2014). The white rectangle is the surface projection of the mainshock rupture area with >5 cm of slip and the red rectangle denotes the maximum slip patch (~18 cm) from Barnhart et al., (2014).

3.4. Discussion

3.4.1. A complex rupture scenario

Direct inversion for finite rupture propagation in the 2011 Mw 5.3 mainshock is not feasible because only two seismometers were operating within ~100 km (Figure 3.S1), but our new aftershock and 14-year template-based earthquake catalogs illuminate the geometry of the fault zone and spatiotemporal evolution of its seismicity. In regions with an insufficient number of seismometers to invert for rupture dimensions, aftershocks have long been used to estimate the mainshock rupture area (e.g., Richter, 1955). The aftershocks that followed the Mw 5.3 mainshock occurred within its proposed rupture area from a geodetic slip inversion (Figure 3.3b; Barnhart et al., 2014). The distinct clusters of aftershock seismicity likely denote slip asperities, multiple faults, or a combination of both.

Nearfield observations of the mainshock were limited but two seismometers recorded the direct arrivals and revealed multi-peaked envelopes during the ~2.2 s rupture duration estimated by moment tensor inversion (Figure 3.3a inset; Figure 3.S7; ANSS ComCat, 2022). Similar to source-time functions for cascading failures in larger earthquakes (e.g., Yue et al., 2012; Wei et al., 2011; Ross et al., 2019), the multi-peaked envelopes likely indicate multiple pulses of energy being released as a series of segments ruptured. This contrasts with a single-peaked envelope which would be expected for a continuous planar fault rupture. Rupture initiated in the south, moved northeastward, and released the maximum slip at or near cluster 3 (Figure 3.3b; Barnhart et al., 2014) which appears consistent with the gradual onset of the envelope and maximum peak in energy toward the end of the rupture. Although some of the rupture specifics are not resolvable with the limited station coverage, we were able to determine some of the spatiotemporal evolution. The southern clusters of seismicity located near the mainshock hypocenter were active prior to the mainshock (Figure 3.3). Based on waveform similarity and the southern clusters response to foreshocks (Figure 3.3a), the three foreshocks likely occurred within or near the southern clusters. The northern clusters were seismically quiescent prior to the mainshock which either ruptured these previously inactive segments or triggered their activation shortly (<60 minutes) after rupture (Figure 3.3). The rupture terminated near the southwestern terminus of the 2001 MbLg 4.5 earthquake sequence (Figure 3.1b; Meremonte et al., 2002; Rubinstein et al., 2014). Cascading megathrust ruptures exhibit similar behavior at larger spatial and temporal scales, wherein multiple ruptures fill in a fault zone over time with little or no overlap and each rupture may heighten hazard in neighboring areas (Elliot et al., 2022; Philibosian & Meltzner, 2020).

The entire aftershock sequence spans ~11 km and strikes NNE which is generally consistent with the ~10 km and NNE strike from geodetic estimates (Figure 3.3b; Barnhart et al., 2014). The ~10 km length is anomalously long for a Mw 5.3 earthquake. Theoretical and empirical relationships estimate a Mw 5.3 earthquake corresponds to a 5-5.5 km rupture length (Wells & Coppersmith, 1994; Haiyun & Xiaxin, 2003). The geodetic inversion by Barnhart et al., (2014) included interferograms that span months on either side of the mainshock and therefore, included the net slip of the foreshocks, mainshock, and a few months of the aftershock activity in their ~8-10 km rupture length. Our aftershock and template-based earthquake catalog provides resolution of both the spatial and temporal evolution of seismicity during the same time. One plausible solution to remedy the fault length with the earthquake magnitude is if only the 3 southernmost clusters ruptured during the mainshock. In this scenario, the summed length of the three southern clusters, ~5 km, is consistent with empirical scaling of rupture length for a Mw 5.3 earthquake (Wells & Coppersmith, 1994). To test the feasibility of this scenario, we modeled the Coulomb stress change for two faults that have the strike and length of the two southernmost clusters of aftershocks. After rupture on the southernmost fault, the Coulomb stress change indicates that the receiver fault crosses the boundary between negative and positive Coulomb stress (-0.05 to 0.05 MPa; Figure 3.S8 b-c). This suggests triggering on the receiver fault was possible but with our geometry the receiver fault does not fall within the highest Coulomb stress change area. We also modeled the Coulomb stress change for a rupture with the proposed dimensions from Barnhart et al., (2014) to see if the aftershock locations fall within the zone of maximum positive Coulomb stress change. We found the aftershocks fall within the minimum coulomb stress change area that has >-0.5 MPa coulomb stress change (Figure 3.S8a).

The 2011 Mw 5.3 mainshock appears to have been a cascading rupture which included slip on multiple asperities along one or more faults. The ability or mechanism of earthquakes to rupture multiple faults or fault patches is poorly understood. A few cases of two-fault rupture have emerged for moderate magnitude earthquakes in fluid-injection settings (Palgunadi et al., 2020; Wang et al., 2020b; Guo et al., 2022). A multi-fault rupture scenario for the 2011 Mw 5.3 mainshock is possible and the ~2 km steps are feasible (Finzi & Langer, 2012; Wesnousky, 2006). Multi-fault and multi-asperity ruptures are typically observed for M>6.5 earthquakes (Philibosian & Meltzner, 2020). We suggest the ability of the 2011 Mw 5.3 earthquake to rupture multiple segments was advanced by fluid-injection operations, as it may have decreased the fault and step-over material strength ultimately increasing the connectability of faults or asperities during rupture (Finzi & Langer, 2012). It is unclear how large an earthquake could grow during cascading rupture, especially in injection-induced earthquake settings where blind and complex fault systems often go unrealized until seismically reactivated. Hazard assessment frameworks that allow single ruptures to have slip on multiple faults (e.g., Milner et al., 2022) or patches may lead to a more accurate view of risk.

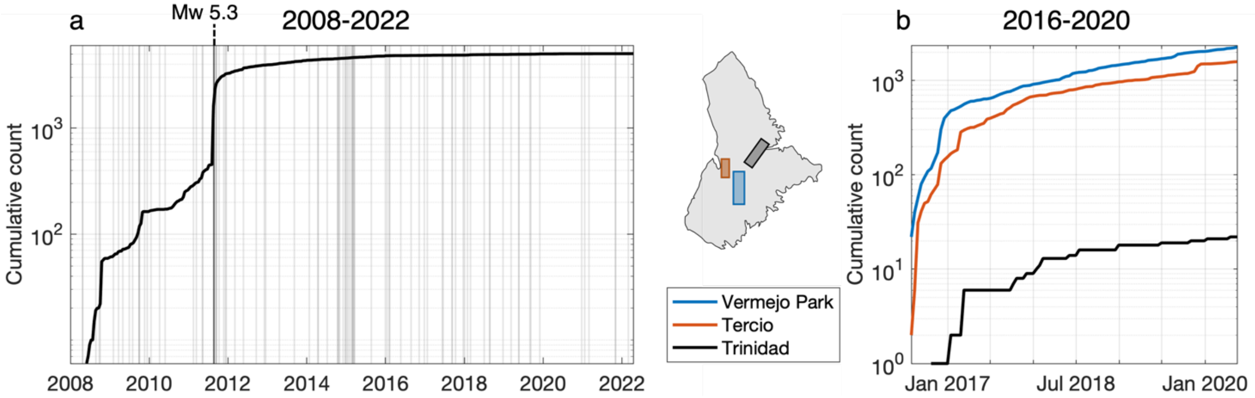

Figure 3.4. Spatiotemporal evolution of the Raton Basin seismicity. a) The cumulative distribution of earthquakes in the Trinidad zone resulting from 14 years of template detection is shown with a logarithmic vertical axis. Earthquakes with M≥3 (ANSS ComCat, 2022) that occurred within the Raton Basin are marked by a gray line and the 2011 Mw 5.3 earthquake is labeled. The right outset map displays the Raton Basin outline and denotes the three zones of seismicity. The color of the three zones of seismicity corresponds to the legend and line colors in (a-b). b) The cumulative number of earthquakes per zone above the minimum magnitude of completeness (Mc = 0.6) from 2016-2020 (Glasgow et al., 2021). The vertical axis is logarithmic.

3.4.2. Cessation of seismicity in the Trinidad zone

Very low rates of seismicity occurred in the Trinidad zone from 2016 to mid 2022 (Figure 3.4a). Seismic monitoring of the Raton Basin has been sporadic in space and time, however detailed multi-month to multi-year snapshots (e.g., Nakai et al., 2017b; Rubinstein et al., 2014; Glasgow et al., 2021) suggest the Tercio and Vermejo Park zones have been consistently seismically active since at least 2008 (Figure 3.1a). From 2016-2020, the Trinidad zone experienced two orders of magnitude less earthquakes than the Tercio and Vermejo Park zones (Figure 3.4b). This may be due to both the slow accumulation of stress following the 2011 earthquake sequence and the significant decrease (−80%) in the nearby fluid injection volume from 2012-2016 (Glasgow et al., 2021). The Vermejo Park zone has remained seismically active despite hosting the second largest earthquake in the Raton Basin, a Mw 5 earthquake in 2005 (ANSS ComCat, 2022; Figure 3.1a; Figure 3.4b). The lack of seismicity in the Trinidad zone which hosted the largest earthquake in the basin since the onset of wastewater injection may indicate decreased hazard for this zone.

3.5. Conclusions

Our study of the 2011 earthquake sequence and broader seismicity in the Trinidad zone supports a cascading rupture style for the Mw 5.3 mainshock and the cessation of seismicity beginning in 2016. The 2011 Mw 5.3 earthquake rupture initiated in the southern Trinidad zone and grew by slipping 3-6 well-separated segments which ultimately increased the final event magnitude. The rupture terminated at the edge of the 2001 earthquake sequence. It is unclear how common multi-segment ruptures are for moderate magnitude earthquakes but with our adopted machine-learning and automated methodology, it was possible to determine the rupture scenario even with sparse station coverage. This highlights the ability of rapid aftershock deployments to increase the scientific understanding of complex ruptures. This finding has important implications on earthquake hazards in induced settings and suggests estimates of the maximum magnitude of earthquakes that rely on the assumption of a single fault rupture are inadequate in some cases.

3.6. Supplementary Information

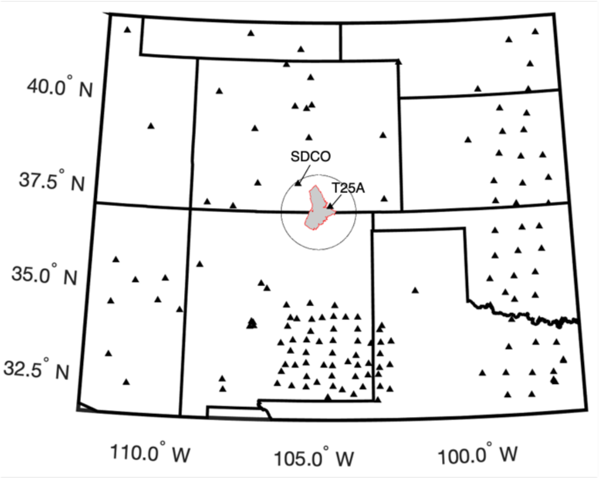

Figure 3.S1. Regional seismometer distribution. Seismometers within ~900 km of the Raton Basin that recorded on August 23, 2011 - the date of the Mw 5.3 Trinidad zone mainshock. Seismometers are black triangles. The basin is outlined in red and shaded gray. The black circle has a 110-km radius around the basin's center. The stations used in this study, SDCO and T25A, are labeled.

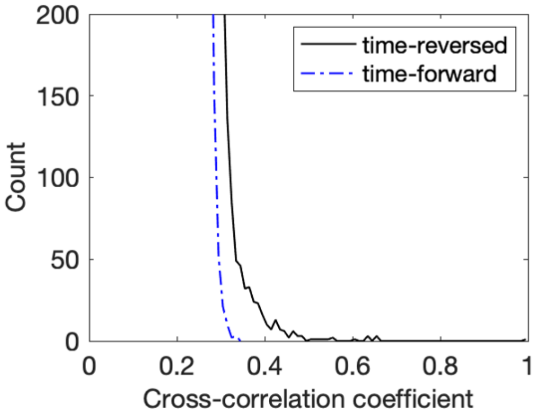

Figure 3.S2. Template detection cross-correlation coefficient distribution. An example of the number of detections versus the cross-correlation coefficient for a time-reversed (blue dashed line) and time-forward (black line) template. The time-reversed template has no detections above the 0.34 cross-correlation coefficient.

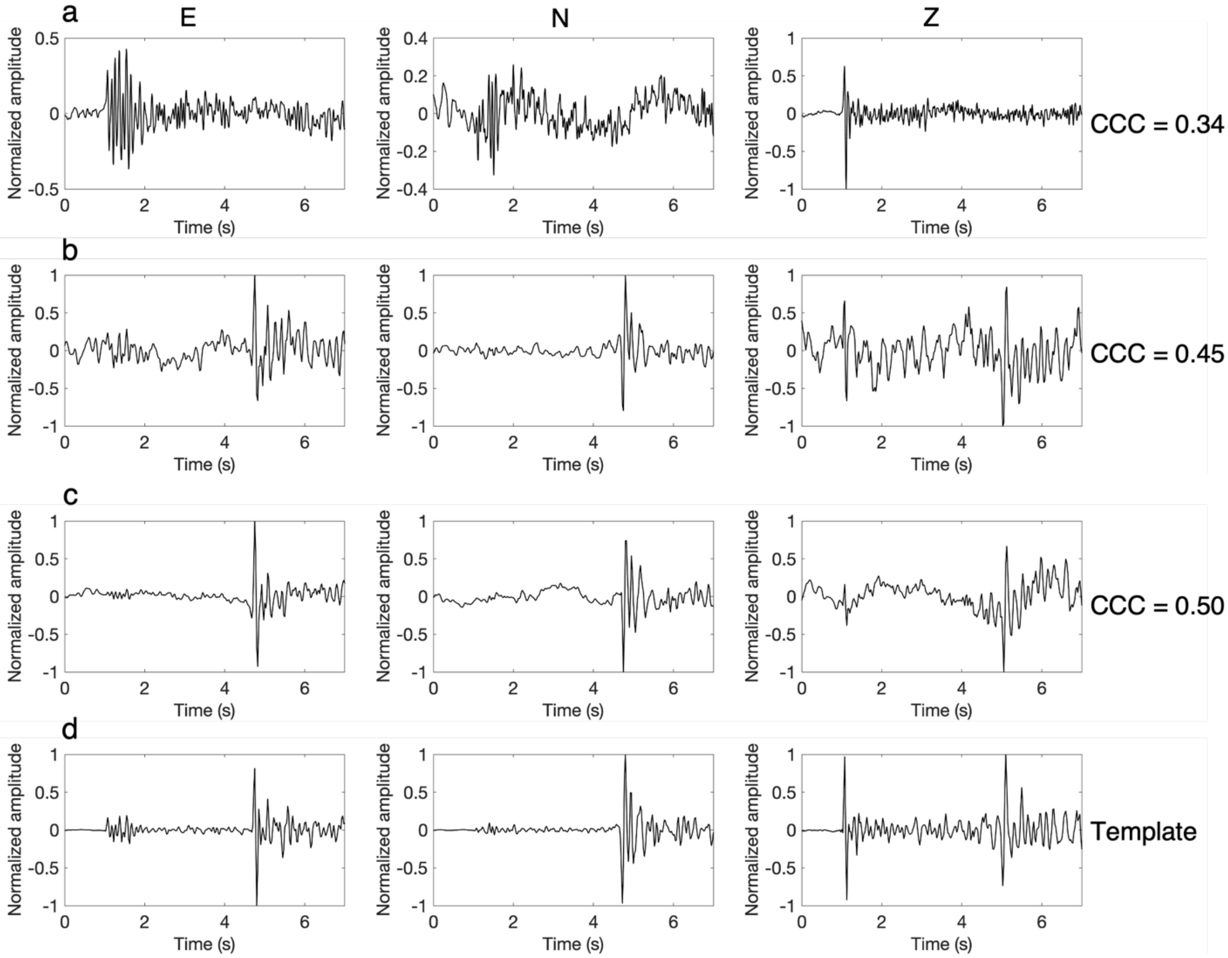

Figure 3.S3. Template detection examples. a-c) Three-component waveforms with different cross-correlation coefficients (CCC) printed on the right side. a) an example of the CCC where the templates will begin to trigger on noise (see Figure 3.S2). b-c) Examples of new earthquakes using our CCC threshold of ≥ 0.45. d) The template waveform. (a-c) are aligned based on the max CCC lag time.

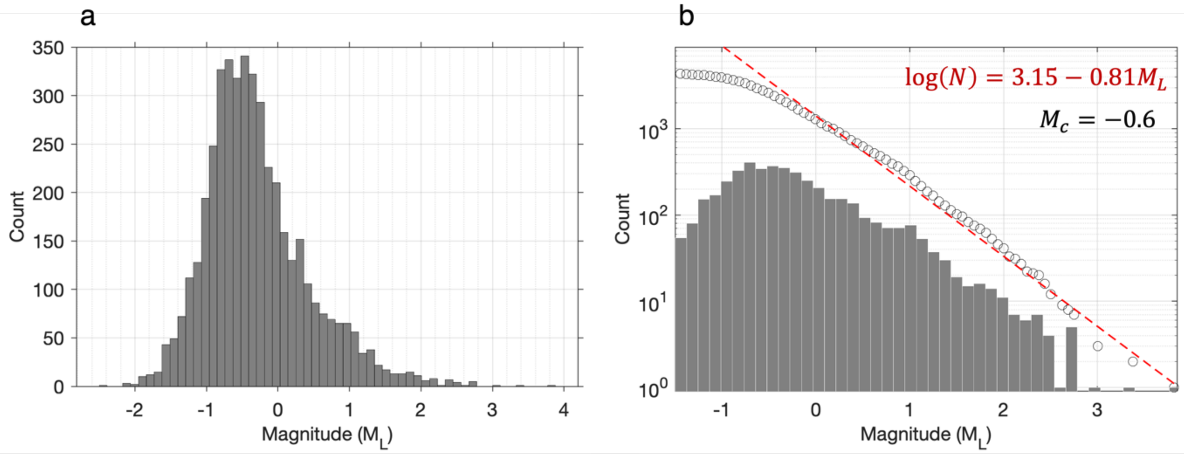

Figure 3.S4. Aftershock earthquake catalog magnitude distribution. The magnitude distribution in a) linear and b) log scale. b) The circles mark the cumulative distribution. The red dashed line fits the cumulative distribution down to the magnitude of completeness and its equation is printed in red. The minimum magnitude of completeness is -0.6. The frequency-magnitude number, also known as b-value, is 0.81.

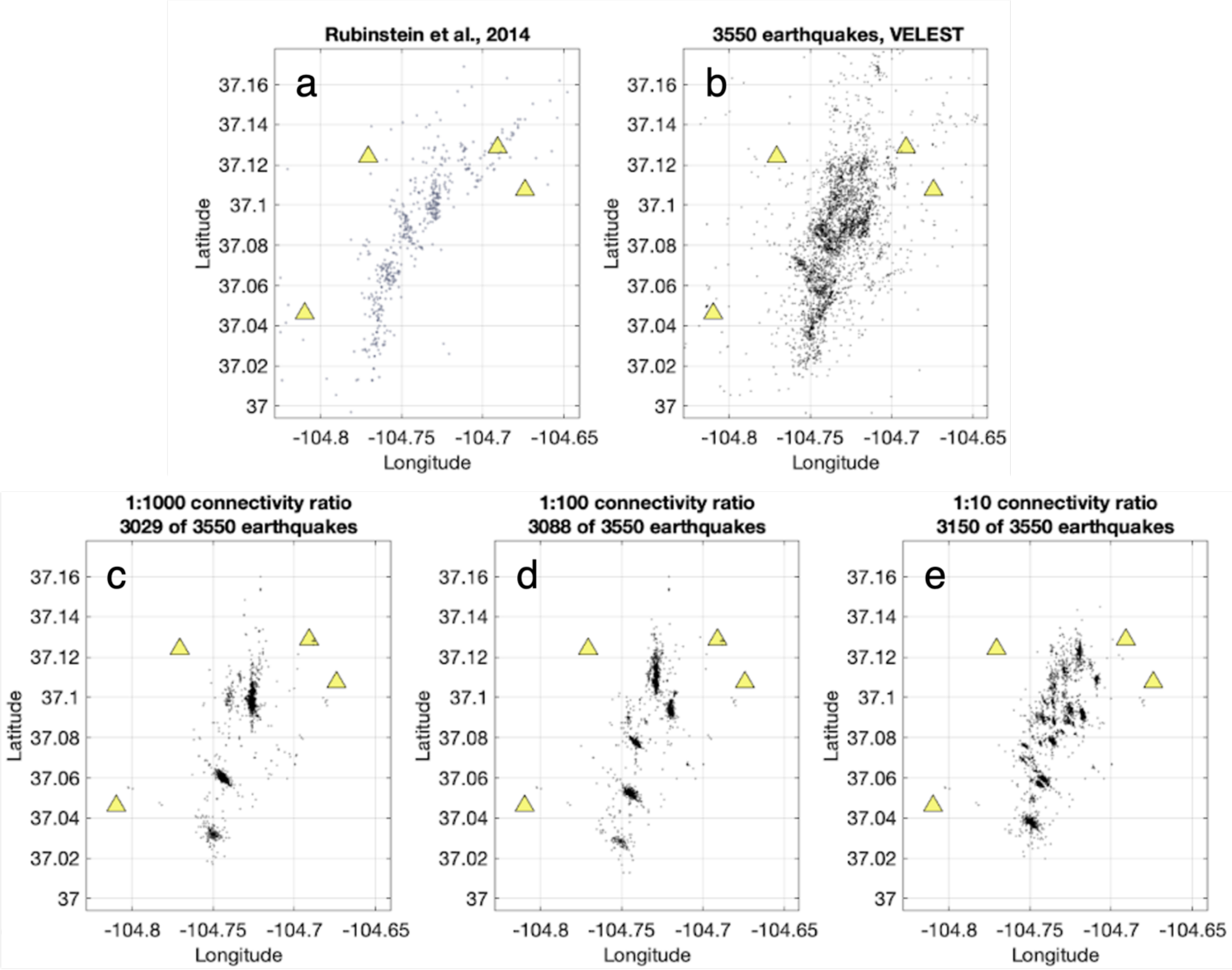

Figure 3.S5. Trinidad zone aftershock earthquake locations. a) Aftershock earthquake locations from Rubinstein et al. (2014). b) Aftershock earthquake locations following the VELEST step in our study. c-e) Examples of results from GrowClust when the connectivity ratio is modulated (see titles). The results from (d) are the final locations discussed in the manuscript text and figures.

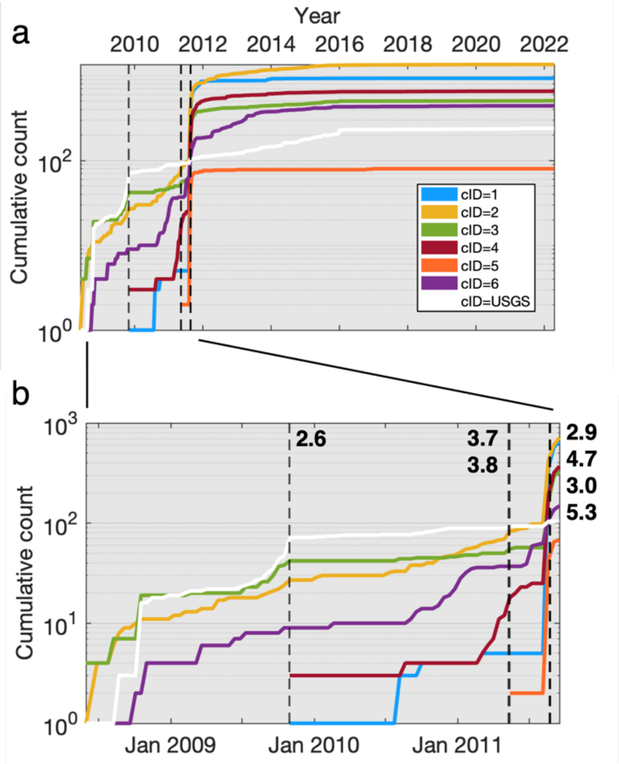

Figure 3.S6. Temporal evolution of earthquakes in the Trinidad Zone. Each line shows the cumulative number of earthquakes for a given group (see legend) from a) 2008 to 2022 and b) 2008 to the 2011 Mw 5.3 mainshock. The time of USGS detected earthquakes used as templates in this study are marked by black dashed lines and their magnitudes are labeled in (b). Earthquakes that occur close in time appear as one dashed line and their magnitudes are printed as a list.

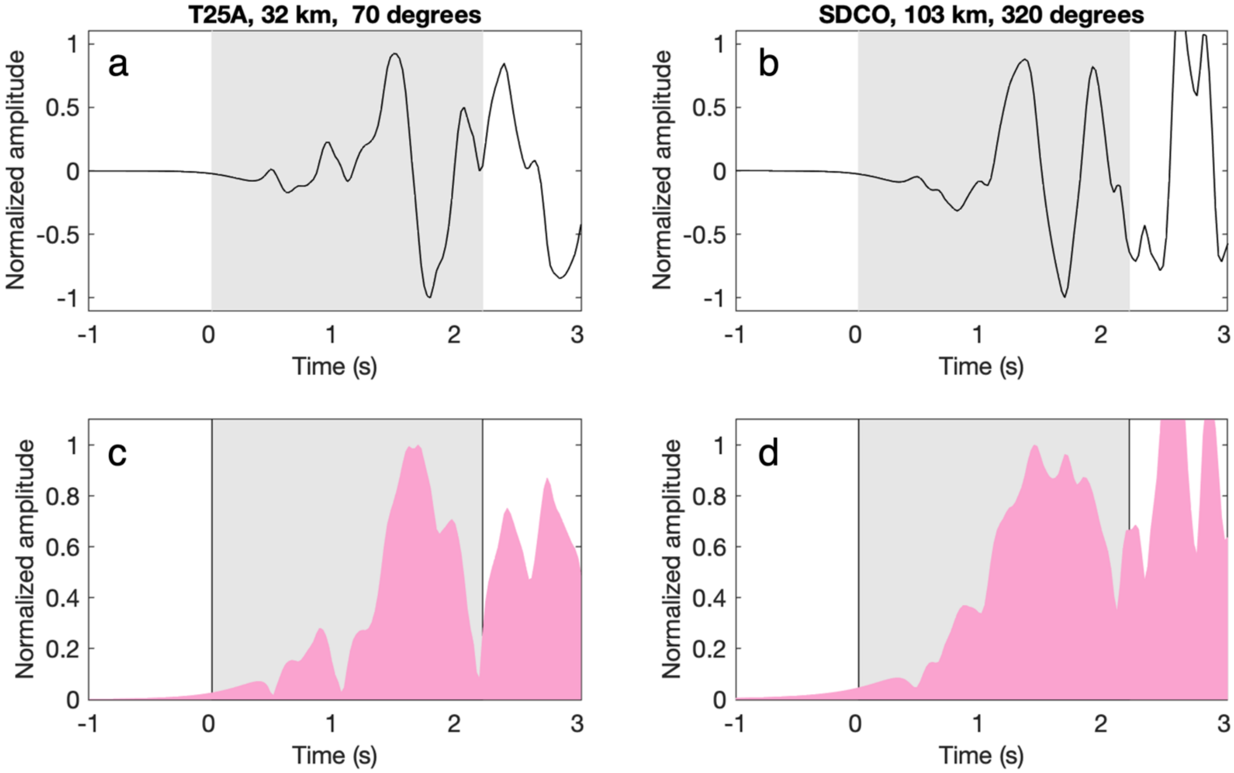

Figure 3.S7. Waveforms during Mw 5.3 earthquake rupture. a-b) Vertical component seismograms filtered from 0.5 to 3 Hz and c-d) envelopes from stations T25A and SDCO (Figure 3.S1). The station names and back azimuths to the Mw 5.3 earthquake are printed above the corresponding columns. Black lines mark the ~2 s recording of rupture (ANSS ComCat, 2022).

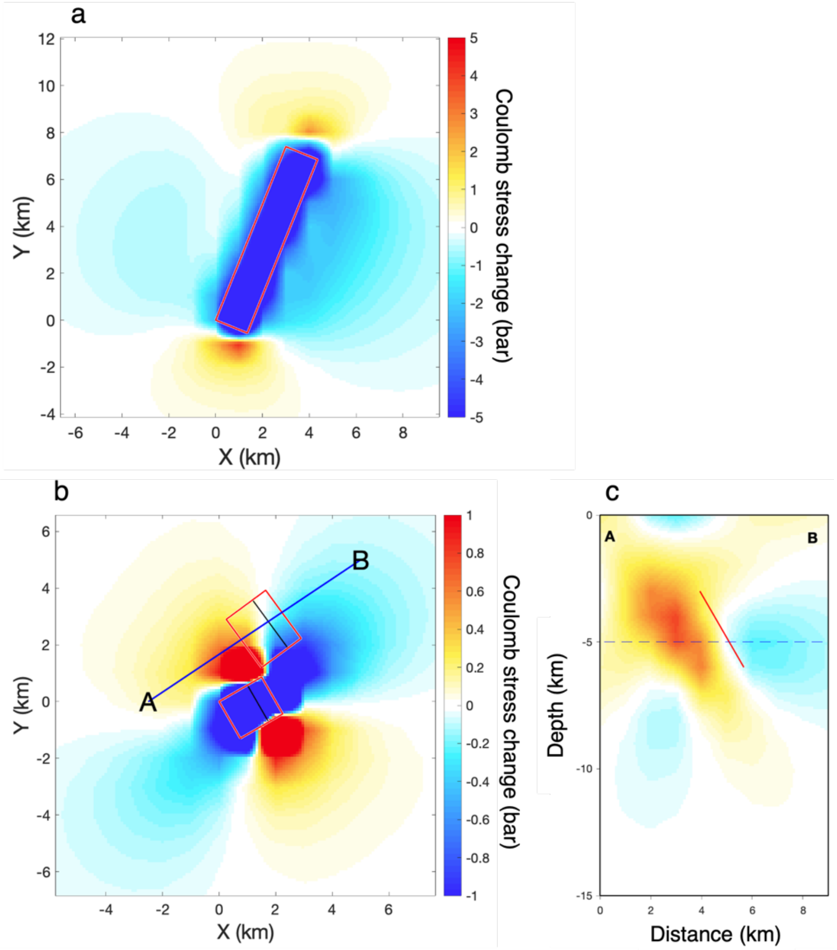

Figure 3.S8. Modeling coulomb stress. Coulomb stress change estimates at 5 km depth for a) Mw 5.3 earthquake on an 8-km long NE striking and east dipping normal fault from Barnhart et al., (2014) and b) a Mw 4.6 (1/6th of the moment of a Mw 5.3) earthquake on a 1.5-km long NNE striking and east dipping normal fault as the source and a similar dimension fault ~2 km to the northeast as the receiver fault. This fault geometry approximates the length and strike of the two southernmost aftershock clusters. c) Displays a cross-section from A-B shown in b. The red boxes in a-b display the surface projection of the fault plane and the black lines show where the fault intersects the plane of the current depth slice, in this case 5 km. For reference, 1 bar = 0.1 MPa.

4. Chapter Four: Global variability of the 410-km discontinuity form receiver function analysis of dense arrays

Abstract

Seismic boundaries between olivine polymorphs in Earth's mantle provide thermal and compositional markers that inform mantle dynamics and structure. Seismic studies of the mantle transition zone often utilize either global averaging with sparse arrays or regional sampling from dense arrays. The intermediate approach of this study targeted dense sampling from many dense seismic arrays around the globe. We consistently computed teleseismic P-to-S receiver functions and inverted for 1-D mantle transition zone seismic structure beneath each array to facilitate comparison of dense array results. In total, 67 arrays were used with an average of 3,600 receiver functions at each. We focused on the 410-km discontinuity (410) parameters of Vs jump and depth because the 410 is a prominent seismic interface and clearly linked to a single mineral phase transition between olivine and wadsleyite. Temperature and composition were inferred using modern mineral physics constraints and the new observational seismic estimates of the Vs jump and depth. The 410 depth ranges from ~405-440 km which is consistent with a ~300 K temperature range. The 410 Vs contrast ranges from ~3-9% which is consistent with a 24-80 vol. % olivine composition. The average olivine abundance of 45-50 vol. % is lower than the pyrolite model of the upper mantle, ~56 vol. % olivine for the dry case. The 24-80 vol. % range in olivine content suggests the upper mantle is compositionally heterogeneous near 410 km depth, where there are not major impediments to convection.

4.1. Introduction

Mantle transition zone boundaries are important markers of composition and temperature in the Earth's interior. Several discontinuities exist from 400-750 km depth, among the most seismically visible are those at approximately 410 and 660 km depth, followed by a weaker discontinuity at approximately 520 km depth. The 410-km discontinuity (410) is relatively simple as a globally observed seismic contrast. It is clearly linked to a binary phase transition between olivine and wadsleyite (Katsura & Ito, 1989; Ita & Sixtrude, 1992) and its positive Clapeyron slope is considered flow enhancing (Ringwood, 1991). Other boundaries, e.g., the 660- and 520-km discontinuities, are more complicated markers of temperature and composition. The 660-km seismic discontinuity (660) involves multiple phase transitions, and their relative observability varies with temperature and composition (Hirose, 2002; Jenkins et al., 2016; Simmons & Gurrola, 2000). Additionally, the 660 is an endothermic phase transition located near an increase in viscosity with depth, which can transiently impede convection and promote layered structure (Tackley, 1996). The 520-km discontinuity (520) is thought to represent a binary phase transition between olivine polymorphs, similar to the 410, but it may split into two discontinuities under some conditions (Saikia et al., 2008; Deuss and Woodhouse, 2001). Additionally, the subtler seismic contrast at the 520 leads to its scarcer observation compared to the 410 and 660 (Lawrence and Shearer, 2006; Zhang, 2022). In this study we seek to leverage the relative simplicity and broad observability of the 410 to estimate the variability of temperature and bulk composition at a well-mixed depth in the mantle convection system (e.g., Ballmer et al., 2015).

Most studies of the mantle transition zone either focus on small regions of dense sampling (e.g., van Stiphout et al., 2019; Hooft et al., 2003; Wu et al., 2022; Reusch et al., 2011; Jenkins et al., 2016) or global mapping (e.g., Huang et al., 2019; Houser et al., 2008; Chambers et al., 2005). However, the growth of continental seismic arrays in recent years provides some intermediate examples (e.g., Cao and Levander, 2010; Gao and Liu, 2014; Liu et al., 2015, Knapmeyer-Endrun et al., 2013). Global average properties are well known and frequently compared to model estimates of average mantle composition and the geotherm (Shearer & Flannigan, 1999; Cammarano et al., 2003; Zhou et al., 2022). The magnitude of depth variations and inferred temperature variations between studies has received much scrutiny. Dense array observations may lead to better constraints on mantle properties compared to global averaging with long period precursors because they involve a shorter path between the sampled discontinuity and receiver, are less affected by spurious site or path effects because of averaging, and can lead to shorter period observations. Although many dense array teleseismic receiver function studies exist around the globe, the datasets are incompatible because of the variability in processing and inversion methods. The goal of this study was to implement a less common observational perspective which allows for comparison between arrays by assembling and uniformly processing teleseismic receiver functions from globally distributed dense arrays. We uniformly processed teleseismic P-to-S receiver functions and inverted for the properties of transition zone interfaces using a collection of dense broadband arrays from around the globe. The 410, 520, and 660 were modeled but we focused on the 410 results and determined the spatial variability of composition and temperature in this well-mixed portion of the upper mantle.

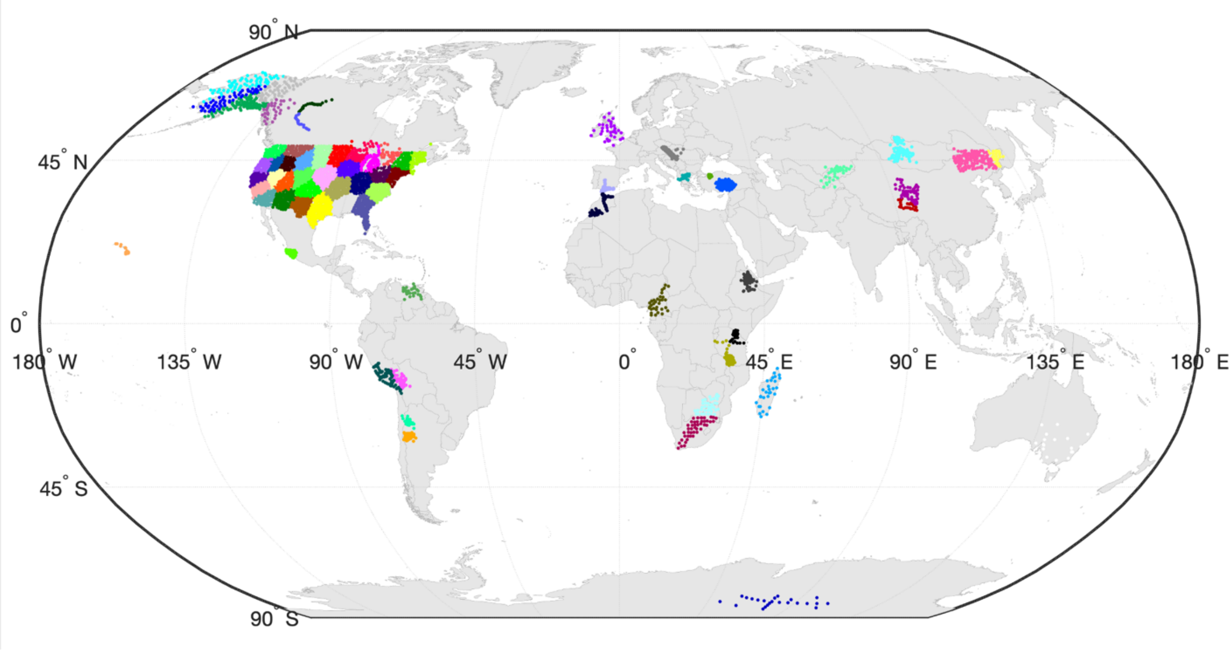

Figure 4.1. Global distribution of seismometers. The seismometers used in this study are shown as dots. Each cluster of the same color dots indicates an array. There are 67 arrays in total. For densely spaced seismometers, the individual dots cannot be seen, and the region appears filled in by one color (e.g., the United States).

4.2. Data

Seismic data were openly accessed through the Incorporated Research Institutions for Seismology Data Management Center. Our search query targeted seismic networks with >15 three-component broadband seismometers that recorded continuously for a minimum of one year. Additionally, we considered teleseismic P waveforms from 30-90° source-receiver distances. In total, 5,255 seismometers (Figure 4.1) were used to produce 240,890 receiver functions. The Transportable Array receiver functions for the contiguous United States were computed by previous studies (Schmandt et al., 2015; Zhang et al., 2021). Sampling density was variable between networks; therefore, we modified their configurations to make them more cohesive. We considered array aperture, natural separations in station geometry, tectonic province, number of receiver functions, and receiver function similarity from 350-600 km depth to configure arrays. All arrays were arranged using the following workflow, except for the Transportable Array which is discussed in the next paragraph. If the array aperture was >500 km and there were >1,500 observations, then it was split into multiple arrays based on the array geometry, previous studies, or approximate tectonic provinces. If the waveforms between a split array were dissimilar (e.g., had a cross correlation coefficient <0.9 or the depth lag was >4 km), then we considered each individually. Alternatively, if the waveforms were similar, then the original array was not split. An example of an array split based on tectonic province would be for large arrays that span subduction zones, the data was split into arrays with and without shallow (<200 km) subducting slab interference using global slab depth estimates (e.g., Figure 4.2b). Thirty-two arrays were formed using this method.

For the USArray in the contiguous United States and Alaska, we used k-means clustering to form the final arrays. There are 31 arrays for the contiguous United States. There are 5 arrays for Alaska, one array was formed for the shallow slab (<200 km; Hayes, 2018) and afterward, four were formed using k-means clustering (Figure 4.2b). The irregular array geometry resulting from k-means was more compatible with the suite of irregular geometries from the global arrays compared to the even geometry that results from splitting stations using a regular distance interval (e.g., Zhang, 2022).

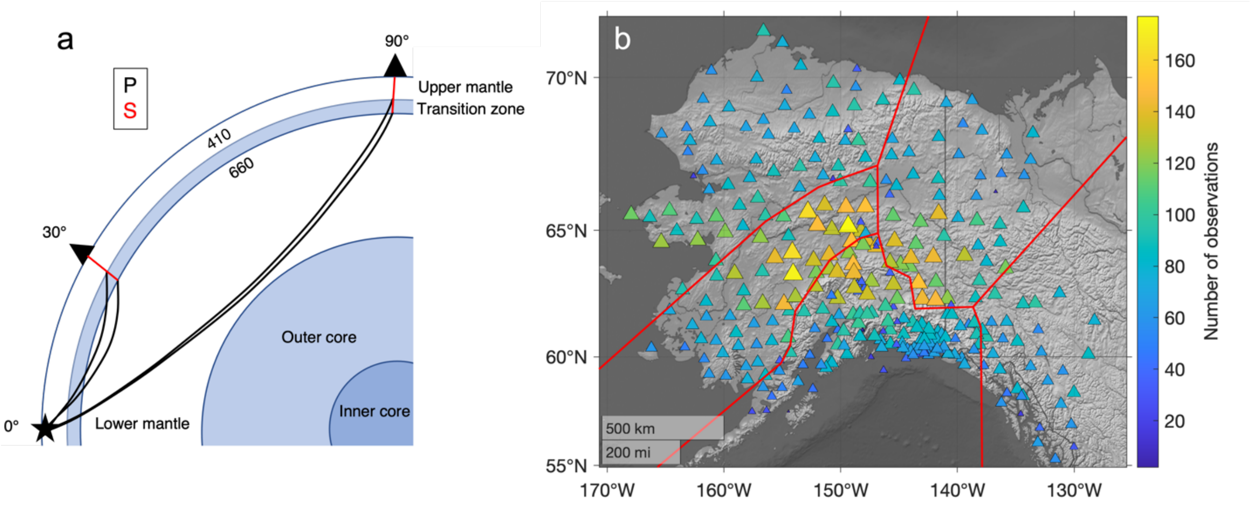

Figure 4.2. Example of teleseismic P-to-S ray paths and array configuration. a) Schematic of the ray paths for P-to-S conversions at the 410 and 660 discontinuities for a 30-

and 90-degree source-receiver distance. Seismometers are black triangles. The earthquake is represented by a black star. b) The stations (triangles) are colored by the number of observations (see color bar). Red lines indicate the boundaries of the five arrays formed from these stations. The southern array was formed using a contour for the shallow subducting slab (<200 km). The four remaining clusters were formed using k-means clustering.

4.3. Methods

4.3.1. Observed receiver functions

P-to-S (Ps) receiver functions were calculated from three-component seismic data using a multiband spectral deconvolution method (Mercier et al., 2006; Hansen & Dueker, 2009). The Ps receiver functions were filtered in four frequency bands, each with a low corner of 0.03 Hz and high corners of 0.2, 0.3, 0.4, and 0.5 Hz. For each array, the 5% furthest distance from the mean receiver function were considered outliers and removed. The moveout was corrected using ray tracing with a 1-D profile calculated as the average of 1-D profiles beneath each station from a 3-D tomography model (GLAD-M25; Lei et al., 2020). The depth-domain receiver functions were stacked. The uncertainties of the stacked receiver functions were estimated using bootstrap resampling with 500 iterations.

4.3.2. Probabilistic inversion

A Monte Carlo Markov Chain (MCMC) method was used to invert observed Ps receiver functions for 12 parameters spanning the mantle transition zone. The inversion space has four parameters per discontinuity including a top and bottom Vs and depth for each discontinuity, the 410, 520, and 660 (Figure 4.3a). Thus, each discontinuity is represented as a linear gradient over a finite depth interval. Synthetic Ps receiver functions were calculated using a reflectivity code (Levin & Park, 1997) with identical slowness sampling, filtering and moveout correction as the observed receiver functions. The attenuation effects were corrected using the structure from PREM (Dziewonski and Anderson, 1981). The frequency bands with high corners of 0.2, 0.3, 0.4, and 0.5 Hz were weighted in the inversion by using misfit scaling factors of 1, 2, 5, and 10, respectively. Technically, the waveforms using a 0.5 Hz high-frequency corner contain the full signal available for constraining the discontinuities but including lower frequency bands helps guide the inversion toward optimal models, especially for more gradual gradients such as the 520 (Zhang, 2022).

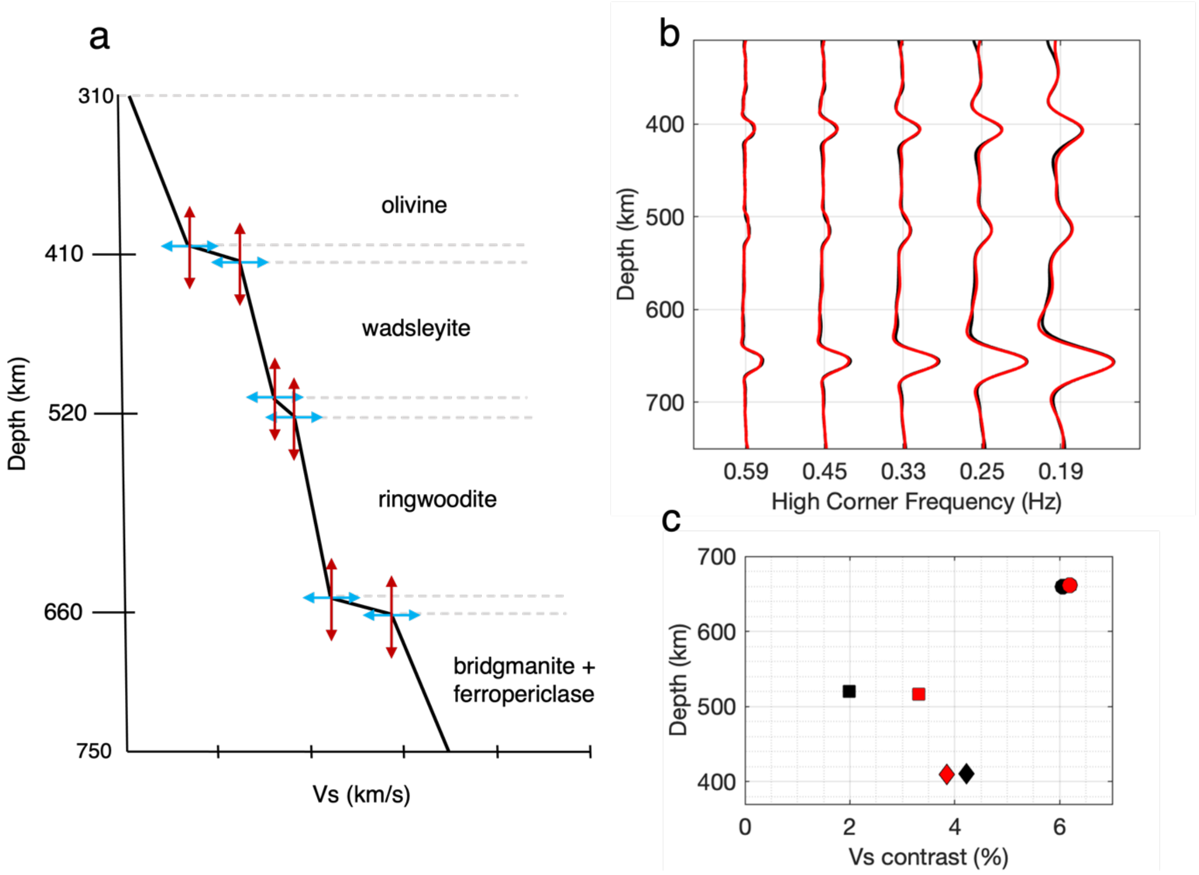

Figure 4.3. Inversion schematic and recovery test. a) A schematic of the parameter space for the inversion. The 12 parameters that can vary in the inversion are marked by arrows. b-c) An example of an inversion test. b) Input synthetic waveforms are black and output synthetic waveforms made from averaging the 200 best models are red. c) The black markers show the input parameters used to model the black waveforms in (b). The red markers show the average of the 200 best model parameters from the inversion that were used to make the red waveforms in (b). For this test, the width of each discontinuity is 20 km. The discontinuity width is the difference between the top and bottom of the discontinuity- see dashed lines in (a).

	410	520	660
Depth (km)	375-445	470-600	615-705
Width (km)	0.1 - 40		
Vs (km/s)	4.6-6.4		
Vs contrast (%)	Positive		

Table 4.1. Prior distribution of inversion parameters. Discontinuity names in top row and parameters in left column.

Metropolis Hastings sampling was used to draw samples from the prior distributions (Table 4.1). The discontinuity depth sampling step was 1.5 km, and the Vs step was adjusted by array, ranging from 0.005-0.1 km/s, so that the acceptance rate fell between 30-50% (Bissig et al., 2020). Each inversion begins with ak135 (Kennett et al., 1995) plus a 520 discontinuity but the starting point for the final inversion is updated to be the last accepted point during the Vs step testing. For each array, the MCMC inversion sampled 100,000 models by running 10 chains with 10,000 iterations. For each model, the misfit ($S(m)$) was calculated using depth-migrated waveform segments from 310-750 km depth. The inversion seeks to minimize the difference between the observed stacks (d^{obs}) and the synthetic stacks (d^{syn}) using the following function:

$$S(m) = \frac{1}{N}\sum_{i,j}^{N}\left(\frac{w_j(d_{i,j}^{obs} - d_{i,j}^{syn})^2}{2(\sigma)_{i,j}^2}\right)$$

where N is the number of points from 310-750 km, w is the weight, σ is the d^{obs} uncertainty i is for each sample point, and j is for each frequency band. The likelihood function ($L(m)$) is related to the misfit function by:

$$L(m) = \exp\left(-\frac{1}{2}S(m)\right)$$

At each step, a model is proposed and compared to the last accepted step. The new model is always accepted when its likelihood is greater than the last accepted model (e.g., if its misfit is lower). Additionally, the new model is accepted if the ratio between the likelihood functions of the new model and last accepted model is greater than a random variable generated between 0 and 1. The next model is chosen based on the last accepted point. An example of the posterior distribution of the accepted model parameters from the MCMC method can be found in Figure 4.S1.

Averaging the solutions with the lowest misfit ($S(m)$) from the posteriors creates a stabler solution than the single lowest misfit result (Bodin et al., 2012). The average parameters of the 200 lowest misfit models composed the final solution for each array (Figure 4.S1). The standard deviation of model parameters was calculated for the ensemble of acceptable solutions. We focused on the depth, Vs contrast, and width parameters. The depth was measured as the average of the top and bottom depth from the linear gradient (Figure 4.3a). We calculated the Vs contrast as the percent difference in Vs after extrapolating the Vs gradients above and below the discontinuity to the discontinuity depth (Zhang, 2022). This method removes the effect that discontinuity width has on Vs contrast. The width was measured as the difference between the top and bottom discontinuity depth.

The recovery of the inversion was tested for four cases with variable Vs-depth gradients at each discontinuity. The input waveforms were made using the reflectivity code (Levin & Park, 1997) with an Earth model resembling ak135 (Kennett et al., 1995) plus a 520-km discontinuity. The width of the discontinuities was systematically changed between tests: 1 km, 10 km, 20 km, 30 km. The depths remained centered on 410, 520, and 660 regardless of the widths. We note that changing the width also changes the total Vs contrast due to the background velocity gradients above and below each discontinuity. Figure 4.3 displays the results of the test using 20-km width discontinuities and Figure 4.S2 includes the 1-km width test. The waveform characteristics were well fit at all frequency bands (Figure 4.3b). The depth, Vs contrast, and width were well recovered for the 410, 520, and 660 (Figure 4.3 d-f).

4.4. Results

The inversion with observational data is similarly capable of fitting stacked waveforms at multiple frequencies as the inversion tests (Figure 4.4). The highest frequency stacks from the best modeled waveforms typically have slightly lower maximum amplitudes than the observed discontinuity amplitudes and the converse is true for the lowest frequency stacks (Figure 4.4b). The increased complexity of the observed 520 and 660, which may include multiple phase transitions, may lead to a worse fit of these discontinuities with 1-D synthetics compared to the better fit and simpler single-phase transition of the 410. Table 4.2 lists the ranges and averages from inversion results for each discontinuity and Figure 4.5 displays their histogram distributions. However, we mainly focus on the 410 results and suggest our inversion method works well for this simpler discontinuity. The 410 Vs contrast ranges from 2.7-8.7% and the average Vs contrast is 5.3% with ± 1.2% standard deviation (Figure 4.5a). The 410 depth ranges from 405-440 km and the average depth is 424.1 with ± 5.8 km standard deviation (Figure 4.5b). Although the 660 seismic discontinuity may be complicated by multiple phase transitions, its depth was well fitted (Figure 4.4b), therefore we used it to estimate mantle transition zone thickness. The mantle transition zone thickness, measured as the distance between the 410 and 660, ranges from 231-264 km and the mean thickness is 248 with ± 6.7 km standard deviation (Figure 4.S3).

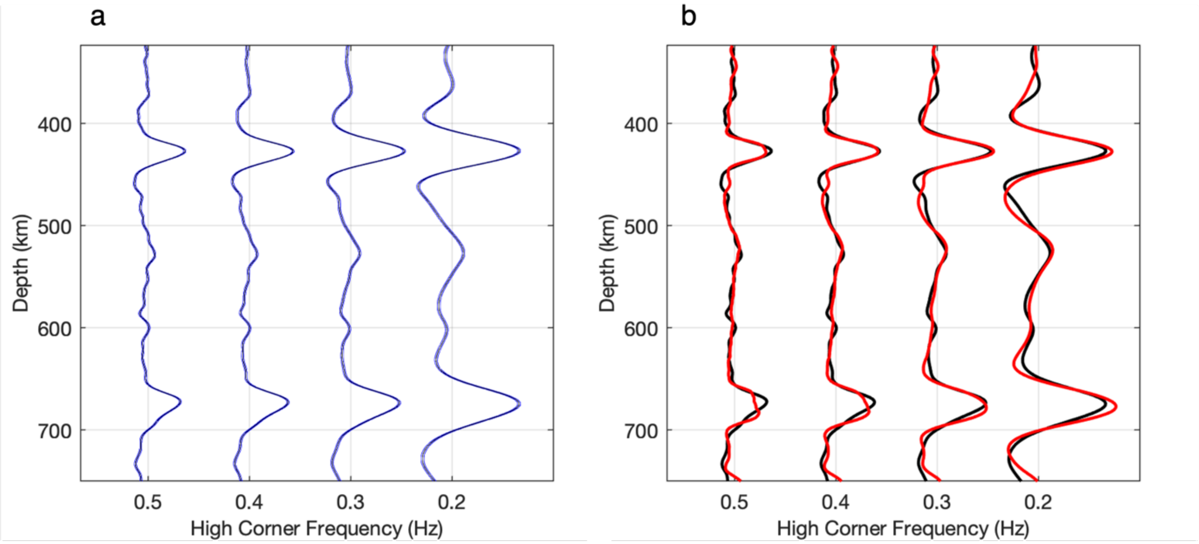

Figure 4.4. Observed and modeled receiver functions. a) The observed receiver function is a thin black line and the observational uncertainty from bootstrap resampling is plotted as thin blue lines. b) The observed receiver function stacks from (a) are black. The modeled receiver function stacks from averaging the 200 best models from the inversion are red lines. Waveforms are plotted from left to right by decreasing high corner frequency (see horizontal axis). The observational waveforms are an example from Mongolia.

	410	520	660
Vs contrast (%)	2.7-8.7	0.4-4.3	2.2-8.0
Average Vs contrast (%)	5.3 ± 1.2	1.5 ± 0.8	5.2 ± 1.2
Depth (km)	405-440	491-550	646-687
Average depth (km)	424.1 ± 5.8	511 ± 12.9	672.5 ± 8.1
Width (km)	10.2-35.1	13.48-35.4	17.4-38.3
Average width (km)	24.4 ± 6.1	25±4.2	29.3 ± 5.4

Table 4.2. Best inversion posteriors. The ranges and averages of parameters from the 200 best models following inversion. Averages include ± one standard deviation.

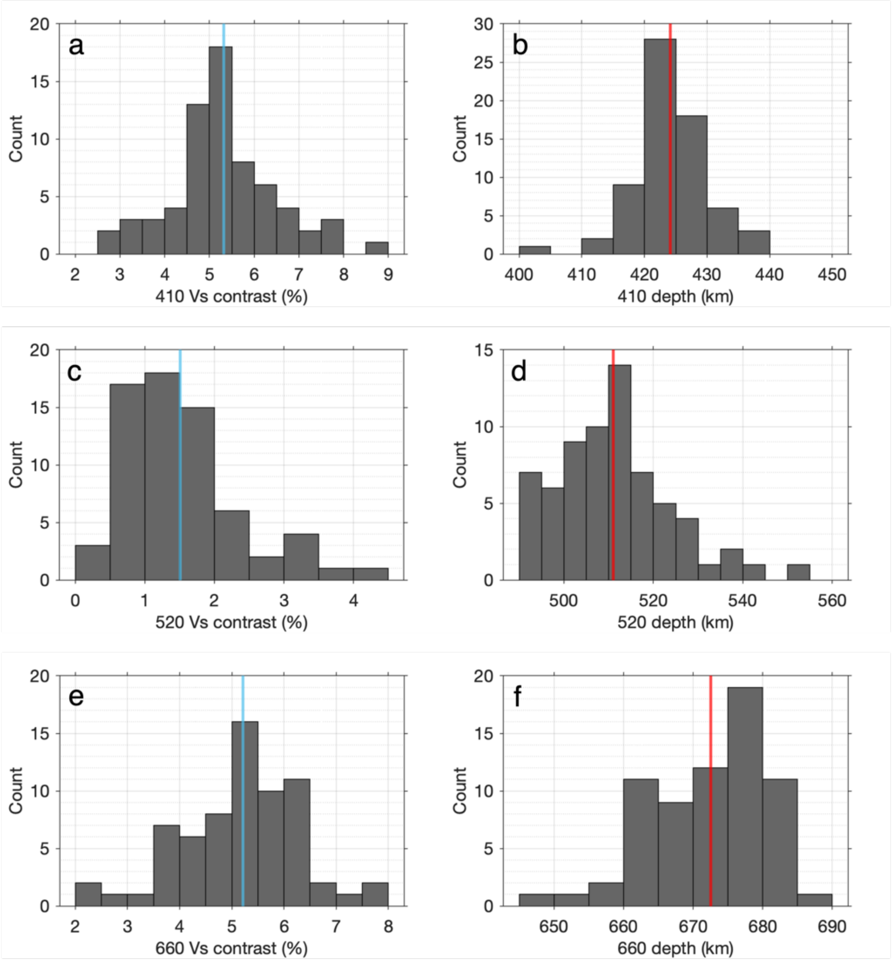

Figure 4.5. Histogram distributions from the best inversion results. Histogram distributions of inversion results for the a-b) 410-km discontinuity, c-d) 520-km discontinuity, and e-f) 660-km discontinuity. The first column (a, c, e) displays Vs contrast histograms with a blue line marking the average Vs contrast. The second column (b, d, f) displays depth with a red line marking the average depth.

4.5. Discussion

4.5.1. Mantle transition zone properties

The 410 and 520 depths should be positively correlated since each has a positive Clapeyron slope. However, if water is present, it will elevate the 410 and depress the 520 leading to a negative correlation between their depths. We found the 410- and 520-km depths are positively correlated with a correlation coefficient of 0.45 (Figure 4.6a). The slope of the best fit line (York et al., 2004) between the 410 and 520-km depths falls between the ratio of their Clapeyron slopes from mineral physics predictions (Katsura et al., 2004; Inoue et al., 2006; Suzuki et al., 2000; Figure 4.6). The agreement between our model and mineral physics predictions confirms thermal variations predominately control their topographies. Furthermore, most of our observations are inconsistent with hydration which would lead to a negative correlation between 410 and 520 depths.

The width of mantle discontinuities can be gleaned from studies that consider the frequency dependence of receiver function amplitudes (Schmandt, 2012; Goes et al., 2022). Decreasing the width of the discontinuity increases the P-to-S amplitude (e.g., Figure 4.S2). The 410 width is affected by composition, not temperature. The average width of the 410 in our study is 24.4 ± 6.1 km. The range in widths, 10-35 km, suggests composition varies between regions. Variable hydration (Frost & Dolejš, 2007) and/or differences in Mg-Fe content between regions (Chen et al., 2002; Katsura, 2022) could help explain the variable widths we observe. In a water-rich scenario, the width of the 410 will increase. However, this is only expected for the 410 when temperatures are lower than the ambient mantle (<1400 °C) and water is greater than 0.5 wt. % (Frost & Dolejš, 2007).

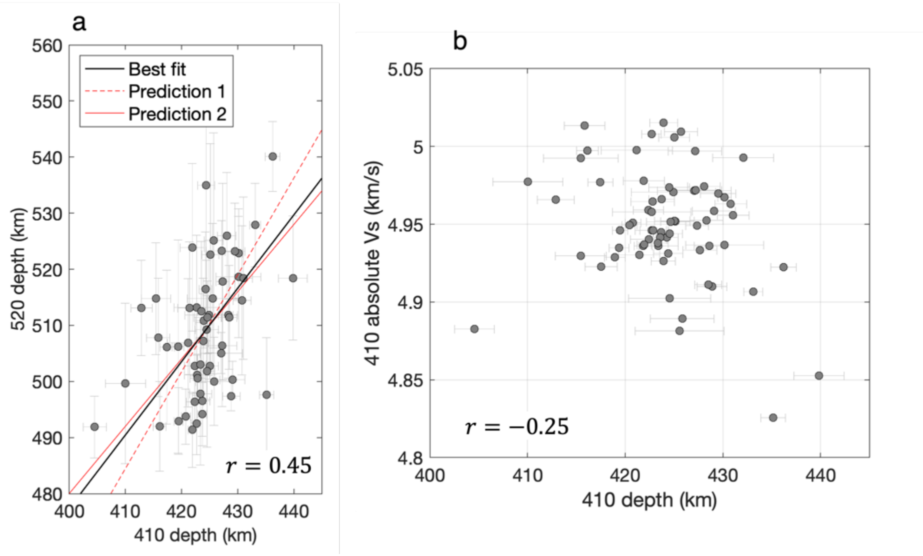

Figure 4.6. Comparison of predictions and observations. a) The 410- versus 520-km discontinuity depths for each array are marked by gray circles and their uncertainties by gray bars. Arrays that have a standard deviation for the 520-km discontinuity depth greater than 20 km were removed. The slope (1.7) form Equation 1 comes from mineral physics predictions in Katsura et al., (2004) and Suzuki et al., (2000). The slope (1.2) from Equation 2 comes from mineral physics predictions in Katsura et al., (2004) and Inoue et al., (2006). Our best fit line is black with slope 1.3. The correlation coefficient (r) of 0.45 is printed in the figure. b) Absolute Vs (average from 350-450 km) from GLAD-M25 tomography model (Lei et al., 2020) versus 410-km discontinuity depth from our inversion results. The correlation coefficient of -0.25 is printed in the figure.

4.5.2. Olivine content at the 410

The lower mantle may be poorly mixed and contain boundaries that resist flow and material exchange. Alternatively, the upper mantle is considered well mixed and the 410 is considered flow enhancing (Ringwood, 1991). The mantle is thought to be a mechanical mixture of harzburgite and basalt and has a pyrolytic composition. The olivine content of pyrolite is variable between studies but typically falls between 56-65 vol. % (Frost, 2008; Ringwood, 1962). In this paper, we consider pyrolite to be 60 vol. % olivine. Therefore, in this paper pyrolite is composed of 80% harzburgite (~75% olivine plus ~25% pyroxene-garnet) plus 20% basalt (100% pyroxene-garnet). Compositional heterogeneity in the mantle is expected from geodynamic models that consider plate tectonics and convection (Yan et al., 2020). The 410 Vs contrast depends most strongly on olivine composition. Hydration can also affect the Vs contrast. We estimated the olivine content for a dry (0 wt. % water) and wet (2 wt. % water) scenario by combining our Vs contrast results with mineral physics estimates (Figure 4.7a). The effect of iron was not considered because it similarly decreases the Vs of olivine and wadsleyite and therefore, should not significantly affect the Vs contrast of the 410. The Fe # in olivine above the 410 was assumed to be 6.5 and the Fe # in wadsleyite below the 410 was assumed to be 8.4 based on the pyrolite phase equilibrium experiments by Ishii et al., (2020). We did not consider high- and low-temperature cases because temperature only slightly affects the 410 Vs contrast (Figure 4.S4).

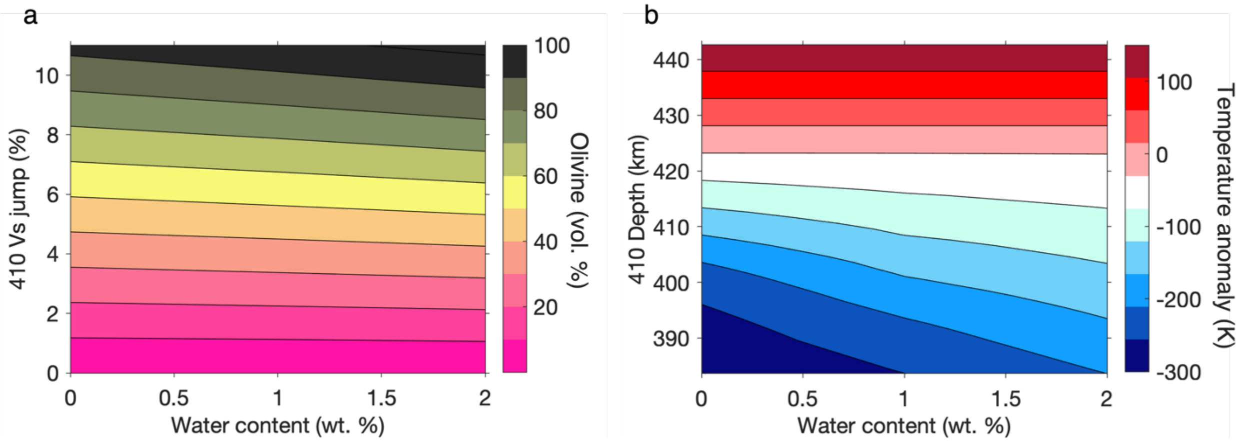

Figure 4.7. Mineral physics predictions for the 410. a) Estimates of olivine content (%) as a function of water content (wt. %) and the 410-km discontinuity Vs contrast (%) assuming 14.2 GPa (at 423 km depth) and 1830 K. b) Estimates of temperature anomaly (K) as a function of water content (wt. %) and 410-km discontinuity depth (km). Water does not affect the 410-km discontinuity depth above 1830 K.

The pyrolite model predicts a higher olivine content, ~60% olivine fraction for the dry condition, than the dry condition average in this study, 45 ± 10 vol. % (Table 4.3; Figure 4.8). The average 45 vol. % olivine suggests a more basalt-rich composition (~40%) compared to the 80% harzburgite plus 20% basalt composition for the pyrolite model. The 2.7-8.7% range in 410 Vs contrasts are consistent with ~25-70 vol. % olivine for the dry condition and 30-80 vol. % olivine for the wet condition (Table 4.3; Figure 4.8; Figure 4.9). Some geodynamic models predict a narrower range, 50 to 67.5 vol %, in olivine at 410 depths (Figure 4.6e from Goes et al., 2022).

	410 dry (0 wt. %)	410 wet (2 wt. %)
Olivine (vol. %)	24 to 72	27 to 80
Average olivine (vol. %)	45 ± 10	50 ± 11
Temperature anomaly (K)	-190 to 170	-94 to 170
Average temperature (K)	10 ± 60	18 ± 46

Table 4.3. Olivine fraction and temperature anomaly for the 410. The ranges and averages of olivine content and temperature anomaly across the 410 for dry and wet cases. Averages include ± one standard deviation.

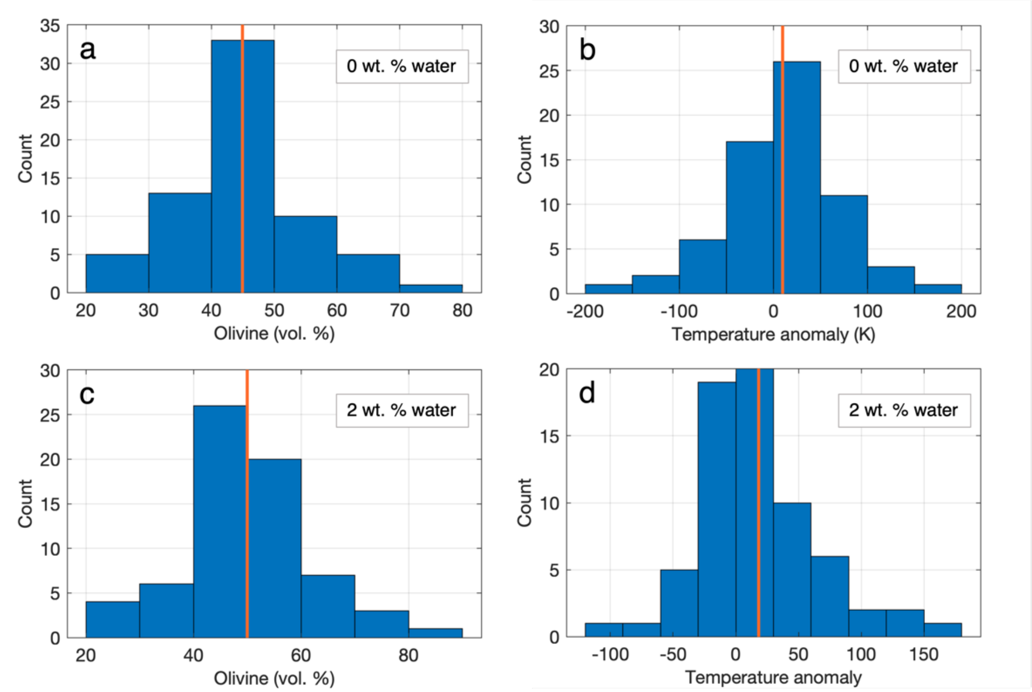

Figure 4.8. Distributions of 410 olivine content and temperature anomaly. Histogram distribution of a & c) olivine content and b & d) temperature anomaly for the dry (0 wt. % water) and wet (2 wt. % water) cases in the top (a, b) and bottom (c, d) rows. The orange lines indicate the averages.

Greater than 60% of the arrays fall within the 40-60 vol. % olivine content for the wet and dry cases (Figure 4.8 a & c). Some of the regions that fall within the mean range are most of the central U.S., eastern Antarctica, most of Alaska, northwestern Canada, Cameroon, Morocco, the Balkans, and Turkey. The most harzburgite-rich regions are Hawaii, the United Kingdom, the southern Tibetan plateau (Figure 4.9), and the northwestern most, southwestern most, and mid-southern U.S. arrays. The most basalt-rich regions are Peru and Bolivia, Mexico, an array in the northwestern U.S., South Africa, southern Tanzania, Spain, and southeastern Australia.

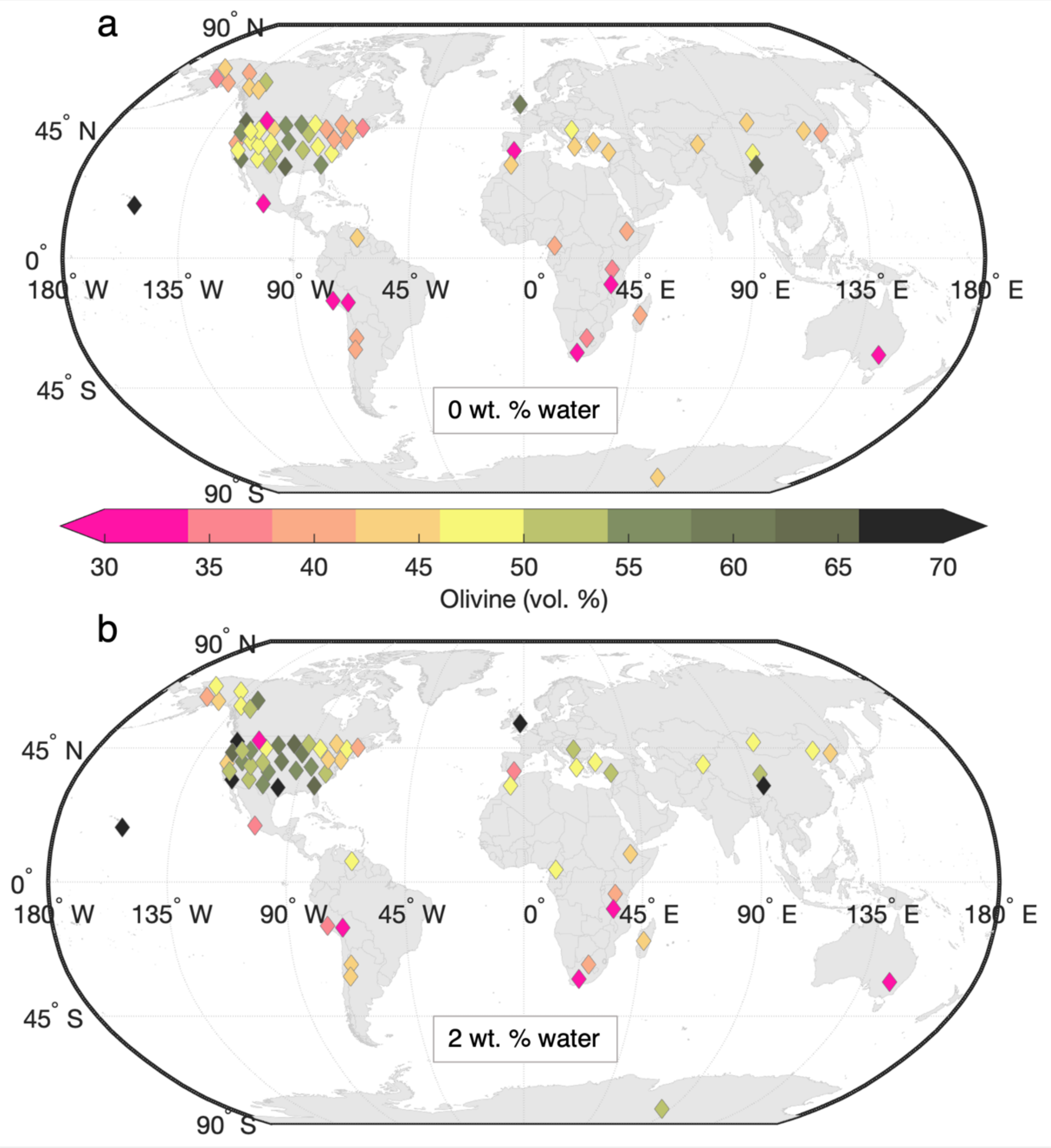

Figure 4.9. Global olivine map at 410-km discontinuity. Estimate of olivine fraction for a) dry (0 wt. % water) and b) wet (2 wt. % water) cases using the Vs contrast from each array with mineral physics estimates from Figure 4.7a.

4.5.3. Temperature at the 410

Variations in discontinuity depths are often attributed to temperature anomalies. We estimated temperature anomalies assuming 1830 K and 14.2 GPa at our average 410 depth of 424 km (Figure 4.7b). Water does not affect the depth of the 410 when temperature is higher than 1830 K (Figure 4.7b). The temperature anomalies inferred from the 410 depths range from −190 to 170 K in the dry case and −94 to 170 K in the wet case (Table 4.3; Figure 4.10). The negative correlation coefficient of −0.25 between the average absolute Vs beneath each array from Lei et al., (2020) and the 410 depths (Figure 4.6b) suggests absolute temperatures could be inferred using the 410 depths with adiabatic temperature profiles (e.g., Katsura, 2022). Geodynamic models of tectonic plate recycling produce thermal heterogeneity in the mantle with the coolest regions corresponding to subduction and warmest regions corresponding to plumes (Yan et al., 2020). Similarly, we find the largest positive temperature anomalies at the hotspot setting of Hawaii and Afar, as well as the east African spreading center (Figure 4.10). We did not observe a strong correlation with subduction settings being cooler. In general, the mantle beneath the US has a warmer temperature anomaly across its western flank and a cooler anomaly across its eastern flank which is consistent with the more active tectonics along its western margin.

The topography of the 410 in this study varies from ~405-440 km which is slightly narrower but consistent with global ranges observed from long period precursor studies (e.g., Huang et al., 2019; Houser et al., 2008). One advantage of long period precursor studies is the ability to compile a global map of 410 depth by interpolating between the broad distribution of underside reflections that result from source-receiver geometry. However, sampling blind spots remain in some regions. The Afar hotspot below Ethiopia is one region that is often under sampled by SS precursor studies (e.g., Figure 4.11b; Huang et al., 2019; Waszek et al., 2021; Houser et al., 2008) leading to poorly constrained and variable mantle transition zone discontinuity depths in this region. For example, the SS precursor studies by Huang et al., (2019) and Waszek et al., (2021) suggest the depth of the 410 beneath the Afar region is ~400-405 km, whereas the study by Houser et al., (2008) suggests the 410 beneath the same area is ~434-437 km. The depth of the 410 beneath the Ethiopian array in our study is 435 km which disagrees with the ~400-405 km depth estimate (Figure 4.11; Huang et al., 2019). We suggest the dense sampling near our array and shorter path between the 410 and receiver yield better depth estimates for the 410. Furthermore, the temperature is expected to be elevated near the potential Afar plume and our depth of ~435 km is consistent with a positive temperature anomaly of ~150 K.

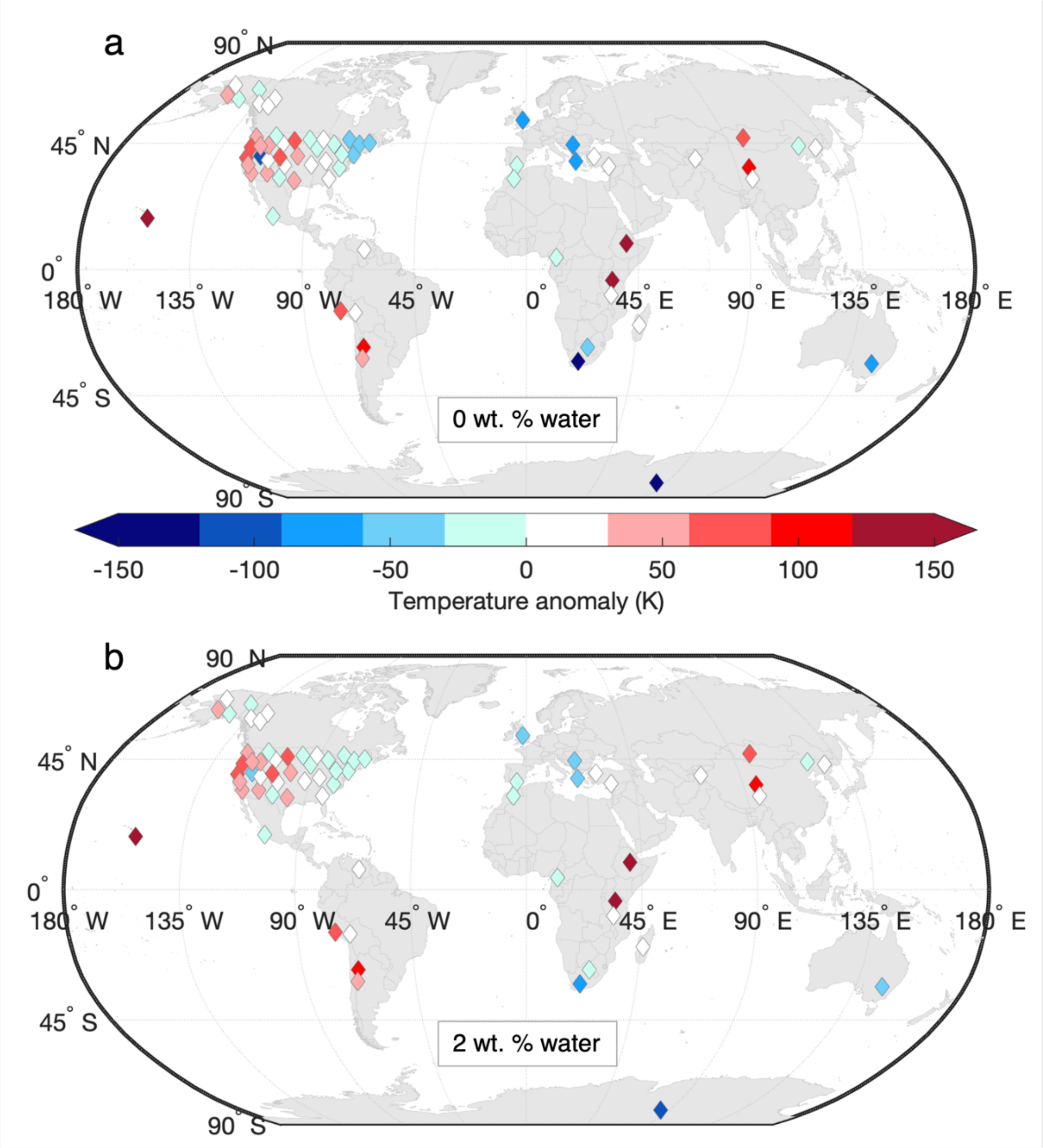

Figure 4.10. Global temperature map at 410-km discontinuity. Estimate of temperature for a) dry (0 wt. % water) and b) wet (2 wt. % water) cases using the 410-km discontinuity depth at each array with mineral physics estimates in Figure 4.7b. The temperature anomaly corresponds to 1830 K (e.g., 0=1830 K).

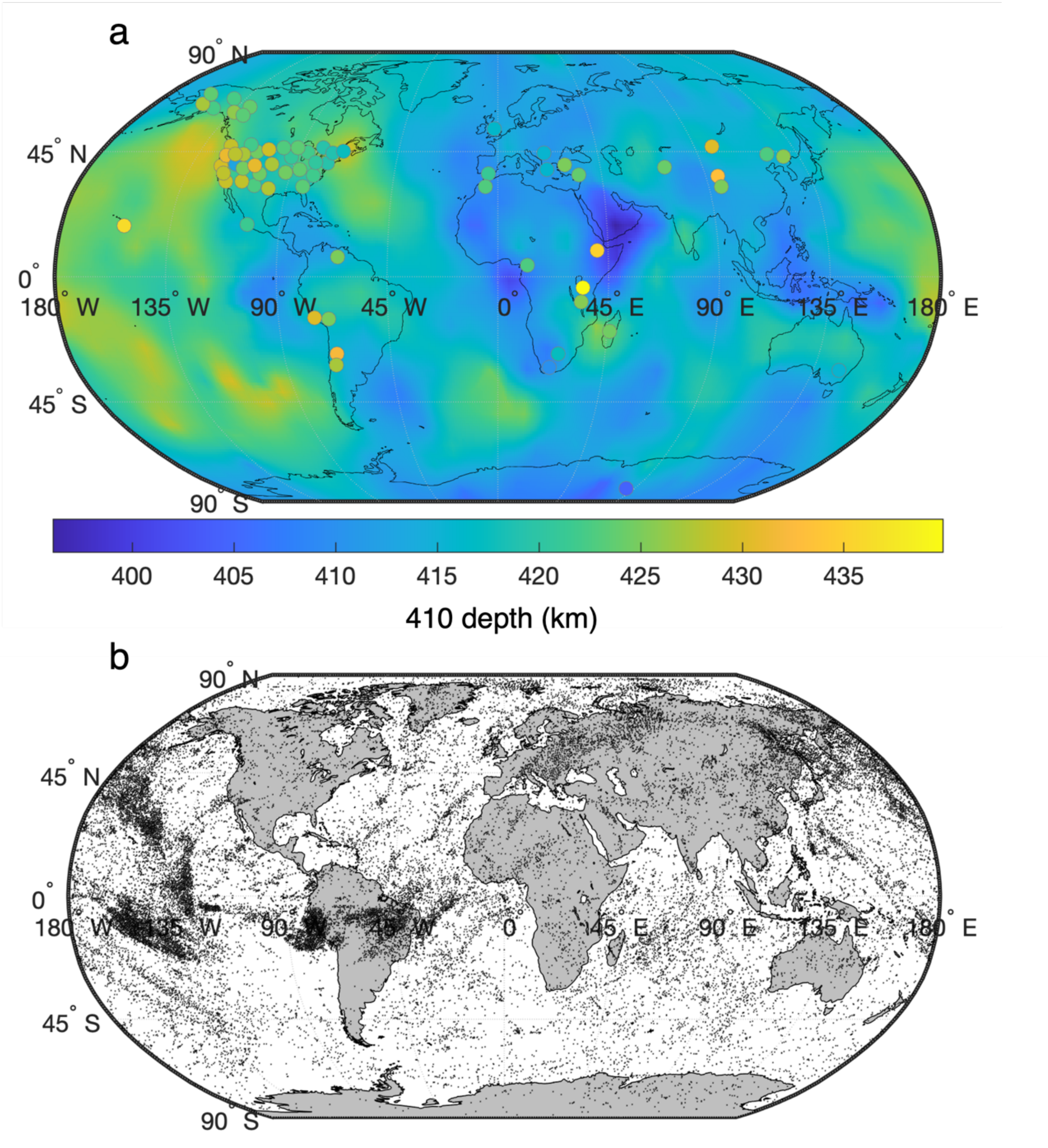

Figure 4.11. Comparison of 410 depths between two studies. a) The background color displays 410 depths from the Huang et al., (2019) SS precursor study. Circles correspond to the 410 depths sampled from arrays in our study. b) The global sampling distribution of the 410 from Huang et al. (2019). Each black dot marks the point where the 410 was sampled.

4.6. Conclusions

We used a broad distribution of dense seismic arrays to sample the mantle transition zone which bridges two commonly used approaches, globally distributed single-station studies and dense array studies of small regions. The systematic processing and inversion of teleseismic P-to-S receiver functions allowed us to directly compare mantle transition zone structure between regions. We focused on results from the relatively simpler 410, compared to the 520 and 660, and used its seismic parameters to estimate the variability of temperature and olivine content in the upper mantle. The average olivine content of 45-50 vol. % is 10-15 vol. % lower than the pyrolite model suggests. The range in olivine abundance from ~25-80 vol. % suggests the 410 is compositionally heterogeneous. The variation in 410 depths from 405-440 km corresponds to an approximate 300 K range in temperature. Similarly to results from deeper mantle seismic discontinuities, our results suggest the upper mantle near the 410 is laterally heterogeneous despite being well mixed. Future studies of the deeper mantle transition zone would aid from an inversion method that incorporates the potential multiphase boundaries of the 520 and 660.

4.7. Supplementary Information

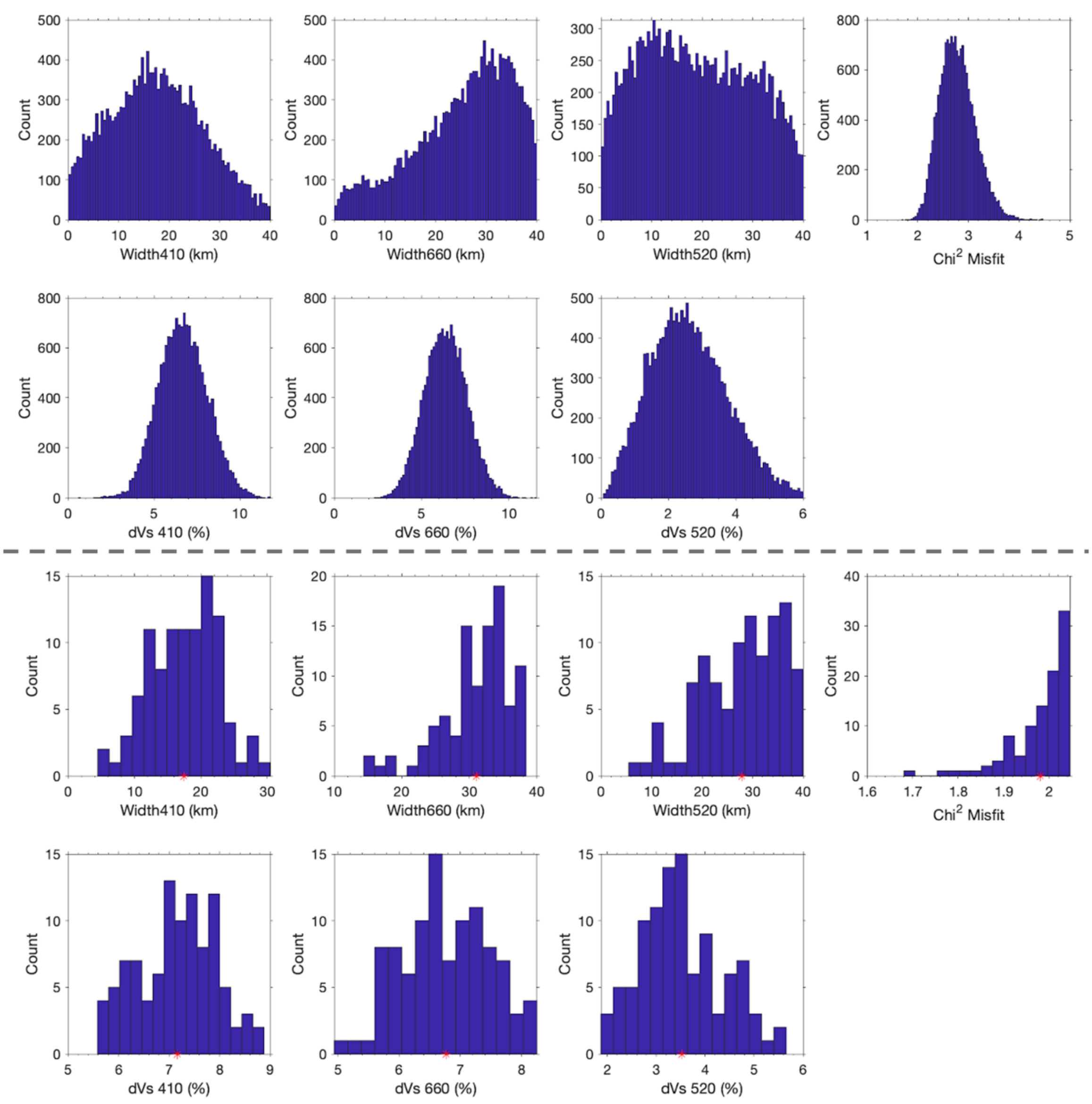

Figure 4.S1. Posterior distribution example. This example is for the Ireland and United Kingdom seismic array. The top 2 rows display the histogram distributions of all accepted models during the Monte Carlo Markov Chain inversion. The bottom two rows display the histogram distributions of the 200 lowest misfit models. The average of the lowest misfit results is indicated by a red star on the horizontal axis.

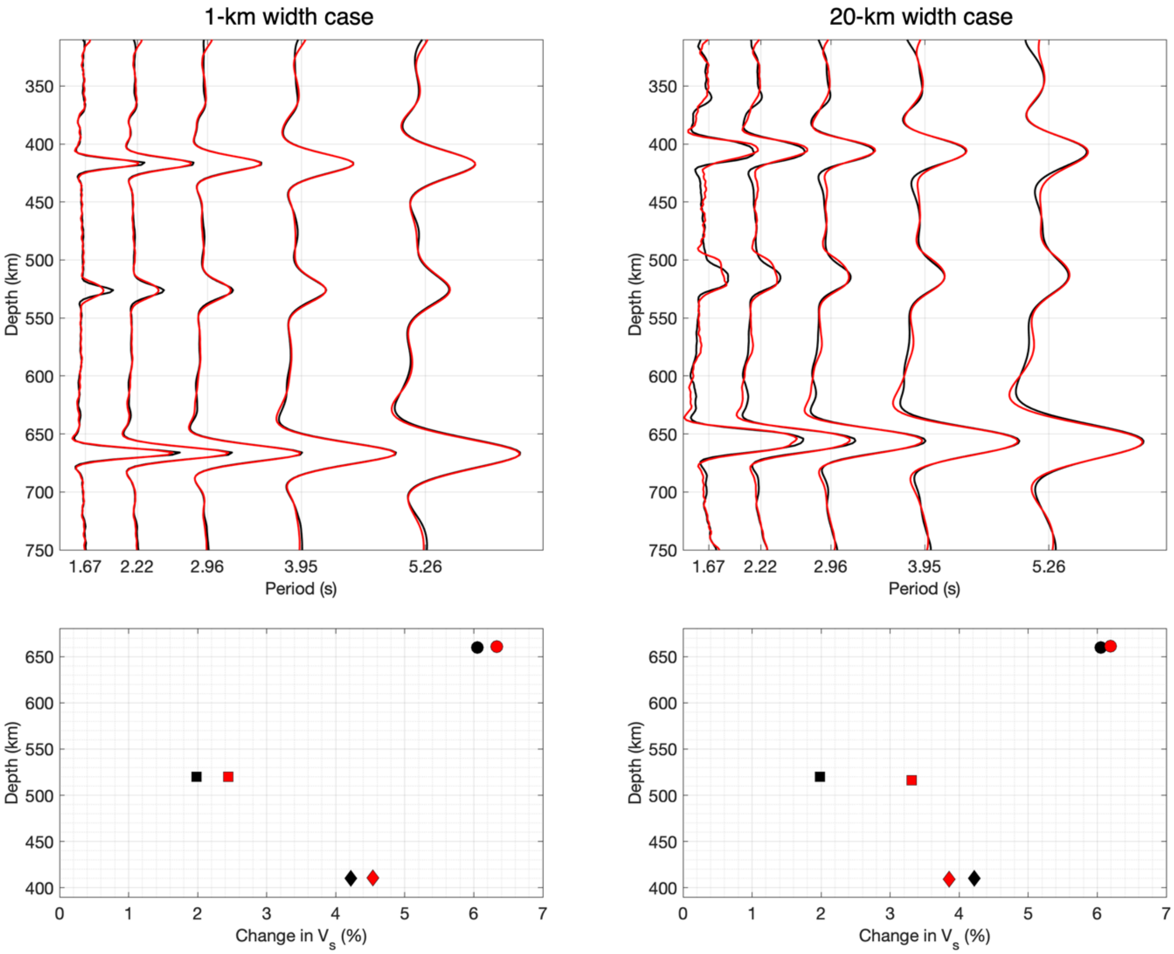

Figure 4.S2. Inversion recovery tests. Two examples are shown here, a & c) for 1-km and b & d) for 20-km width discontinuities. The discontinuity width is the difference between the top and bottom of the discontinuity- see dashed lines in Figure 4.2a of the main text. a-b) Input synthetic waveforms are black. Output synthetic waveforms made from averaging the best 200 inversion results are red. c-d) The input and output parameters used to make the waveforms in (a, b). The black markers show the input parameters used to model the black waveforms and the red markers show the average 200 best parameters output from the inversion that were used to make the red waveforms.

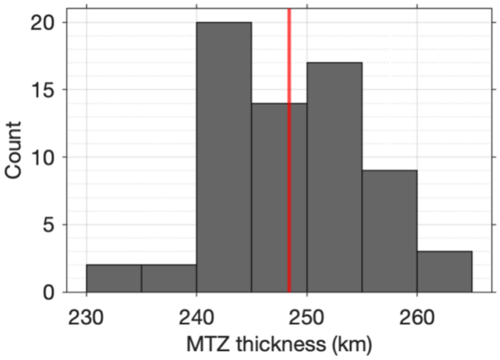

Figure 4.S3. Mantle transition zone thickness. The mantle transition zone thickness was measured as the distance between the 410 km discontinuity and the 660 km discontinuity. The thickness ranges from 231-264 km and the mean thickness is marked by a red line. The mean thickness is 248 with ± 6.7 km standard deviation.

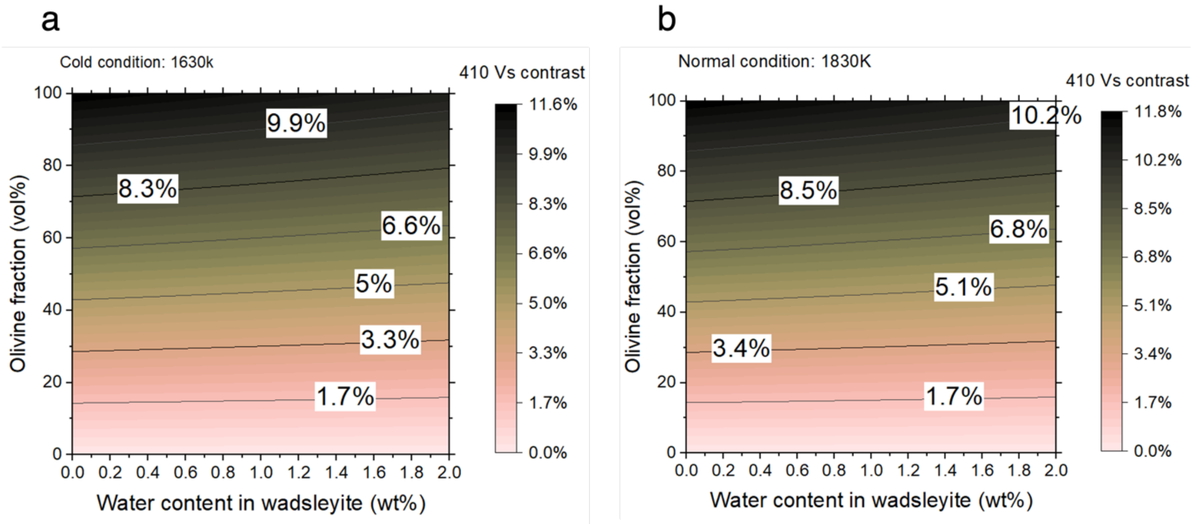

Figure 4.S4. The effect of temperature on 410 Vs contrast. Estimates of 410 Vs contrast as a function of water content and olivine content in a) a cold condition at 1630 K and b) a normal condition at 1830 K.

References

Allen, R. V. (1978). Automatic earthquake recognition and timing from single traces. *Bull. seism.* Soc. Am., 68(5), 1521–1532.

Ansari, E., Bidgoli, T. S., & Hollenbach, A. (2019). Accelerated fill-up of the Arbuckle Group aquifer and links to U.S. midcontinent seismicity. *Journal of Geophysical Research: Solid Earth, 124*, 2670–2683. https://doi.org/10.1029/ 2018JB016926

ANSS ComCat (2021). Advanced National Seismic System Comprehensive Earthquake Catalog. Retrieved from https://earthquake.usgs.gov/data/comcat/. (Accessed Feb 2021).

ANSS ComCat (2022). Advanced national seismic system comprehensive earthquake catalog. Retrieved from https://earthquake.usgs.gov/ data/comcat/ (Accessed Aug 2022).

Bachmann, C. E., Weimer, S., Goertz-Allmann, B. P., & Woessner, J. (2012). Influence of pore-pressure on the event-size distribution of induced earthquakes, *Geophys. Res. Lett., 39,* L09302, doi:10.1029/2012GL051480.

Baiesi, M., & Paczuski, M. (2004). Scale-free networks of earthquakes and aftershocks, *Phys. Rev. E, 69*, 066106, doi:10.1103/PhysRevE.69.066106.

Ballmer, M. D., Schmerr, N. C., Nakagawa, T., & Ritsema, J. (2015). Compositional mantle layering revealed by slab stagnation at~ 1000-km depth. Science advances, 1(11), e1500815.

Baltz E.H. (1965). Stratigraphy and history of the Raton basin and notes on San Luis basin, Colorado-New Mexico. *American Association of Petroleum Geologists Bulletin, v. 49*, 2041-2075.

Barbour, A. J., Norbeck, J. H., & Rubinstein, J. L. (2017). The effects of varying injection rates in Osage County, Oklahoma, on the 2016 Mw 5.8 Pawnee earthquake. *Seismological Research Letters, 88(4)*, 1040. https://doi.org/10.1785/0220170003

Barnhart, W. D., Benz, H. M., Hayes, G. P., Rubinstein, J. L., & Bergman, E. (2014), Seismological and geodetic constraints on the 2011 Mw5.3 Trinidad, Colorado earthquake and induced deformation in the Raton Basin, *J. Geophys. Res. Solid Earth, 119*, 7923–7933, doi:10.1002/ 2014JB011227.

Blackwell, D. D., Richards, M. C., Frone, Z. S., Batir, J. F., Williams, M. A., Ruzo, A. A., & Dingwall, R. K., (2011). SMU Geothermal Laboratory Heat Flow Map of the Conterminous United States, 2011. Retrieved from http://www.smu.edu/geothermal

Bodin, T., Sambridge, M., Tkalčić, H., Arroucau, P., Gallagher, K., & Rawlinson, N. (2012). Transdimensional inversion of receiver functions and surface wave dispersion. Journal of Geophysical Research: Solid Earth, 117(B2).

Bollinger, G. A., Adams, M. J., Henrisy, R. F., & Langer, C. J. (1983). The Denver earthquake sequence of March-April 1981, *Earthquake Notes, 54,* 3-12.

Bonner, J. L., Blackwell, D. D., & Herrin, E. T. (2003). Thermal constraints on earthquake depths in California, *Bulletin Seismol. Soc. Am., 93*, 2333-2354, doi:10.1785/0120030041

Brodsky, E. E., & Lajoie, L. J. (2013). Anthropogenic seismicity rates and operational parameters at the Salton Sea Geothermal Field. *Science, 341(6145)*, 543–546. https://doi.org/10.1126/science.1239213

Cammarano, F., Goes, S., Vacher, P., & Giardini, D. (2003). Inferring upper-mantle temperatures from seismic velocities. *Physics of the Earth and Planetary Interiors*, *138*(3-4), 197-222.

Cao, A., & Levander, A. (2010). High-resolution transition zone structures of the Gorda Slab beneath the western United States: Implication for deep water subduction. Journal of Geophysical Research: Solid Earth, 115(B7).

Chamberlain, C. J., Frank, W. B., Lanza, F., Townend, J., & Warren- Smith, E. (2021). Illuminating the pre-, co-, and post-seismic phases of the 2016 M7.8 Kaikōura earthquake with 10 years of seismicity. Journal of Geophysical Research: Solid Earth, 126, e2021JB022304. https://doi. org/10.1029/2021JB022304

Chambers, K., Woodhouse, J. H., & Deuss, A. (2005). Topography of the 410-km discontinuity from PP and SS precursors. *Earth and Planetary Science Letters*, *235*(3-4), 610-622.

Chang, K. W., & Segall, P. (2016), Injection-induced seismicity on basement faults including poroelastic stressing, *J. Geophys. Res. Solid Earth*, *121*, 2708–2726, doi:10.1002/2015JB012561.

Chen, K., Avouac, J. P., Aati, S., Milliner, C., Zheng, F., & Shi, C. (2020). Cascading and pulse-like ruptures during the 2019 Ridgecrest earthquakes in the Eastern California Shear Zone. Nature communications, 11(1), 1-8.

Cochran, E. S., Ross, Z. E., Harrington, R. M., Dougherty, S. L., & Rubinstein, J. L. (2018). Induced earthquake families reveal distinctive evolutionary patterns near disposal wells. *Journal of Geophysical Research: Solid Earth*, *123*, 8045–8055. https://doi.org/10.1029/2018JB016270.

Cochran, E. S., Wickham-Piotrowski, A., Kemna, K., Harington, R., Dougherty, S., & Castro, A. P., (2020). Minimal clustering of injection-induced earthquakes observed with a large-n seismic array. *Bulletin of the Seismological Society of America, 110(5)*, 2005-2017. https://doi.org/10.1785/0120200101.

COGCC (2021). Colorado Oil and Gas Conservation Commission. Retrieved from http://cogcc.state.co.us/data.html#/cogis. (Accessed Feb 2021).

Dane, C. H., & Bachman, G. O. (1965). Geologic Map of New Mexico, *U. S. Geological Survey*, Scale 1:500.000

Dempsey, D., & Riffault, J. (2019). Response of induced seismicity to injection rate reduction: Models of delay, decay, quiescence, recovery, and Oklahoma. *Water Resources Research*, *55*, 656–681. https://doi.org/10.1029/2018WR023587

Deuss, A., & Woodhouse, J. (2001). Seismic observations of splitting of the mid-transition zone discontinuity in Earth's mantle. Science, 294(5541), 354-357.

Dreger, D. S. (2003). TDMT_INV: Time domain seismic moment tensor inversion. In W. H. K. Lee et al., (eds.), *International Handbook of Earthquake and Engineering Seismology, Part B, Int. Geophys. Ser (Vol. 81*, p. 1627). New York: Academic Press.

Dziewonski, A. M., & Anderson, D. L. (1981). Preliminary reference Earth model. Physics of the earth and planetary interiors, 25(4), 297-356.

Earle, P. S., & Shearer, P. M. (1994). Characterization of global seismograms using an automatic-picking algorithm. *Bull. Seismol. Soc. Am., 84(2)*, 366–376.

Elliott, J. L., Grapenthin, R., Parameswaran, R. M., Xiao, Z., Freymueller, J. T., & Fusso, L. (2022). Cascading rupture of a megathrust. Science advances, 8(18), eabm4131.

Ellsworth, W. L. (2013). Injection-induced earthquakes. *Science, 341(6142)*, 1225942. https://doi.org/10.1126/science.1225942

Farrell, S., Husen, & Smith, R.B. (2009). Earthquake swarm and b-value characterization of the Yellowstone volcano-tectonic system. *J. Volcanol. Geotherm. Res.188*, 260–276.

Finzi, Y., Langer, S., 2012. Damage in step-overs may enable large cascading earthquakes. Geophys. Res. Lett. http://dx.doi.org/10.1029/2012GL052436 (5 pp.).

Flores, R. M., & Bader, L. R. (1999). A summary of Tertiary coal resources of the Raton Basin, Colorado and New Mexico, chap. SR of Fort Union Coal Assessment Team, 1999 Resource Assessment of Selected Tertiary Coal Beds and Zones in the Northern Rocky Mountains and Great Plains Region: *U.S. Geological Survey Professional Paper 1625-A*

Fossen, H., & Rotevatn, A. (2015). Fault linkage and relay structures in extensional settings - A review. Earth-Science Reviews, 154, 14-28.

Frohlich, C. (2012). Two-year survey comparing earthquake activity and injection-well locations in the Barnett Shale, Texas. *Proceedings of the National Academy of Sciences, 109*, 35, 13934-13938

Frohlich, C., Hayward, C., Rosenblit, J., Aiken, C., Hennings, P., Savvaidis, A., Lemons, C., Horne, E., Walter, J. I., & DeShon, H. R. (2020). Onset and cause of increased seismic activity near Pecos, West Texas, United States, from observations at the Lajitas TXAR Seismic Array. *Journal of Geophysical Research: Solid Earth*, *125*(1), e2019JB017737.

Frost, D. & Dolejš, D. (2007). Experimental determination of the effect of H2O on the 410-km seismic discontinuity. Earth Planet. Sci. Lett. 256, 182–195.

Frost, D. J. (2008). The upper mantle and transition zone. Elements, 4(3), 171-176.

Gao, S. S., & Liu, K. H. (2014). Mantle transition zone discontinuities beneath the contiguous United States. Journal of Geophysical Research: Solid Earth, 119(8), 6452-6468.

Goebel, T. H. W., Hosseini, S. M., Cappa, F., Hauksson, E., Ampuero, J. P., Aminzadeh, F., & Saleeby, J. B. (2016). Wastewater disposal and earthquake swarm activity at the southern end of the Central Valley, California. *Geophysical Research Letters, 43*, 1–8. https://doi.org/10.1002/2015GL066948

Goebel, T. H. W., Rosson, Z., Brodsky, E. E., & Walter, J. I. (2019). Aftershock deficiency of induced earthquake sequences during rapid mitigation efforts in Oklahoma. *Earth and Planetary Science Letters, 522*, 135–143. https://doi.org/10.1016/j.epsl.2019.06.036

Goebel, T. H., & Brodsky, E. E. (2018). The spatial footprint of injection wells in a global compilation of induced earthquake sequences. *Science*, *361(6405)*, 899-904.

Goebel, T. H., Weingarten, M., Chen, X., Haffener, J., & Brodsky, E. E. (2017). The 2016 Mw5.1 Fairview, Oklahoma earthquakes: Evidence for long-range poroelastic triggering at >40 km from fluid disposal wells. Earth and Planetary Science Letters, 472, 50–61. https://doi.org/10.1016/j.epsl.2017.05.011

Goes, S., Yu, C., Ballmer, M. D., Yan, J., & van der Hilst, R. D. (2022). Compositional heterogeneity in the mantle transition zone. *Nature Reviews Earth & Environment*, *3*(8), 533-550.

Gutenberg, B., & Richter, C. F. (1956). Earthquake magnitude, intensity, energy, and acceleration. *Bull. Seismol. Soc. Am. 46*, 105–145.

Hainzl, S., and Ogata, Y. (2005). Detecting fluid signals in seismicity data through statistical earthquake modeling, *J. Geophys. Res., 110*, B05S07, doi:10.1029/2004JB003247.

Hamling, I. J., Hreinsdóttir, S., Clark, K., Elliott, J., Liang, C., Fielding, E., ... & Stirling, M. (2017). Complex multifault rupture during the 2016 M w 7.8 Kaikōura earthquake, New Zealand. Science, 356(6334), eaam7194.

Hansen, S., Dueker, K., (2009). P- and S-wave receiver function images of crustal imbrication beneath the Cheyenne belt in southeast Wyoming. Bull. Seismol. Soc. Am, http://dx.doi.org/10.1785/0120080168.

Harte, D. (2010), PtProcess: an R package for modeling marked point process indexed by time. *J. Stat. Softw.*, *35(8)*, 1-32.

Hayes, G., 2018, Slab2 - A Comprehensive Subduction Zone Geometry Model: U.S. Geological Survey data release, https://doi.org/10.5066/F7PV6JNV

Healy, J. H., Rubey, W. W., Griggs, D. T., & Raleigh, C. B. (1968). The Denver earthquakes. *Science 161 (3848)*, 1301–10.

Hemborg, T.H. (1998). Spanish Peak Field, Las Animas County, Colorado: Geologic setting and early development of a coalbed methane reservoir in the central Raton Basin. *Colorado Geological Survey*, Resource Series 33, 34p.

Hooft E.E.E., Toomey D.R., and Solomon S.C., (2003). Anomalously thin transition zone beneath the Galapagos hotspot. Earth and Planetary Science Letters 216: 55–64.

Houser, C., Masters, G., Flanagan, M., Shearer, P., (2008). Determination and analysis of long-wavelength transition zone structure using SS precursors. Geophys. J. Int. 174, 178–194.

Hsieh, P. A., & Bredehoeft, J. D. (1981). A reservoir analysis of the Denver earthquakes: A case of induced seismicity, *Journal of Geophysical Research, v. 86*, 903–920, doi:10.1029/JB086iB02p00903.

Huang, Q., Schmerr, N., Waszek, L., & Beghein, C. (2019). Constraints on seismic anisotropy in the mantle transition zone from long-period SS precursors. Journal of Geophysical Research: Solid Earth, 124(7), 6779-6800.

Ide, S. (2019). Frequent observations of identical onsets of large and small earthquakes. Nature, 573(7772), 112-116.

Inoue, T., Irifune, T., Higo, Y., Sanehira, T., Sueda, Y., Yamada, A., ... & Utsumi, W. (2006). The phase boundary between wadsleyite and ringwoodite in Mg2SiO4 determined by in situ X-ray diffraction. Physics and Chemistry of Minerals, 33(2), 106-114.

Ishii, T., Miyajima, N., Sinmyo, R., Kojitani, H., Mori, D., Inaguma, Y., & Akaogi, M. (2020). Discovery of new-structured post-spinel MgFe2O4: Crystal structure and high-pressure phase relations. *Geophysical Research Letters*, *47*(6), e2020GL087490.

Ita, J., & Stixrude, L. (1992). Petrology, elasticity, and composition of the mantle transition zone. Journal of Geophysical Research: Solid Earth, 97(B5), 6849-6866.

Jenkins, J., S. Cottaar, R. S. White, and A. Deuss, (2016). Depressed mantle discontinuities beneath Iceland: Evidence of a garnet controlled 660 km discontinuity?, Earth Planet. Sci. Lett., 433, 159–168, doi:10.1016/j.epsl.2015.10.053.

Johnson, R. B. (1969). Geologic map of the Trinidad quadrangle, south-central Colorado, *U. S. Geological Survey*, Miscellaneous Geologic Investigations Map I-558.

Johnson, R. B., & Wood, H. H., Jr. (1956). Stratigraphy of upper Cretaceous and Tertiary rocks of Raton Basin, Colorado and New Mexico. *American Association of Petroleum Geologists Bulletin, V. 40*, p. 707-721.

Johnson, R. C., & Finn, T. M. (2001). Potential for a Basin-Centered Gas Accumulation in the Raton Basin, Colorado and New Mexico. *USGS Bulletin,* 2184-B.

Joubert, C., Sohrabi, R., Rubinstein, J. L., Jansen, G., & Miller, S. A. (2020). Injection-Induced Earthquakes Near Milan, Kansas, Controlled by Karstic Networks, *Geophys. Res. Lett.*, *47*(21), 1–9, doi:10.1029/2020GL088326.

Kagan, Y. Y., & Jackson, D. D. (1991). Long-term earthquake clustering. *Geophysical Journal International, 104(1)*, 117–134. https://doi.org/10.1111/j.1365-246X.1991.tb02498.x

Karlstrom, K. E., Crossey, L. J., Hilton, D. R., and Barry, P. H. (2013). Mantle He-3 and CO_2 degassing in carbonic and geothermal springs of Colorado and implications for neotectonics of the Rocky Mountains. *Geology, 41*, pp. 495-498

Katsura, T. (2022). A revised adiabatic temperature profile for the mantle. *Journal of Geophysical Research: Solid Earth*, *127*(2), e2021JB023562.

Katsura, T., Ito, E., (1989). The system Mg2 SiO4 –Fe2 SiO4 at high pressures and temperatures: precise determination of stabilities of olivine, modified spinel, and spinel. J. Geophys. Res., Solid Earth (1978–2012) 94 (B11), 15663–15670.

Katsura, T., Yamada, H., Nishikawa, O., Song, M., Kubo, A., Shinmei, T., ... & Funakoshi, K. I. (2004). Olivine-wadsleyite transition in the system (Mg, Fe) 2SiO4. Journal of Geophysical Research: Solid Earth, 109(B2).

Kennett, B. L., Engdahl, E. R., & Buland, R. (1995). Constraints on seismic velocities in the Earth from traveltimes. Geophysical Journal International, 122(1), 108-124.

Keranen, K. M., & Weingarten, M. (2018). Induced seismicity. *Annual Review of Earth and Planetary Sciences, 46(1)*, 149–174. https://doi.org/10.1146/annurev-earth-082517-010054

Keranen, K. M., Weingarten, M., Abers, G. A., Bekins, B. A., & Ge, S. (2014). Sharp increase in central Oklahoma seismicity since 2008 induced by massive wastewater injection. *Science, 345(6195)*, 448-451.

Kissling, E., Ellsworth, W., Eberhart-Phillips, D., & Kradolfer, E. (1994). Initial reference models in local earthquake tomography. Journal of Geophysical Research, 99, 19635–19646. https://doi.org/10.1029/93jb03138

Knapmeyer-Endrun, B., Krüger, F., Legendre, C. P., Geissler, W. H., & PASSEQ Working Group. (2013). Tracing the influence of the Trans-European Suture Zone into the mantle transition zone. Earth and Planetary Science Letters, 363, 73-87.

Kothari, S., Shcherbakov, R., & Atkinson, G. (2020). Statistical modeling and characterization of induced seismicity within the Western Canada Sedimentary Basin. *Journal of Geophysical Research: Solid Earth, 125*, e2020JB020606. https://doi.org/ 10.1029/2020JB020606

Kraft, T., & Deichmann, N. (2014). High-precision relocation and focal mechanism of the injection-induced seismicity at the Basel EGS, *Geothermics, 52,* 59–73, doi: 10.1016/j.geothermics.2014.05.014.

Langenbruch, C., Weingarten, M. & Zoback, M. D. (2018). Physics-based forecasting of man-made earthquake hazards in Oklahoma and Kansas. *Nat. Commun. 9*, 3946.

Lawrence, J. F., & Shearer, P. M. (2006). Constraining seismic velocity and density for the mantle transition zone with reflected and transmitted waveforms. Geochemistry, Geophysics, Geosystems, 7(10).

Lei, W., Ruan, Y., Bozdağ, E., Peter, D., Lefebvre, M., Komatitsch, D., et al. (2020). Global adjoint tomography—model GLAD-M25. Geophysical Journal International, 223(1), 1–21. https://doi.org/10.1093/gji/ggaa253

Lei, X., Wang, Z., & Su, J. (2019) Possible link between long-term and short-term water injections and earthquakes in salt mine and shale gas site in Changning, south Sichuan Basin, China, *Earth and Planetary Physics*, *3(6)*, 510-525.

Lei, X., Yu, G., Ma, S., Wen, X., & Wang, Q. (2008). Earthquakes induced by water injection at ~3 km depth within the Rongchang gas field, Chongqing, China, *J. Geophys. Res., 113*, doi: 10.1029/2008JB005604.

Levin, V., & Park, J. (1997). P-SH conversions in a flat-layered medium with anisotropy of arbitrary orientation. Geophysical Journal International, 131(2), 253-266.

Li Y. G., Vidale J. E., Aki K., & Marone, C. J. (1994). Fine structure of the Landers fault zone: segmentation and the rupture process. *Science, 265*, 367.

Li, Z., Elsworth, D. & Wang, C., (2021). Constraining maximum event magnitude during injection-triggered seismicity. Nat. Commun. 12, 1–9.

Liu, M., Zhang, M., Zhu, W., Ellsworth, W. L., & Li, H. (2020). Rapid characterization of the July 2019 Ridgecrest, California, earthquake sequence from raw seismic data using machine learning phase picker. *Geophysical Research Letters, 47*, e2019GL086189. https://doi.org/10.1029/2019GL086189

Llenos, A. L., & Michael, A. J. (2016). Characterizing potentially induced earthquake rate changes in the Brawley Seismic Zone, Southern California. *Bulletin of the Seismological Society of America, 106(5)*, 2045–2062. https://doi.org/10.1785/0120150053

Llenos, A. L., & Michael, A. J., (2013). Modeling earthquake rate changes in Oklahoma and Arkansas: possible Signatures of induced seismicity. *Bull. Seismol. Soc. Am. 103*, 2850–2861. http://dx.doi.org/10.1785/0120130017

Lund Snee, J.-E., & Zoback, M. D. (2020). Multiscale variations of the crustal stress field throughout north America. *Nature Communications*, *11*(1), 1–9.

Martínez-Garzón, P., Kwiatek, G., Bohnhoff, M., & Dresen, G. (2016). Impact of fluid injection on fracture reactivation at The Geysers geothermal field. *J. Geophys. Res. Solid Earth, 121*, 7432–7449, doi:10.1002/2016JB013137

Martínez-Garzón, P., Zaliapin, I., Ben-Zion, Y., Kwiatek, G., & Bohnhoff, M. (2018). Comparative study of earthquake clustering in relation to hydraulic activities at geothermal fields in California. *Journal of Geophysical Research: Solid Earth, 123*, 4041–4062. https://doi.org/10.1029/2017JB014972

McGarr, A. (2014). Maximum magnitude earthquakes induced by fluid injection. *Journal of Geophysical Research: solid earth*, *119*(2), 1008-1019.

Mercier, J. P., Bostock, M. G., & Baig, A. M. (2006). Improved Green's functions for passive-source structural studies. Geophysics, 71(4), SI95-SI102.

Meremonte, M. E., Lahr, J. C., Frankel, A. D., Dewey, J. W., Crone, A. J., Overturf, D. E., et al. (2002). Investigation of an earthquake swarm near Trinidad, Colorado, August–October 2001. U.S Geol. Surv. Open-File Rept. 02-0073.

Milner, K. R., B. E. Shaw, and E. H. Field (2022). Enumerating Plausible Multifault Ruptures in Complex Fault Systems with Physical Constraints, Bull. Seismol. Soc. Am. XX, 1–19, doi: 10.1785/0120210322

Morgan, P. (2009). A Preliminary Analysis of Geothermal Resources in the Central Raton Basin, Colorado, from Bottom-Hole Temperature Data, *GRC Transactions, 33*, 509–513.

Mousavi, S. M., Ogwari, P. O., Horton, S. P., & Langston, C. A. (2017). Spatio-temporal evolution of frequency-magnitude distribution and seismogenic index during initiation of induced seismicity at Guy-Greenbrier, Arkansas. *Physics of the Earth and Planetary Interiors, 267*, 53–66. https://doi.org/10.1016/j.pepi.2017.04.005

Nakai, J. S., Sheehan, A. F., & Bilek, S. L. (2017a). Seismicity of the Rocky Mountains and Rio Grande Rift from the EarthScope Transportable Array and CREST temporary seismic networks, 2008–2010. *Journal of Geophysical Research: Earth Surface, 122*, 2173–2192. https://doi.org/ 10.1002/2016JB013389

Nakai, J. S., Weingarten, M., Sheehan, A. F., Bilek, S. L., & Ge, S. (2017b). A possible causative mechanism of Raton Basin, New Mexico and Colorado earthquakes using recent seismicity patterns and pore pressure modeling. *Journal of Geophysical Research: Solid Earth, 122(10)*, 8051-8065.

NMOCD (2021). New Mexico Oil and Conservation Division. Retrieved from https://wwwapps.emnrd.state.nm.us/ocd/ocdpermitting/Data/Wells.aspx. (Accessed Feb 2021)

Ogata, Y. (1988). Statistical models for earthquake occurrences and residual analysis for point processes. *Journal of the American Statistical Association, 83(401)*, 9–27. https://doi.org/10.1080/01621459.1988.10478560

Omori, F. (1894). On the aftershocks of earthquakes, *J. Coll. Sci. Imp. Univ. Tokyo, 7*, 111–200.

Palgunadi, K. H., A.-A. Gabriel, T. Ulrich, J. Á. López-Comino, and P. M. Mai (2020). Dynamic Fault Interaction during a Fluid-Injection-Induced Earthquake: The 2017 Mw 5.5 Pohang Event, Bull. Seismol. Soc. Am. 110, 2328–2349, doi: 10.1785/0120200106

Papadopulous, S. S., & Associates, Inc. (2008). Coalbed Methane Stream Depletion Assessment Study- Raton Basin, Colorado. In conjunction with: Colorado Geological Survey, Denver, Colorado.

Park, Y., Mousavi, S. M., Zhu, W., Ellsworth, W. L., & Beroza, G. C. (2020). Machine learning-based analysis of the Guy-Greenbrier, Arkansas earthquakes: A tale of two sequences. *Geophysical Research Letters, 47*, e2020GL087032. https://doi.org/10.1029/2020GL087032

Peterie, S. L., Miller, R. D., Intfen, J. W., & Gonzales, J. B. (2018). Earthquakes in Kansas induced by extremely far-field pressure diffusion. Geophysical Research Letters, 45, 1395–1401. https://doi.org/ 10.1002/2017GL076334

Philibosian, B., & Meltzner, A. J. (2020). Segmentation and supercycles: a catalog of earthquake rupture patterns from the Sumatran Sunda Megathrust and other well-studied faults worldwide. Quaternary Science Reviews, 241, 106390.

Pillmore, C. L. (1964). Geologic map of the Catskill SW quadrangle, Colfax County, New Mexico, *U. S. Geological Survey*, Open-File Report OF-64-123.

Pillmore, C. L. (1965a). Geologic map of the Catskill NE quadrangle, Colfax County, New Mexico, *U. S. Geological Survey*, Open-File Report OF-65-122.

Pillmore, C. L. (1965b). Geologic map of the Catskill SE quadrangle, Colfax County, New Mexico, *U. S. Geological Survey*, Open-File Report OF-65-121.

Pillmore, C. L. (1969). Geologic map of the Catskill NW quadrangle, New Mexico and Colorado, *U. S. Geological Survey*, Open-File Report OF-66-104.

Pillmore, C. L. (2003). Geologic map of the Vermejo Park quadrangle, Colfax County, New Mexico, and Las Animas County, Colorado, *U. S. Geological Survey*, Open-File Report OF-2003-438.

Raleigh, C. B., Healy, J. H., & Bredehoeft J. D., (1976). An experiment in earthquake control at Rangely, Colorado, *Science*, *191*, 1230–1237.

Reusch, A. M., Nyblade, A. A., Tibi, R., Wiens, D. A., Shore, P. J., Bekoa, A., ... & Nnange, J. M. (2011). Mantle transition zone thickness beneath Cameroon: evidence for an upper mantle origin for the Cameroon Volcanic Line. *Geophysical Journal International*, *187*(3), 1146-1150.

Reyes, C. & Wiemer, S. (2020). From ZMAP to ZMAP7: Fast-forwarding 25 years of software evolution, *EGU General Assembly 2020*, Online, 4–8 May 2020, EGU2020-18878, https://doi.org/10.5194/egusphere-egu2020-18878, 2020

Richter, C. F., Foreshocks and aftershocks, in Earthquakes in Kern County, California During 1952, Div. Mines Bull. 171, 199–202, 1955.

Ringwood, A. E. (1962). A model for the upper mantle, J. Geophys. Res., 67, 857–867, doi:10.1029/JZ067i002p00857.

Ringwood, A. E. (1991). Phase transformations and their bearing on the constitution and dynamics of the mantle. Geochim. Cosmochim. Acta 55, 2083–2110.

Roberts, N. S., Bell, A. F., & Main, I. G. (2015), Are volcanic seismic b-values high, and if so when? *J Volcanol Geotherm*, *Res 308*, 127–141. doi:10.1016/j.jvolgeores.2015.10.021

Ross, Z. E., Idini, B., Jia, Z., Stephenson, O. L., Zhong, M., Wang, X., ... & Jung, J. (2019). Hierarchical interlocked orthogonal faulting in the 2019 Ridgecrest earthquake sequence. Science, 366(6463), 346-351.

Rubinstein, J. L., Ellsworth, W. L., McGarr, A., & Benz, H. M. (2014). The 2001–present induced earthquake sequence in the Raton Basin of northern New Mexico and southern Colorado. *Bulletin of the Seismological Society of America, 104(5)*, 2162–2181. https://doi.org/10.1785/0120140009

Saikia, A., Frost, D. J., & Rubie, D. C. (2008). Splitting of the 520-kilometer seismic discontinuity and chemical heterogeneity in the mantle. Science, 319(5869), 1515-1518.

Saint Louis University (2021). North America Moment Tensor: Focal Mechanism Plots, Tables and Other Compilations, http://www.eas.slu.edu/eqc/eqc_mt/MECH.NA/ (last accessed July 2021)

Savage, H. M., K. M. Keranen, D. P. Schaff, and C. Dieck (2017), Possible precursory signals in damage zone foreshocks, Geophys. Res. Lett., 44, 5411–5417, doi:10.1002/2017GL073226.

Scanlon, B. R., Weingarten, M. B., Murray, K. E., & Reedy, R. C. (2019). Managing Basin-Scale Fluid Budgets to Reduce Injection-Induced Seismicity from the Recent U.S. Shale Oil Revolution. *Seismolog. Res. Lett., 90*, 171−182.

Schmandt, B. (2012), Mantle transition zone shear velocity gradients beneath USArray, Earth Planet. Sci. Lett., 355–356, 119–130.

Schmandt, B., Lin, F. C., & Karlstrom, K. E. (2015). Distinct crustal isostasy trends east and west of the Rocky Mountain Front. Geophysical Research Letters, 42(23), 10-290.

Schoenball, M., & Ellsworth, W. L. (2017a). Waveform-relocated earthquake catalog for Oklahoma and southern Kansas illuminates the Regional Fault Network. *Seismological Research Letters, 88(5)*, 1252–1258. https://doi.org/10.1785/0220170083

Schoenball, M., & Ellsworth, W. L. (2017b). A systematic assessment of the spatiotemporal evolution of fault activation through induced seismicity in Oklahoma and Southern Kansas: Induced seismicity evolution in Oklahoma, *J. Geophys. Res., 122(12)*, 10189– 10206, doi: 10.1002/2017JB014850

Schoenball, M., Davatzes, N. C., & Glen, J. M. (2015). Differentiating induced and natural seismicity using space-time-magnitude statistics applied to the Coso Geothermal field. *Geophysical Research Letters*, *42*(15), 6221-6228.

Schoenball, M., Walsh, F. R., Weingarten, M., & Ellsworth, W. L. (2018). How faults wake up: the Guthrie-Langston, Oklahoma earthquakes. *The Leading Edge, 37(2)*, 100-106.

Schwab, D. R., Bidgoli, T. S., & Taylor, M. H. (2017). Characterizing the potential for injection-induced fault reactivation through subsurface structural mapping and stress field analysis, Wellington Field, Sumner County, Kansas. *Journal of Geophysical Research: Solid Earth,* 122, 10,132–10,154. https://doi.org/10.1002/ 2017JB014071

Segall, P., & Lu, S. (2015), Injection-induced seismicity: Poroelastic and earthquake nucleation effects, *Journal of Geophysical Research: Solid Earth*, *120*, 5082–5103, doi:10.1002/2015JB012060.

Shearer, P. M., and M. P. Flanagan (1999). Seismic velocity and density jumps across the 410- and 660-kilometer discontinuities, Science, 285, 1545–1548.

Shen, L. W., Schmitt, D. R., Wang, R., & Hauck, T. E. (2021). States of in-situ stress in the Duvernay East Shale Basin and Willesden Green of Alberta, Canada: variable in-situ stress states effect fault stability. *Journal of Geophysical Research: Solid Earth*, e2020JB021221.

Shen, W., Ritzwoller, M. H., Schulte-Pelkum, V., & Lin, F. C. (2013). Joint inversion of surface wave dispersion and receiver functions: a Bayesian Monte-Carlo approach. Geophysical Journal International, 192(2), 807-836.

Simmons, N.A., & Gurrola, H., (2000). Multiple seismic discontinuities near the base of the transition zone in the Earth's mantle. Nature 405, 559–562.

Skoumal, R. J., & Trugman, D. T. (2021). The proliferation of induced seismicity in the Permian Basin, Texas. *Journal of Geophysical Research: Solid Earth, 126*, e2021JB021921. https://doi. org/10.1029/2021JB021921

Skoumal, R. J., Barbour, A. J., Brudzinski, M. R., Langenkamp, T., & Kaven, J. O. (2020). Induced seismicity in the Delaware Basin, Texas. *Journal of Geophysical Research: Solid Earth, 125*, e2019JB018558. https://doi.org/ 10.1029/2019JB018558

Slinkard, M., Schaff, D., Mikhailova, N., Heck, S., Young, C., & Richards, P. G. (2014). Multistation validation of waveform correlation techniques as applied to broad regional monitoring. Bulletin of the Seismological Society of America, 104(6), 2768-2781.

Snoke, J. A. (2003). FOCMEC: Focal mechanism determinations. *International handbook of earthquake and engineering seismology, 85*, 1629-1630.

Stoeser, D. B., Green, G. N., Morath, L. C., Heran, W. D., Wilson, A. B., Moore, D. W., & Van Gosen, B. S. (2007), Preliminary integrated geologic map databases for the United States: Central States: Montana, Wyoming, Colorado, New Mexico, North Dakota, South Dakota, Nebraska, Kansas, Oklahoma, Texas, Iowa, Missouri, Arkansas, and Louisiana, *United States Geological Survey, Open File Report (2005-1351)*, Version 1.2, Retrieved from http://pubs.usgs.gov/of/2005/1351/index.htm. (Accessed January 2021)

Sumy, D. F., Cochran, E. S., Keranen, K. M., Wei, M., and Abers, G. A. (2014). Observations of static Coulomb stress triggering of the November 2011 M5.7 Oklahoma earthquake sequence, *J. Geophys. Res. Solid Earth*, *119*, 1904–1923, doi:10.1002/2013JB010612.

Suzuki, A., Ohtani, E., Morishima, H., Kubo, T., Kanbe, Y., Kondo, T., ... & Kikegawa, T. (2000). In situ determination of the phase boundary between wadsleyite and ringwoodite in Mg2SiO4. Geophysical Research Letters, 27(6), 803-806.

Tackley, P. J. (1996). On the ability of phase transitions and viscosity layering to induce long wavelength heterogeneity in the mantle. Geophysical Research Letters, 23(15), 1985-1988.

Treiman, J. A., Kendrick, K. J., Bryant, W. A., Rockwell, T. K., & McGill, S. F. (2002). Primary surface rupture associated with the *M* 7.1 16 October 1999 Hector Mine earthquake, San Bernardino County, California. *Bull. Seismol. Soc. Am.*, *92***,** 1171-1191.

Trugman, D. T., & Shearer, P. M., (2017). GrowClust: A Hierarchical Clustering Algorithm for Relative Earthquake Relocation, with Application to the Spanish Springs and Sheldon, Nevada. *Earthquake Sequences. Seismol. Res. Lett. 88*, 379–391. doi:10.1785/0220160188

U. S. Geological Survey (2021). National Earthquake Information Center (NEIC), accessed July 2021 at https://www.usgs.gov/natural-hazards/earthquake-hazards/national-earthquake-information-center-neic?qt-science_support_page_related_con=3#qt-science_support_page_related_con

Uhrhammer, R. A., & Collins, E. R. (1990). Synthesis of Wood-Anderson seismograms from broadband digital records. *Bulletin of the Seismological Society of America*, *180 (3)*, 702-216. https://doi.org/10.1785/BSSA0800030702

Utsu, T. (1961). A statistical study on the occurrence of aftershocks, *Geophys. Mag., 30*, 521–605.

van Stiphout, A. M., Cottaar, S., & Deuss, A. (2019). Receiver function mapping of mantle transition zone discontinuities beneath Alaska using scaled 3-D velocity corrections. *Geophysical journal international*, *219*(2), 1432-1446.

van Stiphout, T., Kissling, E., Wiemer, S., and Ruppert N. (2009), Magmatic processes in the Alaska subduction zone by combined 3-D b value imaging and targeted seismic tomography, *J. Geophys. Res., 114*, B11302, doi:10.1029/2008JB005958.

Vasylkivska, V. S., & Huerta, N. J. (2017). Spatiotemporal distribution of Oklahoma earthquakes: Exploring relationships using a nearest-neighbor approach. *Journal of Geophysical Research: Solid Earth, 122*, 5395–5416. https://doi.org/10.1002/2016JB013918

Verdecchia, A., Cochran, E. S., & Harrington, R. M. (2021). Fluid-earthquake and earthquake-earthquake interactions in southern Kansas, USA. *Journal of Geophysical Research: Solid Earth, 126*, e2020JB020384. https://doi. org/10.1029/2020JB020384

Walsh, R. R., & Zoback, M. D. (2015). Oklahoma's recent earthquakes and saltwater disposal, *Sci. Adv. 1*, e1500195, doi: 10.1126/sciadv.1500195

Wang, K., Ellsworth, W., & Beroza, G. C. (2020b). Revisiting the Timpson induced earthquake sequence: A system of two parallel faults. Geophysical Research Letters, 47, e2020GL089192. https://doi.org/10.1029/2020GL089192

Wang, R., Gu, Y. J., Schultz, R., & Chen, Y. (2018). Faults and non-double-couple components for induced earthquakes. Geophysical Research Letters, 45(17), 8966-8975.

Wang, R., Gu, Y. J., Schultz, R., Kim, A., and Atkinson G. (2016), Source analysis of a potential hydraulic fracturing induced earthquake near Fox Creek, Alberta, *Geophys. Res. Lett., 43*, 564-573, doi:10.1002/2015GL066917

Wang, R., Schmandt, B., Zhang, M., Glasgow, M., Kiser, E., Rysanek, S., & Stairs, R. (2020a). Injection-induced earthquakes on complex fault zones of the Raton Basin illuminated by machine-learning phase picker and dense nodal array. Geophysical Research Letters, 46, e2020GL088168. https://doi.org/10.1029/2020gl088168

Waszek, L., Tauzin, B., Schmerr, N. C., Ballmer, M. D. & Afonso, J. C. (2021). A poorly mixed mantle transition zone and its thermal state inferred from seismic waves. Nat. Geosci. 14, 949–955.

Wei, S., Fielding, E., Leprince, S., Sladen, A., Avouac, J. P., Helmberger, D., ... & Briggs, R. (2011). Superficial simplicity of the 2010 El Mayor–Cucapah earthquake of Baja California in Mexico. Nature geoscience, 4(9), 615-618.

Weingarten, M., Ge, S., Godt, J. W., Bekins, B. A., & Rubinstein, J. L. (2015). High-rate injection is associated with the increase in U.S. mid-continent seismicity. *Science, 348(6241)*, 1336–1340. https://doi.org/10.1126/science.aab1345

Wessel, P., & Smith, W. H. (1991). Free software helps map and display data. *Eos, Transactions American Geophysical Union, 72(41)*, 441–446. https://doi.org/10.1029/90EO00319

Wiemer, S., (2001). A software package to analyze seismicity: Zmap, *Seism. Res. Lett., 72*, 373–382.

Wiemer, S., & Wyss, M. (2000). Minimum magnitude of completeness in earthquake catalogs: Examples from Alaska, the Western United States, and Japan. *Bulletin of the Seismological Society of America, 90(4)*, 859–869. https://doi.org/10.1785/0119990114

Woessner, J., & Wiemer, S. (2005). Assessing the Quality of Earthquake Catalogues: Estimating the Magnitude of Completeness and Its Uncertainty, *Bull. Seismol. Soc. Am.*, *95*(2), 684–698, doi:10.1785/0120040007.

Woodward, L. A. (1997). Role of regional tectonic analysis in exploration for fracture reservoirs in Cretaceous source rocks of the Raton Basin, New Mexico. *Mountain Geologist, 34*, 73–80.

Woollam, J., Münchmeyer, J., Tilmann, F., Rietbrock, A., Lange, D., Bornstein, T., ... & Soto, H. (2022). SeisBench—A toolbox for machine learning in seismology. Seismological Society of America, 93(3), 1695-1709.

Wu, Y., Bao, X., Zhang, B., Xu, Y., & Yang, W. (2022). Seismic evidence for stepwise lithospheric delamination beneath the Tibetan Plateau. Geophysical Research Letters, 49, e2022GL098528. https://doi.org/10.1029/2022GL098528

Yabe, S., & Ide, S. (2018). Why do aftershocks occur within the rupture area of a large earthquake? Geophysical Research Letters, 45, 4780–4787. https://doi.org/10.1029/ 2018GL077843

Yamanaka Y, & Kikuchi M. (2004). Asperity map along the subduction zone in northeastern Japan inferred from regional seismic data. J. Geophys. Res. 109, B07307, doi:10.1029/2003JB002683

Yan, J., Ballmer, M. D. & Tackley, P. J. (2020). The evolution and distribution of recycled oceanic crust in the Earth's mantle: insight from geodynamic models. Earth Planet. Sci. Lett. 537, 116171.

Yang, J., Zhu, H., Lay, T., Niu, Y., Ye, L., Lu, Z., et al. (2021). Multifault opposing-dip strike-slip and normal- fault rupture during the 2020 Mw 6.5 Stanley, Idaho earthquake. Geophysical Research Letters, 48, e2021GL092510. https://doi.org/10.1029/2021GL092510

Ye, L. H. Kanamori, J. P. Avouac, L. Li, K. F. Cheung, T. Lay, (2016). The 16 April 2016, MW 7.8 (MS 7.5) Ecuador earthquake: A quasi-repeat of the 1942 MS 7.5 earthquake and partial re-rupture of the 1906 MS 8.6 Colombia–Ecuador earthquake. Earth Planet. Sci. Lett. 454, 248–258.

Ye, L., Kanamori, H., & Lay, T. (2018). Global variations of large megathrust earthquake rupture characteristics. Science advances, 4(3), eaao4915.

York, D., Evensen, N. M., Martınez, M. L., & De Basabe Delgado, J. (2004). Unified equations for the slope, intercept, and standard errors of the best straight line. American journal of physics, 72(3), 367-375.

Yu, C., Day, E. A., de Hoop, M. V., Campillo, M., Goes, S., Blythe, R. A., & van der Hilst, R. D. (2018). Compositional heterogeneity near the base of the mantle transition zone beneath Hawaii. Nature communications, 9(1), 1-9.

Yue, H., Lay, T., & Koper, K. D. (2012). En échelon and orthogonal fault ruptures of the 11 April 2012 great intraplate earthquakes. Nature, 490(7419), 245-249.

Zaliapin, I., & Ben-Zion, Y. (2013). Earthquake clusters in southern California I: Identification and stability. *Journal of Geophysical Research: Solid Earth*, *118*, 2847-2846, doi:10.1002/jgrb.50179

Zaliapin, I., & Ben-Zion, Y. (2015). Artefacts of earthquake location errors and short-term incompleteness on seismicity clusters in southern California. *Geophys. J. Int.*, *202*, 1949–1968, doi: 10.1093/gji/ggv259

Zaliapin, I., & Ben-Zion, Y. (2016a). A global classification and characterization of earthquake clusters. *Geophysical Journal International*, *207*, 608-634. doi: 10.1093/gji/ggw300

Zaliapin, I., & Ben-Zion, Y. (2016b). Discriminating characteristics of tectonic and human-induced seismicity. *Bull. Seismol. Soc. Am. 106(3)*, 846–859, doi: 10.1785/0120150211

Zaliapin, I., Gabrielov, A., Keilis-Borok, V., & Wong H. (2008). Clustering analysis of seismicity and aftershock identification. *Phys. Rev. Lett. 101(1)*, 018501, doi: 10.1103/ PhysRevLett.101.018501

Zhai, G., Shirzaei, M., Manga, M., & Chen, X. (2019). Pore-pressure diffusion, enhanced by poroelastic stresses, controls induced seismicity in Oklahoma. *Proceedings of the National Academy of Sciences of the United States of America*, *116*(33), 16228–16233. https://doi.org/10.1073/pnas.1819225116

Zhang, H., (2022). Observational constraints on the 520 km mantle discontinuity, mantle transition zone anisotropy, and local seismicity at Mount St. Helens. Ph.D. Dissertation. University of New Mexico.

Zhang, H., Schmandt, B., & Zhang, J. S. (2021). Localized anisotropy in the mantle transition zone due to flow through slab gaps. Geophysical Research Letters, 48(10), e2021GL092712.

Zhang, J. S., and J. D. Bass (2016). Sound velocities of olivine at high pressures and temperatures and the composition of Earth's upper mantle, Geophys. Res. Lett., 43, 9611–9618, doi:10.1002/ 2016GL069949.

Zhang, M., Ellsworth, W. L., & Beroza, G. C. (2019). Rapid Earthquake Association and Location. Seismological Research Letters, 90(6), 2276–2284. https://doi.org/10.1785/0220190052

Zhang, M., Liu, M., Feng, T., Wang, R., & Zhu, W. (2022). LOC-FLOW: An End-to-End Machine Learning-Based High-Precision Earthquake Location Workflow. Seismological Research Letters.

Zhang, X., Feng, W., Du, H., Li, L., Wang, S., Yi, L., & Wang, Y. (2020). The 2018 MW 7.5 Papua New Guinea earth- quake: A dissipative and cascading rupture process. Geophysical Research Letters, 47, e2020GL089271. https://doi. org/10.1029/2020GL089271

Zhou, W.Y., Hao, M., Zhang, J.S., Chen, B., Wang, R., & Schmandt, B., (2022). Constraining composition and temperature variations in the mantle transition zone. Nat. Commun. 13 (1), 1094.

Zhou, Y., Yue, H., Fang, L., Zhou, S., Zhao, L., & Ghosh, A. (2022). An earthquake detection and location architecture for continuous seismograms: Phase picking, association, location, and matched filter (PALM). Seismological Society of America, 93(1), 413-425.

Zhu, W., & Beroza, G. C. (2019). PhaseNet: a deep-neural-network-based seismic arrival-time picking method. *Geophysical Journal International, 216(1)*, 261-273.